A MEASUREMENT OF NUCLEON QUARK SPIN DISTRIBUTIONS AT HERMES

BY

BALIJEET SINGH BAINS

B.S., Louisiana State University and Agricultural and Mechanical College, 1993
M.S., University of Illinois at Urbana-Champaign, 1995

THESIS

Submitted in partial fulfillment of the requirements
for the degree of Doctor of Philosophy in Physics
in the Graduate College of the
University of Illinois at Urbana-Champaign, 2000

Urbana, Illinois

A MEASUREMENT OF NUCLEON QUARK SPIN DISTRIBUTIONS AT HERMES

BY

BALIJEET SINGH BAINS

B.S., Louisiana State University and Agricultural and Mechanical College, 1993
M.S., University of Illinois at Urbana-Champaign, 1995

THESIS

Submitted in partial fulfillment of the requirements
for the degree of Doctor of Philosophy in Physics
in the Graduate College of the
University of Illinois at Urbana-Champaign, 2000

Urbana, Illinois

A MEASUREMENT OF NUCLEON QUARK SPIN DISTRIBUTIONS AT HERMES

Balijeet Singh Bains, Ph.D.
Department of Physics
University of Illinois at Urbana-Champaign, 2000
Dr. Alan M. Nathan, Advisor

The HERMES experiment, commissioned in 1995 for the purpose of investigating the spin structure of the nucleon via deep inelastic scattering of the longitudinally polarized positron storage beam at HERA off polarized gas targets, collected data taken on ^{3}He in 1995 and on ^{1}H in 1996 and 1997.

Inclusive positron asymmetries and the semi-inclusive hadron and pion asymmetries have been extracted from the three years of data. The data cover a kinematic range of $0.023 < x < 0.6$ and $1 < Q^2 < 15$ GeV^2. Polarized quark distributions are further distilled from these asymmetries. In particular, the $\pi^+ - \pi^-$, or charged pion difference asymmetries are used to extract the polarized valence quark distributions u_v and d_v. In an alternate technique, the inclusive positron and semi-inclusive charged hadron asymmetries are used to determine the u, d, and $\bar{q}$ polarized distributions.

In the first part of this thesis an introduction to the theoretical and experimental considerations for this analysis is presented, followed by a description of the measurement of the above-mentioned asymmetries. Finally, the analysis concerning the conversion of these measured asymmetries into quark polarizations is detailed. From the quark polarizations, polarized parton distributions are extracted, and first and second moments calculated.

Acknowledgments

Firstly, I thank my advisor, Alan Nathan, for his support and encouragement of my work throughout my stay at the Nuclear Physics Laboratory, and for affording me the opportunity to join the HERMES Collaboration. In the same vein, I would like to thank Professors Roy Holt and Naomi Makins of Illinois for their advice and help, which was forthcoming whenever requested of them. I also thank Steve Williamson, for without his efforts, the Illinois contribution to HERMES would not have been possible. Also from NPL, I would like to thank Penny Sigler and Gaylon Reeves, without whom nothing would be done as efficiently.

The HERMES Collaboration being large, there are many people without whom the work presented in this thesis could not have been done. I can only name a few here, but thank the entire collaboration for all of their efforts. Andreas Most deserves my thanks for being my first contact at HERMES and for introducing me to my hardware responsibilities there. In my analysis efforts, I must thank Michael McAndrew and Marc Beckmann for their collaboration in our extraction of the 1997 semi-inclusive asymmetries, as well as Bryan Tipton for his help in effecting a purity analysis of those asymmetries. Our work, of course, would not have been possible without the prior work of the inclusive analysis groups. Brendan Fox deserves a hearty thanks for all of his work in synchronizing and formatting the HERMES data so that it was easily analyzeable by all — it is a thankless task of the utmost importance. Brynnen Owen must be mentioned here as well for his patience and help with many of my computer-related travails. The friendships I made at HERMES I count among my most important accomplishments, and so I would like to mention Greg Rakness, Eric Belz and Johan Blouw for their willingness to go out for a beer, or play football on the weekends while at DESY.

In Illinois, I single out my fellow students who have been a large part of my education. In particular, my office-mates Brynnen Owen, Robert Cadman, and Elaine Schulte must be thanked for putting up with me. Outside of NPL, my friend Dohn Arms must be mentioned, for without his help, my graduate career might have been prematurely arrested. Adam and Debra Abeyta, Craig Milling, and Raj Shah are good friends who helped make my experience in Illinois all the more enjoyable.

Finally, I would like to thank my parents Malkiat Singh and Parkash Kaur Bains and my sister Naseem, for their support and encouragement throughout the last seven years. My brother Alijeet must be specially thanked as he has also been my roommate for the last 5 years.

This work was supported by the U.S. National Science Foundation under Grants NSF PHY 93-10871 and NSF PHY 94-20787.

Contents

1

Introduction

The structure of the nucleon has historically been a subject of much study. The nucleon is known to be comprised of constituent spin-$\frac{1}{2}$ particles called quarks and spin-1 gluons, but the details of their assemblage are not fully understood.

1.1 Motivation

After the first Deep Inelastic Scattering (DIS) experiments demonstrated the existence of subnucleonic structure, a model was formulated which pictured the nucleon as an association of three non-interacting spin-$\frac{1}{2}$ pointlike valence quarks of equal mass. This model, now thought of as naïve, provides a useful starting point for the discussion of quark momentum distribution and spin structure of the nucleon. In this model, each quark carries 1/3 of the nucleon's momentum. If x denotes the fraction of the nucleon's momentum carried by the quark, then the x-dependence of the quark flavor momentum distributions in the proton(uud) would be

$$u(x) \;=\; 2d(x) \;=\; 2\delta(x-\frac{1}{3}); \tag{1.1}$$

all of the momentum of the nucleon is carried by the valence quarks. Experiment tells us that this is not the whole story. In fact, measurements have shown that quarks only account for a fraction of the nucleon's momentum. We know that the valence quarks are not free — they are bound to one another by gluons; moreover, at low x, gluons can produce quark-antiquark pairs (sea quarks). The naïve picture tells us, as stated above, that the quark momentum distributions $q(x) \sim \delta(x-\frac{1}{3})$. Picturing the quarks as bound by gluons smears these delta functions, as interaction among the quarks can lead to momentum redistribution. Also, allowing for fluctuation of the gluons into quark-antiquark pairs at low-x leads to additional weighting of the distributions at low x. So the u and d quark momentum distributions are not delta functions, but are instead only peaked around $x = \frac{1}{3}$, as shown in Figure 1.1. Furthermore, experiment has shown that quarks only acount for a fraction of the nucleon's momentum. The rest presumably comes from gluons [1].

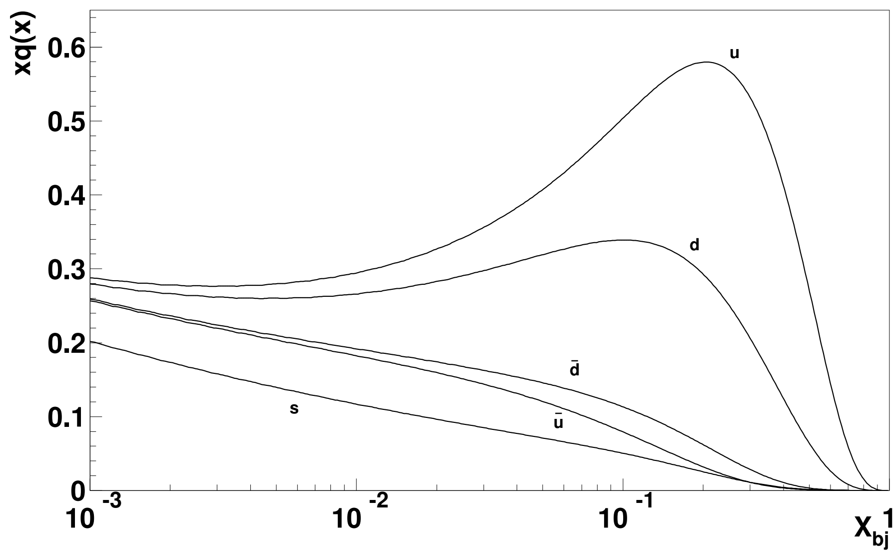

Figure 1.1: x-weighted parametrizations of unpolarized quark distributions from Ref. [2]

In a similar way, a naïve prediction can be made for the spin valence distributions. Assuming the valence quarks to have no relative orbital angular momentum, simple symmetry conditions allows the spin-flavor wavefunction for a spin-up proton to be written as

$$\begin{aligned} |p^{\uparrow}\rangle &= \sqrt{\tfrac{1}{2}}\sqrt{\tfrac{1}{2}}(udu - duu)\sqrt{\tfrac{1}{2}}(\uparrow\downarrow\uparrow - \downarrow\uparrow\uparrow) \\ &+ \sqrt{\tfrac{1}{2}}\sqrt{\tfrac{1}{6}}(udu + duu - 2uud)\sqrt{\tfrac{1}{6}}(\uparrow\downarrow\uparrow + \downarrow\uparrow\uparrow - 2\uparrow\uparrow\downarrow), \end{aligned} \tag{1.2}$$

or

$$|p^{\uparrow}\rangle = \sqrt{\frac{1}{18}}(u^{\uparrow}u^{\downarrow}d^{\uparrow} + u^{\downarrow}u^{\uparrow}d^{\uparrow} - 2u^{\uparrow}u^{\uparrow}d^{\downarrow} + \text{permutations}). \tag{1.3}$$

From this, the spin-weighted numbers of quark flavors, or the average number of each quark flavor found with a particular polarization in the proton can be immediately written down:

$$u^{\uparrow} = \tfrac{5}{3} \quad u^{\downarrow} = \tfrac{1}{3} \quad d^{\uparrow} = \tfrac{1}{3} \quad d^{\downarrow} = \tfrac{2}{3}. \tag{1.4}$$

Therefore,

$$
\begin{aligned}
u \equiv u^{\uparrow} + u^{\downarrow} = 2 \qquad & d \equiv d^{\uparrow} + d^{\downarrow} = 1 \\
\Delta u \equiv u^{\uparrow} - u^{\downarrow} = \tfrac{4}{3} \qquad & \Delta d \equiv d^{\uparrow} - d^{\downarrow} = -\tfrac{1}{3}.
\end{aligned}
\tag{1.5}
$$

In this model, the spin of the proton is carried entirely by its valence quarks ($\Delta u + \Delta d = 1$).

While allowances for contributions to the spin of the nucleon from sea quarks were made, it was still thought that the contributions to the spin of the nucleon from the different quark flavors Δq accounted for its entirety. Polarized DIS experiments at SLAC (E142, E143, E154 and E155) as well as at CERN (The European Muon Collaboration (EMC) and the Spin Muon Collaboration (SMC)), however, performed higher energy experiments that covered a new kinematic regime. The EMC results were the first to contradict this prediction, showing that the spin of the nucleon could not be entirely due to the spin of the underlying quarks. In fact, their results indicated that quarks account for only 40% of the spin of the nucleon [3] and furthermore, that the strange quarks in the sea are significantly negatively polarized. The other experiments confirmed this and helped refine knowledge of the quark contribution to the spin of the nucleon. This underscored the failings of the naïve view of the nucleon; nucleon spin became a many-body problem, with contributions from all of its constituents — contributions from valence and sea spin-$\frac{1}{2}$ quarks (Δq), the spin-1 gluons (ΔG) by which they interact, and possible contributions from quark orbital angular momentum (L_z) all combine to account for the nucleon spin:

$$
\frac{1}{2} \;=\; \frac{1}{2}\sum_q \Delta q + \Delta G + L_z. \tag{1.6}
$$

Solving the spin puzzle, then, became a matter of disentangling the contributions to the nucleon spin from its sources. How much spin is contributed by the valence and sea quarks? How much by gluons or orbital angular momentum?

1.2 Measurements and Predictions

The polarized inclusive DIS measurements made at SLAC and CERN have been in good agreement with the Bjorken Sum Rule [4],

$$\Gamma_1^p - \Gamma_1^n \;=\; \int_0^1 (g_1^p - g_1^n)dx \;=\; \frac{1}{6}[(\Delta u + \Delta\bar{u}) - (\Delta d + \Delta\bar{d})] \;=\; \frac{1}{6}\left|\frac{g_A}{g_V}\right|, \tag{1.7}$$

where $g_{A,V}$ are the weak vector and axial coupling constants. An analysis of world polarized data was performed by SMC in 1998 [5], summarizing the measured structure functions of the above experiments in the following fits:

$$\begin{aligned} \Gamma_1^p(Q^2 = 5\mathrm{GeV}^2) &= \;\;\; 0.121 \pm 0.003(\mathrm{stat}) \pm 0.005(\mathrm{sys}) \pm 0.017(\mathrm{theory}) \\ \Gamma_1^n(Q^2 = 5\mathrm{GeV}^2) &= -0.075 \pm 0.007(\mathrm{stat}) \pm 0.005(\mathrm{sys}) \pm 0.019(\mathrm{theory}) \end{aligned} \tag{1.8}$$

$$(\Gamma_1^p - \Gamma_1^n)(Q^2 = 5\mathrm{GeV}^2) \;=\; 0.174 \pm 0.005(\mathrm{stat})^{+0.011}_{-0.009}(\mathrm{sys})^{+0.021}_{-0.006}(\mathrm{theory}), \tag{1.9}$$

They compare favorably to the theoretically calculated value $\Gamma_1^p - \Gamma_1^n = 0.181 \pm 0.003$ at the same Q^2.

Additionally, hyperon β-decay rates are also related to the axial vector currents. Neutron decay rates yield $\left|\frac{g_A}{g_V}\right| = F + D = 1.257 \pm 0.0028$ [6]. SU(3) flavor symmetry and Λ,Σ decays further constrain F and D with $\frac{F}{D} = 0.575 \pm 0.016$ [3]. These decay rates, coupled with the Γ_1 measurements of the above mentioned experiments, allow flavor separated spin fractions to be evaluated. In this way, Ellis and Karliner [7] arrive at the following picture of nucleon spin structure —

$$\begin{aligned} \Sigma_q \Delta q &= \;\;\; 0.27 \pm 0.04 \\ \Delta u + \Delta\bar{u} &= \;\;\; 0.82 \pm 0.03 \\ \Delta d + \Delta\bar{d} &= -0.44 \pm 0.03 \\ \Delta s + \Delta\bar{s} &= -0.11 \pm 0.03 \end{aligned} \tag{1.10}$$

— reinforcing that only a small fraction of the nucleon spin comes from quarks. Furthermore, they show that the strange sea is significantly negatively polarized.

In addition to making inclusive measurements, SMC was able to directly separate the quark contributions to the spin of the nucleon using semi-inclusive measurements [8]. Imposing the constraint that the sea quark spin contributions are flavor symmetric, they measured at average $Q^2 = 10$ GeV^2 that

$$\begin{aligned} \Delta u - \Delta \bar{u} &= \quad 0.77 \pm 0.10 \pm 0.08 \\ \Delta d - \Delta \bar{d} &= -0.52 \pm 0.14 \pm 0.09 \\ \Delta \bar{q} &= \quad 0.01 \pm 0.04 \pm 0.03. \end{aligned} \tag{1.11}$$

Of note is that the SMC sea polarization is consistent with zero.

1.3 Polarized Quark Distributions at HERMES

The HERMES experiment has been able to make a direct measurement of flavor separated quark spin distributions in the nucleon, improving on the SMC precision. The HERMES experiment has been taking data since 1995, and this thesis describes such an analysis of semi-inclusive DIS measurements made using data accumulated through 1997. It is hoped that the improved precision of the measurements, as compared to SMC, will shed light on the apparent discrepancy between SMC's measurement of the sea quark polarization as consistent with zero and the SU(3)-driven analysis of inclusive scattering measurements and hyperon β-decay suggesting that the strange sea is significantly negative.

Chapter 2 will review the framework of polarized deep-inelastic scattering, describing how the detection of coincident final state hadrons allows for separation of the quark spin distributions by flavor. Chapter 3 details the HERMES experimental setup. Chapter 4 describes the analysis of the 1995–7 data to extract polarized DIS asymmetries. Chapter 5 explains how the measured inclusive and semi-inclusive asymmetries are used to constrain the flavor separated polarized quark distributions, and the spin fractions of the different flavors is calculated. Finally, a summary is presented in Chapter 6.

References

[1] F. Halzen and A. Martin, *Quarks & Leptons, An Introductory Course in Modern Particle Physics* (J. Wiley and Sons, New York, 1984).

[2] H. Lai *et al.*, Phys. Rev. D **55**, 1280 (1997).

[3] F. Close and R. Roberts, Phys. Lett. B **316**, 165 (1993).

[4] J.D. Bjorken, Phys. Rev. **148**, 1467 (1966).

[5] Spin Muon Collaboration, Phys. Rev. D **58**, 112002 (1998).

[6] C. Caso *et al.*, The European Physical Journal **C3**, 1 (1998).

[7] J. Ellis and M. Karliner, hep-ph/9601280.

[8] Spin Muon Collaboration, Phys. Lett. B **420**, 180 (1998).

2

Theory

The main technique used to investigate the structure of the nucleon has been lepton-nucleon scattering. This scattering is called Deep Inelastic Scattering (DIS) at energies where the target breaks apart incoherently. At these energies, the resolution of the scattering is such that the structure of the target can be resolved. The HERMES experiment utilizes polarized positrons or electrons ($\vec{l}$) incident on polarized nucleons ($\vec{N}$) to probe nucleon structure:

$$\vec{l} + \vec{N} \rightarrow l' + X. \tag{2.1}$$

In inclusive measurements, only the scattered lepton (l') is detected, and in semi-inclusive measurements, some of the nucleonic fragments (X) are detected as well. See figure 2.1.

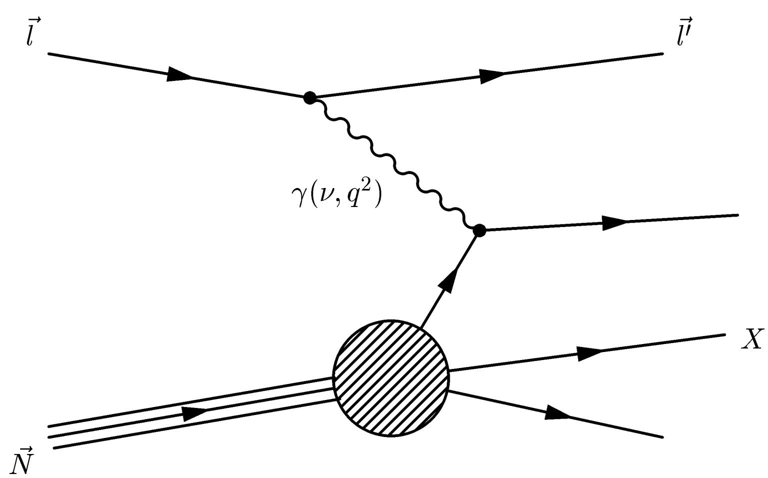

Figure 2.1: Schematic of DIS

2.1 Unpolarized Deep-Inelastic Scattering

Although at HERMES polarized DIS is used, the unpolarized case is useful for introducing the relevant kinematic variables and concepts.

2.1.1 Kinematics

If the four-vectors of the lepton before and after the scattering process are denoted by $\mathbf{l}$ and $\mathbf{l}'$, respectively, the angle of scattering in the laboratory frame denoted by θ, the four-vector of the virtual photon by $\mathbf{q}$, and that of the target nucleon by $\mathbf{N}$, then some useful quantities can be derived.

The negative of the squared four-momentum transfer, or of the virtual photon can be calculated from observables as

$$\begin{aligned} Q^2 &= -\mathbf{q}^2 = -(\mathbf{l}-\mathbf{l}')^2 \\ &\stackrel{\text{lab}}{=} 4EE'\sin^2\theta/2; \end{aligned} \tag{2.2}$$

the energy transfer and relative energy transfer to the nucleon (ν and y, respectively) can be calculated

$$\nu = \frac{\mathbf{N}\cdot\mathbf{q}}{\sqrt{\mathbf{N}^2}} \stackrel{\text{lab}}{=} E - E', \tag{2.3}$$

and

$$y = \frac{\mathbf{N}\cdot\mathbf{q}}{\mathbf{N}\cdot\mathbf{l}} \stackrel{\text{lab}}{=} \nu/E. \tag{2.4}$$

The invariant mass W of the photon-nucleon system, or the nucleon fragments is

$$W^2 = (\mathbf{N}+\mathbf{q})^2 \stackrel{\text{lab}}{=} -Q^2 + M^2 + 2M\nu, \tag{2.5}$$

where $M = \sqrt{N^2}$ is the rest mass of the nucleon. Finally, the Bjorken scaling variable x is defined as

$$x = \frac{-\mathbf{q}^2}{2\mathbf{N}\cdot\mathbf{q}} \stackrel{\text{lab}}{=} \frac{Q^2}{2M\nu} \tag{2.6}$$

and is a measure of the elasticity of the scattering process. $x = 1$ ($W^2 = M^2$) defines elastic scattering while low x identifies a highly inelastic reaction. See table 2.1 for a summary.

Observed Variables		
Variable		Description
$\mathbf{l}(E, \vec{l})$		Beam energy, three-momentum
$\mathbf{l}'(E', \vec{l}')$		Scattered lepton energy, three-momentum
$\mathbf{N}(M, \vec{N} = 0)$		Target nucleon energy, three-momentum

Derived Variables		
Variable	Definition	Description
θ	$\angle(\vec{l}, \vec{l}')$	Lepton scattering angle
$\mathbf{q}$	$\mathbf{l} - \mathbf{l}'$	Virtual photon four-momentum
Q^2	$-\mathbf{q}^2 \overset{\text{lab}}{=} 4EE' \sin^2 \frac{\theta}{2}$	Negative square of virtual photon four-mom.
ν	$(E - E')_{\text{lab}}$	Energy transfer, lab frame
y	ν / E	Relative Energy transfer, lab frame
x	$Q^2 / 2M\nu$	Bjorken scaling variable
s	$M^2 + 2EM + m_e^2$	Lepton-nucleon system invariant mass
W^2	$-Q^2 + M^2 + 2M\nu$	Virtual photon-nucleon invariant mass

Table 2.1: Inclusive Kinematic Variables

2.1.2 Cross-section, Structure Functions

The lowest order Quantum Electrodynamics (QED) DIS cross-section can be written as the contraction of the tensors describing the interactions of the incoming lepton and nucleon with the exchanged photon. This lowest order QED double differential cross-section is written as

$$\frac{d^2\sigma}{dQ^2 d\nu} = \frac{4\pi\alpha^2}{Q^4 E^2} L_{\mu\nu} W^{\mu\nu}, \tag{2.7}$$

where $L_{\mu\nu}$ is the Leptonic Tensor and $W_{\mu\nu}$ the Hadronic Tensor, while $\alpha \approx \frac{1}{137}$ is the electromagnetic coupling constant. $L_{\mu\nu}$ describes the coupling of the incoming point-like lepton with the exchanged virtual photon, is well-known from QED, and can be written down using the Feynman Rules. At DIS energies, the photon is able to resolve the target structure and so the target nucleon cannot be approximated as pointlike. For this reason, $W_{\mu\nu}$ cannot be explicitly written down from first principles. $W_{\mu\nu}$ can be written in general form, however, and after the use of symmetry arguments and conservation laws, a useful form of $W_{\mu\nu}$ is arrived at in terms of dimensionless structure functions. As $W_{\mu\nu}$ can be written in terms of these structure functions, so can the DIS cross-section, after contraction of $L_{\mu\nu}W^{\mu\nu}$ [1].

$$\frac{d^2\sigma}{dxdQ^2} = \frac{4\pi\alpha^2}{xQ^4}(xy^2\mathbf{F_1}(x,Q^2) + (1-y-\frac{xyM}{s})\mathbf{F_2}(x,Q^2)), \tag{2.8}$$

where $\mathbf{F_{1,2}}(x,Q^2)$ are the dimensionless structure functions of the nucleon mentioned above.

2.1.3 Quark Parton Model

At large Q^2 and ν, the above structure functions $\mathbf{F_{1,2}}(x,Q^2)$ are found approximately to be functions only of x, the dimensionless Bjorken scaling variable. The Q^2-dependence of $\mathbf{F_2}$ for fixed values of x is shown in Figure 2.2. This lack of dependence on any variable with a length scale was the first evidence of pointlike nucleon constituents [3], which holds quite well except for the lowest values of x. Further experimental evidence that the Callan-Gross relation

$$\mathbf{F_2}(x) = 2x\mathbf{F_1}(x) \tag{2.9}$$

was satisfied implied that those pointlike nucleon constituents were largely, if not all, spin-1/2 [4].

In the Quark Parton Model (QPM) (also at this Bjorken limit), the Bjorken scaling variable x can be associated with the fraction of the nucleon's momentum carried by the struck parton, or quark. The scattering process of the lepton off of the spatially extended nucleon can be expressed as the incoherent sum of elastic scattering off point-like partons. This allows for a simple interpretation of the structure function $\mathbf{F_2}$ as the charge-weighted sum of the parton momentum distributions

$$\mathbf{F_2}(x) = x\sum_q e_q^2 q(x) \tag{2.10}$$

where the sum is over the quark flavors q, e_q denotes the charge of quark flavor q, and $q(x)$ are the parton distribution functions (PDFs) [5]. PDFs give the number density of a quark of flavor q and with nucleon momentum fraction x.

This QPM picture of the nucleon as a collection of bound non-interacting spin-1/2

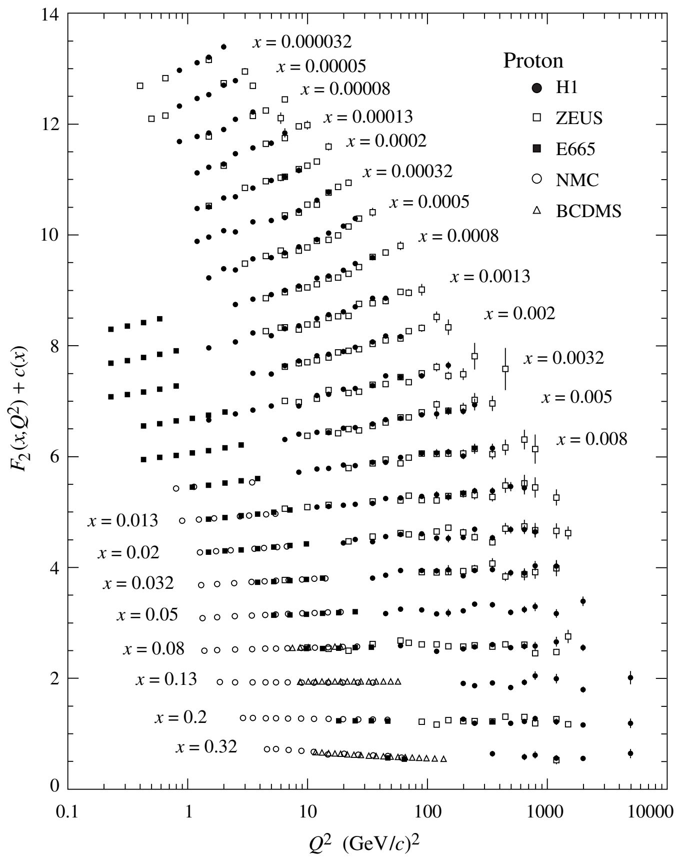

Figure 2.2: Proton Structure Function, F_2^p measured in electromagnetic scattering of electrons (H1,ZEUS) and muons (BCDMS, E665, NMC), in the kinematic domain of the HERA data. Only statistical errors are shown. The data are plotted as a function of Q^2 at fixed x. For the purposes of plotting, a constant $c(x) = 0.6(i_x - 0.4)$ is added to F_2^p, where i_x is the number of the x bin ranging from $i_x = 1(x = 0.32)$ to $i_x = 21(x = 0.000032)$. From [2].

---

quarks is not of course, strictly correct. The Callan-Gross relation (Eq. 2.9) does not hold; there are measurable deviations from it, parametrized by the function

$$R(x, Q^2) \;=\; (1+\gamma^2)\frac{\mathbf{F_2}(x, Q^2)}{2x\mathbf{F_1}(x, Q^2)} - 1 \tag{2.11}$$

where γ^2 is a kinematical factor defined

$$\gamma^2 \;=\; \frac{Q^2}{\nu^2} \;=\; \frac{4M^2x^2}{Q^2}. \tag{2.12}$$

In the Bjorken limit of course, γ^2 vanishes. R is interpreted as the ratio of the cross-sections of the absorption by the nucleon of longitudinally polarized virtual photons to transversely polarized virtual photons:

$$\begin{aligned} R(x,Q^2) &= \sigma_L/\sigma_T; \\ \sigma &= \Gamma_T(\sigma_T+\varepsilon\sigma_L), \end{aligned} \tag{2.13}$$

where σ is the total cross-section, Γ_T is the total flux of transversely polarized virtual photons, and ε is the ratio of the probability of the lepton emitting a longitudinally polarized photon to that of it emitting a transversely polarized one.

$$\varepsilon = \frac{\Gamma_L}{\Gamma_T} = \frac{1-y}{1-y+\frac{1}{2}y^2}. \tag{2.14}$$

If the Callan-Gross relation were strictly true, σ_L would be zero, meaning that the nucleon could not contain partons with transversely oriented spin. $R(x,Q^2)$ corrects for deviations from this approximation.

In addition to the breaking of the Callan-Gross relation, the quark and gluon interactions neglected in the QPM cause explicit Q^2 dependencies in the structure functions. The underlying effects for this scaling violation can be calculated [6] and structure functions measured at one Q^2 can be evolved to another.

2.2 Polarized DIS — Inclusive

The unpolarized cross-section (2.8) is arrived at by averaging over all of the incoming lepton's spin states. This necessarily forces all spin-asymmetric contributions to $L_{\mu\nu}W^{\mu\nu}$ to cancel. If, however, the difference of both spin states is calculated, the symmetric parts cancel and the asymmetric terms are evident.

2.2.1 Polarized Structure Functions

In the cases where the spins of the incoming lepton and the target nucleon are parallel ($\uparrow\Uparrow$) and anti-parallel ($\uparrow\Downarrow$), the difference of the cross-sections of the two relative spin states is given by

$$\frac{d^2\sigma^{\uparrow\Downarrow} - d^2\sigma^{\uparrow\Uparrow}}{dxdy} = \frac{e^4}{4\pi^2 Q^2}\left[\left(1 - \frac{y}{2} - \frac{y^2}{4}\gamma^2\right)\mathbf{g_1}(x,Q^2) - \frac{y}{2}\gamma^2\mathbf{g_2}(x,Q^2)\right], \tag{2.15}$$

where $\mathbf{g}_{\mathbf{1},\mathbf{2}}(x,Q^2)$ are, analogously to $\mathbf{F}_{\mathbf{1},\mathbf{2}}(x,Q^2)$, the dimensionless polarized structure functions of the nucleon.

Just as the unpolarized structure functions can be cast in the QPM, so can the polarized ones. The PDFs introduced in Eq. 2.10 are rewritten and the polarized PDFs are introduced as

$$\begin{aligned} q(x) &= q^{\uparrow}(x) + q^{\downarrow}(x), \text{ and} \\ \Delta q(x) &= q^{\uparrow}(x) - q^{\downarrow}(x), \end{aligned} \tag{2.16}$$

where $q^{+(-)}(x)$ give the quark density of flavor q at momentum fraction x with helicity parallel (anti-parallel) to the nucleon spin. The polarized structure functions $\mathbf{g}_{\mathbf{1},\mathbf{2}}$ scale as the unpolarized ones do in the Bjorken limit, and extending the analogy with Eq. 2.10 they can be written

$$\begin{aligned} \mathbf{g_1}(x) &= \frac{1}{2}\sum_q e_q^2 \Delta q(x), \\ \mathbf{g_2}(x) &= 0. \end{aligned} \tag{2.17}$$

The scaling approximations that the QPM relies on reduces the number of relevant polarized structure functions to one, just as it does for unpolarized structure functions.

2.2.2 Inclusive Asymmetries

The spin structure functions can be experimentally determined by measuring the cross-sections when the lepton and nucleon spins are in two different longitudinal configurations (relatively, at 0° and 180°) and two different transverse (90°, 270°) configurations. Then the asymmetries $A_{\|}$ and $A_{\perp}$ can be defined as

$$A_{\|} = \frac{\sigma(180^\circ) - \sigma(0^\circ)}{\sigma(180^\circ) + \sigma(0^\circ)}$$

$$A_\perp = \frac{\sigma(270^\circ) - \sigma(90^\circ)}{\sigma(270^\circ) + \sigma(90^\circ)}. \tag{2.18}$$

The virtual photon is not emitted collinearly with the incoming lepton, but the above measured asymmetries of Eq. 2.18 can be translated into the asymmetries of the exchanged virtual photon $A_{1,2}$ [7]:

$$\begin{aligned} A_{||} &= D(A_1 + \eta A_2) \\ A_\perp &= d(A_2 - \xi A_1). \end{aligned} \tag{2.19}$$

The kinematic factors D, d and η, ξ are defined as

$$D = \frac{y(2-y)}{y^2 + 2(1-y)(1+R(x,Q^2))}, \tag{2.20}$$

$$d = D\sqrt{\frac{2\varepsilon}{1+\varepsilon}}, \tag{2.21}$$

$$\eta = \frac{2\gamma(1-y)}{2-y}, \tag{2.22}$$

$$\xi = \eta\frac{1+\varepsilon}{2\varepsilon}, \tag{2.23}$$

with ε defined as in 2.14. D and d are the depolarization factors of the virtual photon. The virtual photon asymmetries $A_{1,2}$ are directly related to the photon absorption cross-section of the nucleon. If $\sigma_{1/2}$ and $\sigma_{3/2}$ are the virtual photon absorption cross-sections when the projection of the total angular momentum of the photon-nucleon system into the virtual photon's momentum direction is 1/2 and 3/2, respectively, then $A_{1,2}$ can be written as

$$\begin{aligned} A_1 &= \frac{\sigma_{1/2} - \sigma_{3/2}}{\sigma_{1/2} + \sigma_{3/2}} = \frac{\mathbf{g_1} - \gamma^2 \mathbf{g_2}}{\mathbf{F_1}} \\ A_2 &= \frac{\sigma_{TL}}{\sigma_T} = \frac{\gamma(\mathbf{g_1} + \mathbf{g_2})}{\mathbf{F_1}}. \end{aligned} \tag{2.24}$$

$\sigma_T = \frac{1}{2}(\sigma_{1/2} + \sigma_{3/2})$ is the total transverse photon absorption cross-section and σ_{TL} is a term that arises from the interference between transverse and longitudinal amplitudes.

The asymmetry A_2 is limited by the positivity limit $|A_2| < R(x, Q^2)$ and has been measured to be far smaller [8]. This, plus the fact that its contribution to $A_{||}$ is suppressed by the small factor η, allows for the approximation

$$A_{\|} \approx DA_1. \tag{2.25}$$

Solving Eq. 2.24 under the $A_2 = 0$ assumption gives

$$\begin{aligned} \frac{\mathbf{g_1}}{\mathbf{F_1}} &\approx \frac{A_1}{1+\gamma^2} \\ \mathbf{g_1}(x,Q^2) &\approx \frac{A_{\|}(x,Q^2)}{D} \frac{\mathbf{F_2}(x,Q^2)}{2x[1+R(x,Q^2)]} \end{aligned} \tag{2.26}$$

Making the single measurement of the longitudinal spin asymmetry $A_{\|}$, coupled with existing unpolarized determinations of $\mathbf{F_2}$ and $R(x,Q^2)$ is sufficient for measurement of the polarized structure function $\mathbf{g_1}$.

2.3 Polarized DIS — Semi-Inclusive

The case of semi-inclusive DIS reactions, namely,

$$\vec{l} + \vec{N} \rightarrow l' + h + X, \tag{2.27}$$

where particles other than the scattered lepton (l') are detected in the final state, can also be used to probe nucleon structure. A model for the fragmentation process — the process by which the detected final state hadrons (h) are created in the DIS reaction — is added to the Quark-Parton Model. Measured hadron asymmetries can then be cast in a formalism that facilitates the extraction of parton distribution functions.

Important semi-inclusive kinematic variables are found in table 2.2.

2.3.1 Fragmentation

The cross-section for the semi-inclusive reaction where hadron h is detected in the final state is written as

$$\frac{d^3\sigma}{dxdQ^2dz} = \frac{\sum_q e_q^2 q(x) D_q^h(z)}{\sum_q e_q^2 q(x)} \cdot \frac{d^2\sigma}{dxdQ^2}(x,Q^2), \tag{2.28}$$

Observed Variables		
Variable		Description
E_h		Energy of detected hadron
$\vec{p_h}$		Hadron momentum 3-vector
Derived Variables		
Variable	Definition	Description
z	E_h/ν	Fraction of energy transfer carried by hadron
$p_{\|\|}$	$(\vec{p_h}\cdot\vec{q})/\sqrt{q^2}$	Component of $\vec{p}$ in direction of virtual photon
x_F	$(2\|p_{\|\|}^2\|/\sqrt{W^2})_{\text{com}}$	Feynman scaling variable

Table 2.2: Semi-inclusive Kinematic Variables

introducing the fragmentation functions $D_q^h(z)$. The fragmentation functions give the number density of hadrons h produced with energy fraction $z \stackrel{\text{lab}}{=} E_h/\nu$ of the transfer energy when a quark of flavor q is struck. The fragmentation functions' lack of dependence on any inclusive kinematic variable (such as x or Q^2) is due to the assumption that the hadronization process can be separated from the scattering process and is known as factorization.

The number of fragmentation functions $D_q^h(z)$ can be reduced by application of isospin and charge symmetry. In the case of charged pions, for example, there are 12 fragmentation functions: 2 hadron types ($h \in \{\pi^+, \pi^-\}$) times 6 quark flavors ($q \in \{u, d, s, \bar{u}, \bar{d}, \bar{s}\}$). Applying isospin and charge symmetry reduces the number of functions required to parametrize the generation of pions to three:

$$
\begin{aligned}
D^+(z) &= D_u^{\pi^+}(z) = D_d^{\pi^-}(z) = D_{\bar{d}}^{\pi^+}(z) = D_{\bar{u}}^{\pi^-}(z), \\
D^-(z) &= D_d^{\pi^+}(z) = D_u^{\pi^-}(z) = D_{\bar{u}}^{\pi^+}(z) = D_{\bar{d}}^{\pi^-}(z), \\
D^s(z) &= D_s^{\pi^+}(z) = D_s^{\pi^-}(z) = D_{\bar{s}}^{\pi^+}(z) = D_{\bar{s}}^{\pi^-}(z).
\end{aligned}
\tag{2.29}
$$

The fragmentation functions $D^+(z)$ and $D^-(z)$ are called favored and unfavored, respectively, and have been measured by HERMES [9]. Since the likelihood of producing a hadron that contains the struck quark is higher than that of a hadron which does not contain the struck quark, $D^+(z) > D^-(z)$ for all z.

2.3.2 Fragmentation Models

The fragmentation process cannot yet be calculated from first principles, so fragmentation models have been created to provide a general framework in which to study hadron production. These physically motivated models have been designed to be used in Monte Carlo programs, their parameters tuned such that generated particle and momentum distributions match observed data.

Independent Fragmentation

One of the earliest fragmentation models, the Independent Fragmentation Model, was developed in the early 1970s by Feynman and Field [10, 11]. Based on the assumption that every parton fragments independently, the model reproduces the momentum and energy fraction distributions observed in quark jets produced in e^+e^- annihilation.

In the model, the struck quark fragments by picking up $q\bar{q}$-pairs from the vacuum. The struck quark pairs with the anti-quark of the pair, leaving the remaining quark to pair with the anti-quark of the next $q\bar{q}$-pair. This continues until an energy threshold is reached, parametrized by a function giving the probability that energy fraction z is left to the remaining cascade after $q\bar{q}$-pair production. The probabilities of producing $u\bar{u}$, $d\bar{d}$, and $s\bar{s}$-pairs are given by γ_u, γ_d, and γ_s, respectively, with $\gamma = \gamma_u = \gamma_d$ and $\gamma_s = 1 - 2\gamma$. The measured K/π ratio determines $\gamma_s = 0.3\gamma$ [12]. The width of the transverse momentum distribution of the $q\bar{q}$-pairs, assumed to be Gaussian, is controlled by a third parameter. The model predicts the ratio of unfavored to favored fragmentation functions to be

$$\frac{D^-(z)}{D^+(z)} = \frac{\gamma(1-z)}{z+\gamma(1-z)}, \tag{2.30}$$

verified by experimental data.

Despite this model's successes in describing some properties of hadronic jets, it remains unsatisfactory. The possibility of baryon emission is neglected, and furthermore, Lorentz transformation into another reference frame causes a violation of momentum conservation. Particle multiplicities are dependent on reference frame as well. Finally, since the cascade of $q\bar{q}$-pairs is abruptly stopped once a remaining energy threshold is reached, color and flavor quantum numbers are not conserved.

The Lund String Model

The Lund String Model [13] is similar to the Independent Fragmentation Model, but does not treat the struck parton independently. Based on the QCD prediction of confinement, in this model, the struck parton is connected to the target remnant via the color field, which is concentrated along a tube called a string. The potential energy of the color field between the quarks grows with the distance between them. When this potential field energy is sufficient to produce a $q\bar{q}$-pair, one is produced and the string is divided into two substrings which fragment in the same way until a colorless hadron on the mass shell is produced.

Tunable parameters in this model are the flavor production ratios (equivalent to the γs in the Independent Fragmentation Model), the ratio between quark and diquark production (controlling the production ratio of mesons to baryons), two parameters controlling string breaking probability, and a last parameter determining the transverse momentum distribution. The Lund model is invariant under Lorentz transformation and conserves all quantum numbers. The parameters of the model were tuned so that at HERMES energies, observed hadron spectra are matched [9].

Cluster Fragmentation

A last model, the cluster fragmentation model [14], is based on using QCD perturbation theory as far as possible, rather than parametrizing the fragmentation process as the Independent and Lund models do. Virtual partons from the photon-parton interaction form colorless clusters of low virtuality. The resulting clusters then produce the observed hadrons by simple phase space decays. The cluster model has the advantage of being theory driven, not requiring ad hoc parametrization assumptions. Tunable parameters are the parton masses, the QCD scale parameter, and the maximum cluster mass. High-energy data has been successfully described by the cluster model, but hadron spectra at HERMES energies have not been described as well as by the Lund model [9].

2.3.3 Hadron Asymmetries

The measured semi-inclusive asymmetry of a hadron h can be defined analogously to the inclusive asymmetry (Eq. 2.18), as

$$A_{\parallel}^{h} = \frac{\sigma_h(180°) - \sigma_h(0°)}{\sigma_h(180°) + \sigma_h(0°)} \tag{2.31}$$

Using the factorization assumption mentioned in section 2.3.1 — that the scattering process and the hadronization process can be separated and described independently — the semi-inclusive analogies to the inclusive structure functions (Eq. 2.10, 2.17) can be made:

$$\begin{aligned} g_1^h(x,z) &= \frac{1}{2}\sum_q e_q^2 D_q^h(z)\Delta q(x) \\ F_1^h(x,z) &= \frac{1}{2}\sum_q e_q^2 D_q^h(z) q(x). \end{aligned} \tag{2.32}$$

Continuing onwards, a relation between the polarized and unpolarized PDFs, the fragmentation functions, and the measured hadron asymmetries $A_{\parallel}$ is arrived at:

$$\frac{\sum_q e_q^2 D_q^h(z)\Delta q(x)}{\sum_{q'} e_{q'}^2 D_{q'}^h(z) q'(x)}[1 + R(x,Q^2)] = \frac{A_{\parallel}^h(x,z)}{D}. \tag{2.33}$$

It is assumed that $A_2^h = 0$, as in the inclusive case.

2.3.4 Purities Defined

If we define, for brevity, the measured longitudinal asymmetries corrected by the depolarization factor as

$$A^h(x,z) = \frac{A_{\parallel}^h(x,z)}{D}, \tag{2.34}$$

with A^{e^+} similarly defined for the inclusive case, we can rewrite Eq. 2.33 and also manipulate it such that

$$A^h(x,z) = (1+R)\frac{\sum_q e_q^2 D_q^h(z)\Delta q(x)}{\sum_{q'} e_{q'}^2 D_{q'}^h(z) q'(x)}$$

$$= \quad (1+R)\sum_q \frac{e_q^2 D_q^h(z) q(x)}{\sum_{q'} e_{q'}^2 D_{q'}^h(z) q'(x)} \frac{\Delta q(x)}{q(x)}. \tag{2.35}$$

Cast in this manner, the asymmetry can be simplified by defining the unpolarized information as the hadron purity

$$P_q^h(x,z) \;=\; \frac{e_q^2 D_q^h(z) q(x)}{\sum_{q'} e_{q'}^2 D_{q'}^h(z) q'(x)}, \tag{2.36}$$

which can be physically interpreted as the probability that quark flavor q was struck in an event when hadron h with energy fraction z is detected. Eq. 2.35 can be rewritten such that the asymmetries are linear in the ratios of the polarized and unpolarized parton density functions, or quark polarizations;

$$A^h(x,z) \;=\; (1+R)\sum_q P_q^h(x,z)\frac{\Delta q(x)}{q(x)}. \tag{2.37}$$

The purities being probabilities, the relation

$$\sum_q \int P_q^h(x,z)dz \;=\; 1 \tag{2.38}$$

holds for every x-bin. A purity for the scattered lepton can be defined as well by setting $D_q^{e^+} \equiv 1$, so that the inclusive asymmetries can be treated in the analysis in the same manner as the semi-inclusive asymmetries.

References

[1] A. Manohar, in *Symmetry and Spin in the Standard Model, Proceedings of the Seventh Lake Louise Winter Institute* (World Scientific, Singapore, 1992), pp. 1–46.

[2] C. Caso *et al.*, The European Physical Journal **C3**, 1 (1998).

[3] J.D. Bjorken, Phys. Rev. **179**, 1547 (1969).

[4] C. Callan, Jr. and D. J. Gross, Phys. Rev. Lett. **22**, 156 (1969).

[5] R. Feynman, *Photon-Hadron Interactions* (Addison-Wesley Publishing, Co., Inc., Redwood City, California, 1989).

[6] G. Altarelli and G. Parisi, Nucl. Phys. B **126**, 298 (1977).

[7] M. Düren, The HERMES Experiment: From the Design to the First Results, 1995, DESY-HERMES-95-02.

[8] E143 Collaboration, Phys. Rev. Lett. **76**, 587 (1996).

[9] P. Geiger, Ph.D. thesis, Ruprecht-Karls-Universität Heidelberg, Germany, 1998.

[10] R. Field and R. Feynman, Phys. Rev. D **15**, 2590 (1977).

[11] R. Field and R. Feynman, Nucl. Phys. B **136**, 1 (1978).

[12] European Muon Collaboration, Phys. Lett. B **145**, 156 (1984).

[13] B. Andersson, G. Gustafson, *et al.*, Phys. Rept. **97**, 31 (1983).

[14] G. Marchesini, B. Webber, *et al.*, Comp. Phys. Comm. **67**, 465 (1992).

3

The Experiment

To fulfill its goal of exploring nucleon spin structure via deep-inelastic lepton scattering with pure internal targets, the HERMES experimental setup must meet several needs.

A lepton beam with high current (I) is desired to maximize the deep-inelastic scattering rate. In polarized physics, a high polarization of the beam (P_B) is also needed to more easily measure spin observables. For these same reasons, high nucleon target densities (n) and target polarization (P_T) are also needed. Additionally, a high dilution factor (f), which is the ratio of polarized nucleons to total nucleons in the target, is desired. These quantities are often combined to calculate the figure of merit (FOM) of an experiment, which is a measure of its statistical precision. For polarized DIS,

$$\mathrm{FOM} \;=\; nIt(P_B P_T f)^2, \tag{3.1}$$

where t is the running time of the experiment. As statistical uncertainties scale as $\frac{1}{\sqrt{\mathrm{FOM}}}$, maximizing the FOM is a goal of experiment design.

For inclusive physics, the determination of scattering kinematics should be done with high precision. Separation of the scattered lepton from background particles is essential. For semi-inclusive physics, the acceptance of the spectrometer should be large enough to accept a variety of multi-particle final states. Separation of detected hadrons through particle identification into different types provides further physics possibilities.

This chapter will detail the specifics of how the HERMES experimental setup achieves its goal of providing the ability to make precise polarized DIS inclusive and semi-inclusive measurements. HERMES makes use of the HERA positron storage ring incident on an internal polarized gas target. A forward acceptance spectrometer extends 8.5 meters behind the target to capture the particles produced in the beam-target interaction. This arrangement is novel in two respects. The use of an internal target provides the advantages of a high atomic purity ($f \sim 1$) and the high beam currents available in a storage ring. Previous experiments were limited by either fixed solid or liquid targets, which give small dilution factors from unpolarized material in or around the target. HERMES also has the advantage of an open geometry spectrometer which allows the detection of multi-particle final states. Previous experiments have lacked either the acceptance or the particle identification available at HERMES.

3.1 The Beam

The HERMES experiment is run in the eastern experimental area of the Hadronen Elektronen Ring Anlage (HERA) facility at the Deutsches Elektronen-Synchrotron (DESY) in Hamburg Germany. A schematic diagram of HERA and HERMES can be seen in Figure 3.1. HERMES shares HERA with three other experiments; ZEUS, HERA-B, and H1 are located at the south, west, and north interaction points of HERA, respectively.

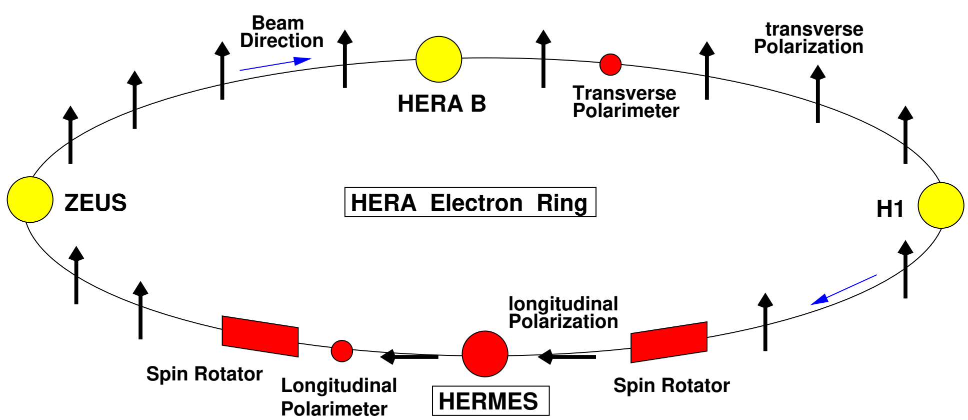

Figure 3.1: Schematic diagram of the HERA collider facility and location of the HERMES experiment. The heavy arrows depict the positron beam polarization, which is rotated from transverse to longitudinal and back by spin rotators before and after the HERMES experimental area. Transverse and longitudinal polarimeters measure the beam polarizations on opposite sides of the ring.

HERMES was designed to detect the scattering products of polarized leptons and polarized nucleons. While HERA is an e-p collider, it is unable to deliver polarized protons, and so

HERMES makes use of only the 27.5 GeV e beam, while the 820 GeV p beam passes through the experimental area without interaction. The e beam is incident on a fixed polarized gas target with the scattering final state particles detected by the HERMES spectrometer.

HERA can inject either positrons or electrons, but due to lifetime problems caused by the attraction of positive ions to the electron beam, HERA injected positrons from 1995–97. For the physics of interest at HERMES there is no difference between e^+-p and e^--p scattering.

The electron beam is naturally highly transversely polarized due to an asymmetry in the emission of synchrotron radiation. This Sokolov-Ternov effect [1] occurs for positrons moving in a plane perpendicular to a uniform magnetic field. A small difference in the rate of synchrotron emission between states with positron spin parallel and anti-parallel to the magnetic field results in the spin-flip to parallel occurring more often than the spin-flip to anti-parallel. The polarization of the beam builds up and asymptotically reaches its maximum:

$$P_B(t) \;=\; P_{\max}(1 - e^{-t/\tau}). \tag{3.2}$$

$P_{\max}$ is the equilibrium polarization, and τ is the polarization rise time constant.

The natural rise of the positron beam polarization is hampered by depolarizing effects, such as the orbital effects of synchrotron emission, as well as magnetic and alignment imperfections. These depolarizing effects have the result of reducing both the maximum polarization and rise time of the electron beam, from 92% and 37 min. [2] to the experimentally determined ~55% and ~22 min.

The physics of interest at HERMES requires the lepton beam to be longitudinally polarized. To achieve this, a pair of spin rotators is placed in the ring before and after the HERMES experimental area, as depicted in Figure 3.1. The two rotators are matched such that the first rotator turns the positron spin into the axis of the beam momentum, while the second turns the spin back to the transverse direction. Each spin rotator is a series of six dipole magnets, alternately vertical and horizontal, extending over 56 m.

From Reference [3], it is known that the effect of the spin rotator magnets on the spin precession is a factor of 63 larger than its effect on the spin orbit. As rotations in space do not commute, a pattern of rotations and orbit bumps can be selected so the beam polarization is rotated as desired while the beam orbit is preserved, apart from a net horizontal bump of 22 cm. This net effect of these rotators is depicted in Figure 3.2. Of note is that HERA is the first high energy positron or electron storage ring to achieve longitudinal polarization [4]. Figure 3.3 shows a measured rise of the HERA positron polarization.

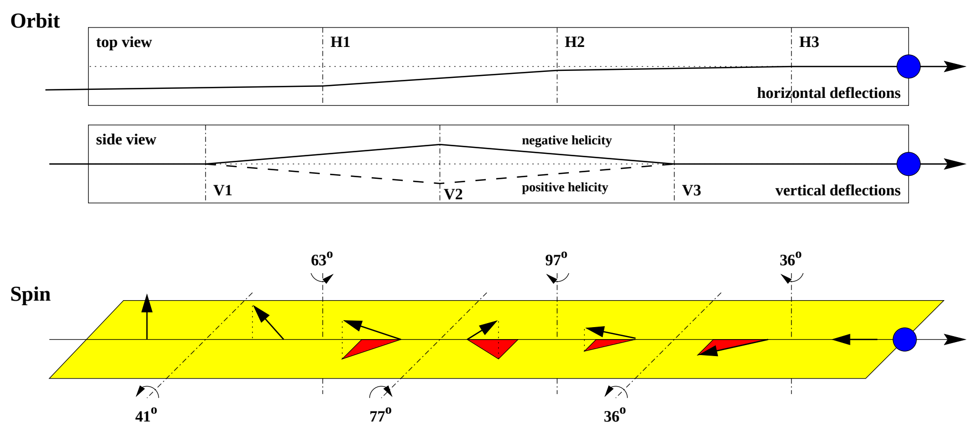

Figure 3.2: Effect of one spin rotator. A series of vertical and horizontal magnetic fields affect the beam orbit (top) and rotate the positron polarization direction (bottom). The sequence is such that the vertical position of the orbit is unchanged but a small horizontal bump results.

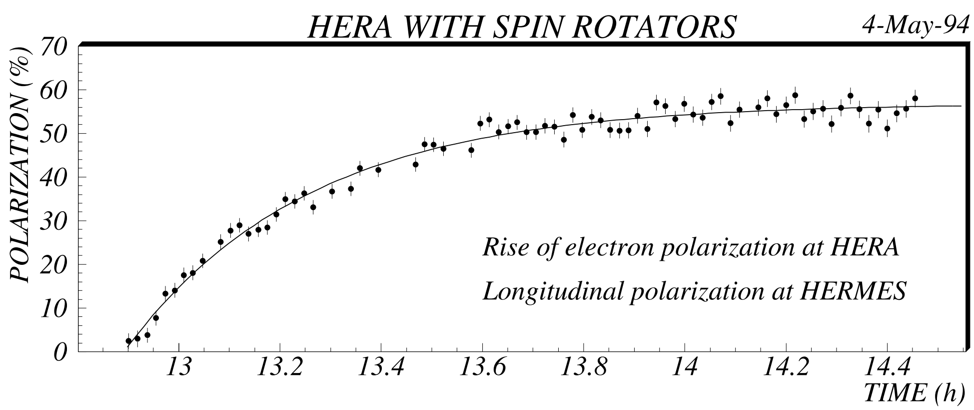

Figure 3.3: The first observation of longitudinal polarization at HERA. A typical HERMES risetime constant of 21 minutes and maximal polarization of 57% are shown in the exponential curve.

Measuring the beam polarization is done by two Compton polarimeters scattering circularly polarized laser light off the beam. The transverse polarimeter, located in the western section of HERA, is designed to use the fact that the Compton cross-section of polarized photons on transversely polarized leptons shows a spin-dependent azimuthal distribution. The laser intensity is chosen so that on the average, only 0.01 photons are backscattered per beam electron bunch. The scattered photons are detected in a position sensitive calorimeter; the top-bottom asymmetry of the position distribution of backscattered photons can be used to derive the beam polarization [2]. Starting in 1997, a second polarimeter in the eastern section of HERA was commissioned to directly measure the longitudinal polarization near the HERMES interaction point. This longitudinal polarimeter uses the fact that the spin-dependent angular distribution of the Compton cross-section on longitudinally polarized leptons can be translated into a spin-dependent energy spectrum. Energy weighted spin asymmetries can be formed and used to measure the beam polarization [5, 6].

3.2 The Targets

HERMES' location in a storage ring precludes the use of a fixed solid or liquid target. While solid or liquid targets have high densities, they also have low dilution factors due to low polarized fraction, and can potentially cause multiple scattering due to massive cell windows or the high target density.

At HERMES an internal gas target is used by inserting a thin windowless cylindrical storage cell into the positron beamline. A diagram of the target region is shown in Figure 3.4. This storage cell is fed by a polarized gas source. A vacuum pumping system removes the gas on either end, preserving the ring vacuum.

The storage cell, which confines the gas atoms near the positron beam, provides for densities two orders of magnitude greater than that of a free gas jet intersecting the beam [7]. The target gas is injected into the cell near the center of the cylinder. This produces a triangular density profile along the beam direction, as shown in Figure 3.5.

The target cell is 550 mm long with a 29×9.8 mm elliptical cross-section. The cell is fabricated from 100 μm thick 99.999% pure aluminum [7] and is cooled to the 15-100K range by cold helium gas flowing through the supports. This further increases the target gas density by slowing thermal diffusion of the gas towards the ends of the storage cell. The cell is within an aluminum vacuum chamber. Scattered particles from the target exit through a 0.33 mm stainless steel exit window. Thin-walled metal meshes called wakefield

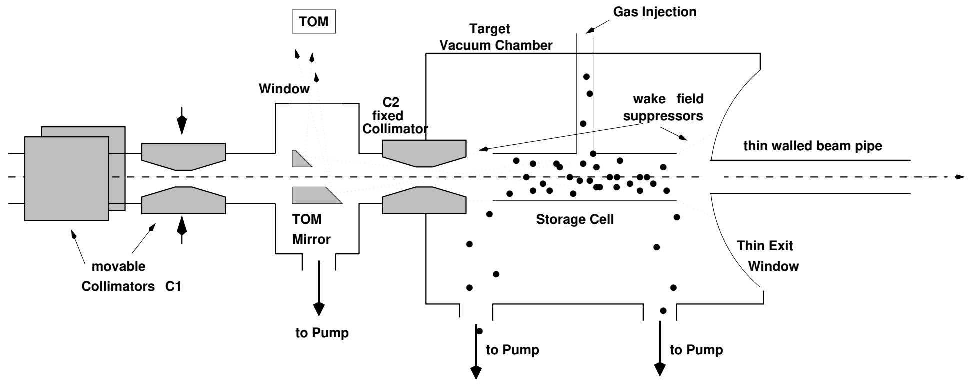

Figure 3.4: Schematic diagram of the HERMES target region.

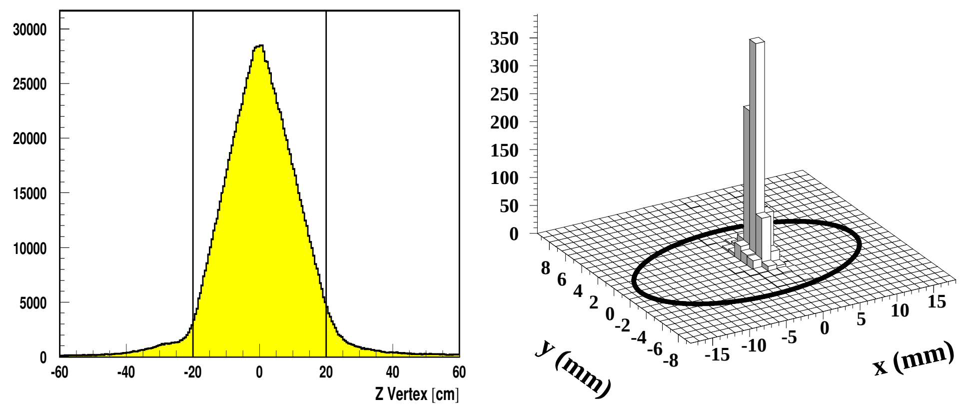

Figure 3.5: Track distribution in the target cell. The left shows the triangular distribution in the cell along the positron beam direction. The right shows the transverse event distribution. The ellipse shows the target storage cell boundary.

---

suppressors connect the target cell to the positron beampipe and ensure the continuity of electromagnetic fields.

As the synchrotron radiation from the positron beam may damage the target cell and may also increase the detector background, a system of collimators is used. Referring to Figure 3.4, Collimators C1 block the synchrotron light from 2m upstream of the target. C1 consists of two pairs of collimators, one horizontally and one vertically movable. A fixed collimator C2 sits next to the cell and shields it from particles scattered from C1.

For polarized physics at HERMES during 1995–97, two different gas sources were used to create and monitor the polarization of nuclei in the target. The ^{3}He target was installed for the 1995 run, and the ^{1}H target replaced it in 1996. Table 3.1 shows a comparison of the main features of the two targets, which are detailed in the following Sections.

	^{3}He	^{1}H
Ave. Polarization	46%	88%
Relative Error	±5%	±4%
Thickness	10^{15} nucleons/cm^2	$7.6 \cdot 10^{13}$ nucleons/cm^2
Atomic Fraction	1.0	0.93 ± 0.04
Source Intensity	$1 \cdot 10^{17}$ atoms/s	$6 \cdot 10^{16}$ atoms/s
Switching Time	10 min	45 s
Cell Temperature	25 K	100 K
Holding Field	3.2 mT	335 mT
Cell Coating	None	Dri-film, Ice

Table 3.1: Main parameters of the ^{3}He and ^{1}H targets.

3.2.1 ^{3}He Target

In 1995 a target using polarized ^{3}He was installed at the HERMES interaction point to study polarized DIS from a neutron target. Polarized ^{3}He can be viewed approximately as a spin-polarized neutron with two spin-paired protons that provide net unpolarized dilution. The ^{3}He target consists of a cubic quartz "pumping" cell illuminated by infrared laser light through which ^{3}He becomes polarized and flows into the storage cell, as depicted in Figure 3.6.

A weak radio frequency discharge excites a small fraction of the atoms to the 2^3S$_1$ metastable state, which is then optically pumped to the higher 2^3P$_0$ state by circularly polarized laser light. The excited states decay back to the metastable level by isotropic emission of unpolarized light. The angular momentum of the laser light stays with the atoms — there is a polarization transfer. As hyperfine interactions in the excited state may mix the electron and nuclear spins, the metastable sample gets nuclearly polarized. The nuclearly polarized metastable atoms may de-excite and their nuclear polarization may not be preserved, but their nuclear polarization is transferred from the metastable to the ground state via metastability exchange collisions. Here the electron clouds between atoms may be

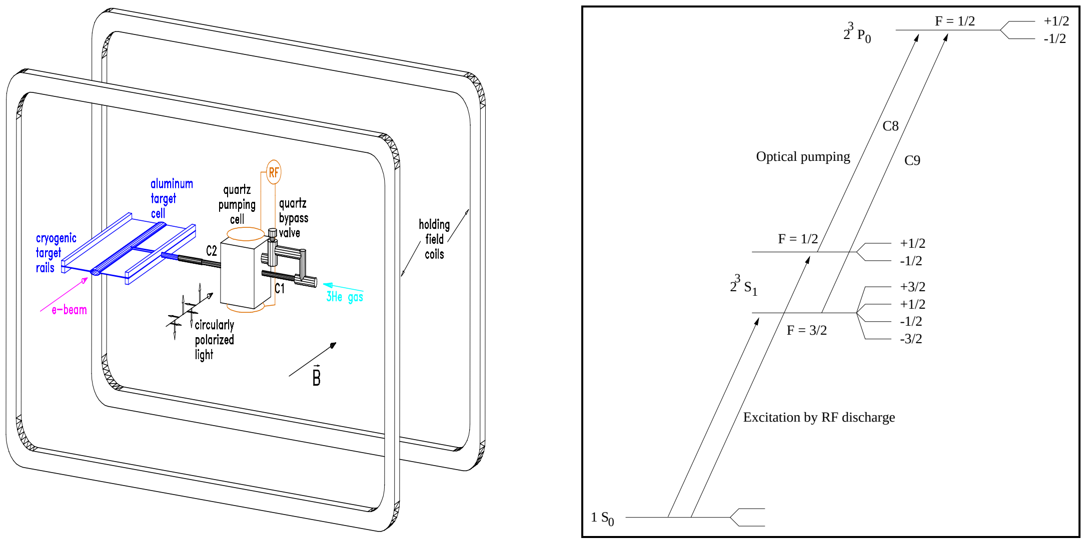

Figure 3.6: The ^{3}He target. Left is a schematic diagram of the target. ^{3}He atoms flow through a polarizing quartz cell and into the storage cell. The right diagram depicts the electron energy level structure in ^{3}He. RF transition populates $2^3\mathrm{S}_1$. Optical pumping induces the transitions to the $2^3\mathrm{P}_0$ state.

---

exchanged, so the small population of metastable atoms exchange their electron clouds with the larger population of stable atoms. In this way, stable polarized nuclei remain and flow into the storage cell [8]. The orientation of a slight magnetic field surrounding the target area determines the axis of the nuclear spin; the target polarization is reversed by reversing the sign of the circular light polarization. Reversal takes nearly one minute and is typically made every ten minutes.

The final target polarization of the ^{3}He target is measured in two ways. In the Pump Cell Polarimeter (PCP), the circular polarization of light emitted from the pumping cell by the de-excitation of electronic states is detected by a photomultiplier tube after passing through a quarter-wave rotation plate and a linear polarizer. The circularly polarized light creates a sinusoidal signal in the optical system whose amplitude is proportional to the nuclear polarization in the pumping cell. As the relaxation of nuclear polarization of ^{3}He is slow, this measurement is sufficient to measure the nuclear polarization in the storage cell.

A second and independent way of measuring the ^{3}He nuclear polarization is provided by the Target Optical Monitor (TOM). The TOM measures the polarization in the target cell by detecting circularly polarized light emitted by atoms who have been excited by Coulomb interaction with the positron beam. As in the PCP, this light is directed to an optical system to measure the nuclear polarization of the target. The two methods give compatible results [7].

The HERMES ^{3}He target typically reaches polarizations near 50%. The target's areal density is limited to 10^{15} nucleons/cm^2 to minimize effect on the positron beam lifetime. A more detailed description of this target can be found in Reference [7].

3.2.2 ^{1}H Target

In 1996 the ^{3}He target was replaced by the polarized Atomic Beam Source (ABS) which provided a polarized proton target in 1996 and 1997. The layout of the ABS and its Breit-Rabi Polarimeter (BRP) can be seen in Figure 3.7. In the ABS dissociator, strong radio frequency (13.56 MHz) dissociates H_2 molecules into atomic Hydrogen. Collimators form an atomic beam directed into the target cell. A series of sextupole magnets polarize the electrons in the beam via Stern-Gerlach separation. High frequency magnetic fields induce hyperfine transitions which exchange electron and nuclear polarization. A final set of sextupole magnets focuses the beam into the entrance tube of the storage cell [9]. The target polarization can be reversed every second in this setup, but at HERMES, this is done on the order of once a minute to limit synchronization issues in data acquisition.

A superconducting magnet surrounds the storage cell with a 0.335 T solenoid field, providing a quantization axis for the nuclear spins. The target cell is also coated with Drifilm and water to minimize molecular recombination and randomization of nuclear spins from atom-wall interactions. The cell temperature is chosen to be ~100K, the lowest possible to maximize target density without causing substantial polarization degradation and recombination.

To measure the polarization in the target cell, the polarization procedure in the ABS is reversed in the BRP. A sample of gas flows from the storage cell out an extraction tube across the beam from the injection tube. A series of sextupole spin separates this gas. A beam chopper and quadrupole mass spectrometer measures the atomic signal. Hyperfine transitions before the sextupole magnets may be induced to alter the spin state of the

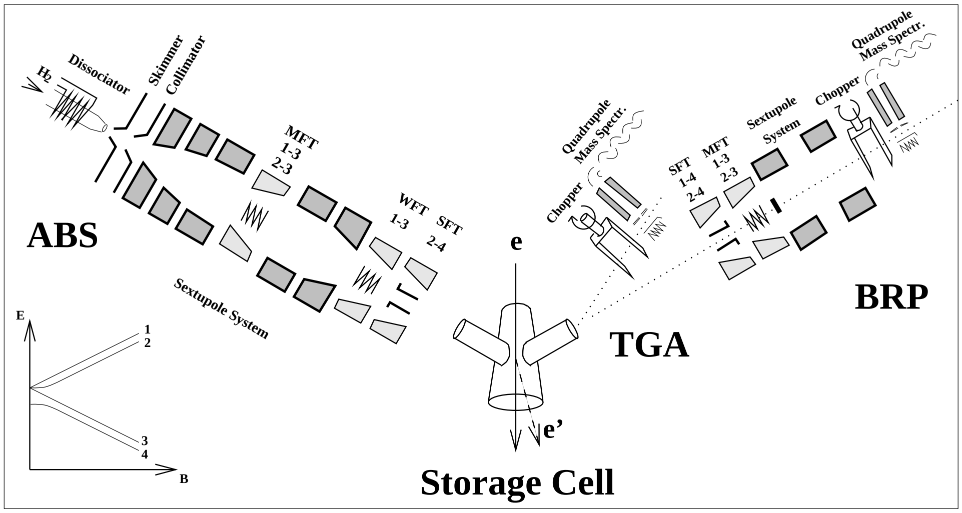

Figure 3.7: The ^{1}H target. The ABS dissociates and polarizes ^{1}H. The atoms flow into the storage cell. A sampling tube allows atoms to be extracted from the cell to be analyzed in the BRP and TGA mass spectrometer.

---

sample beam, yielding a different beam flux. Four independent flux measurements may be achieved to determine the occupations of the four possible electron and proton spin states. Simultaneously, a portion of the sample beam from the target cell is directed to the Target Gas Analyzer (TGA). The TGA uses a mass spectrometer to measure the relative flux of atomic and molecular hydrogen in the target cell [10].

The polarization of the target can then be calculated

$$P_T \;=\; \alpha_0 \left[\alpha_r + (1-\alpha_r)\beta\right] P_T^{\mathrm{atom}}. \tag{3.3}$$

α_0 is the initial fraction of hydrogen atoms leaving the ABS, and is large, typically 0.99 ± 0.01. α_r is the fraction of atoms that do not recombine to molecules in the target cell, and β is the nuclear polarization of the recombined molecules relative to the nuclear polarization of the atoms, P_T^{atom}. This molecular polarization is generally unknown, and a significant portion of the target systematic uncertainty is attributed to it.

The TGA and BRP measure α_r and P_T^{atom} at only one sampled position in the cell. Monte Carlo simulations of diffusion and spin relaxation are used to determine the target parameters over the entire cell. The average areal target density is calculated to be $7.6 \cdot 10^{13}$ nucleons/cm^2. For 1997, the average target polarization was 0.88 ± 0.04.

3.2.3 Unpolarized Gases

HERMES has also taken data with unpolarized gases flowing into the target cell via direct gas feed. Scattering from unpolarized H_2, D_2, ^3He and N_2 molecules has been done at HERMES. These data are not analysed here, but the unpolarized data taking does allow study of the unpolarized model assumptions used in the polarized analysis. Unpolarized data taking statistics can be quickly accumulated as high target densities on the order of 10^{15} nucleons/cm^2 can be reached with a direct gas feed.

3.3 The Spectrometer

The large acceptance HERMES spectrometer was designed to simultaneously determine the inclusive kinematics of deep-inelastic scattering as well as scattered hadrons from such processes. There are two main systems of detectors, a tracking system and a particle identification system. The tracking system consists of drift and microstrip chambers positioned before and after a spectrometer magnet. They measure the trajectories of charged particles with the bending of the tracks in the magnet determining their momenta. The particle identification system consists of four detectors that employ different techniques for separating electron and positron tracks from those of charged hadrons. The Čerenkov counter additionally provides pion identification within the hadron sample.

Both HERA positron and proton storage rings run through the entire HERMES experimental area. For this reason, the HERMES spectrometer is designed in two identical halves, one above and one below the beam pipes. A side view of the detector is shown in Figure 3.8. Details on the HERMES spectrometer can be found in Reference [11]. A relatively short writeup follows.

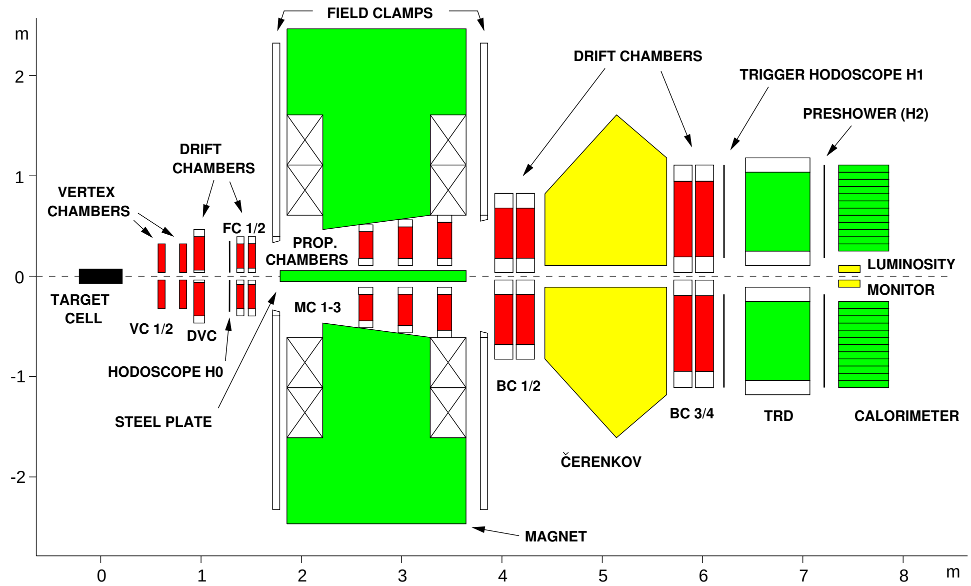

Figure 3.8: A diagram of the HERMES spectrometer.

3.3.1 Tracking System

The tracking system can be subdivided into three regions. The front region encompasses the region from the target cell to the spectrometer magnet. In the front region are the Vertex Chambers, the Drift Vertex Chambers and the Front Chambers, which work in concert to measure the scattering angles of charged tracks leaving the target. They also determine whether a track originates in the target cell or in material surrounding the target. The spectrometer magnet sits behind these chambers centered at 2.75 m from the target and bends the charged tracks in the horizontal plane. The interior of the magnet is the tracking system's magnet region, which contains the Magnet Chambers, which help measure the track deflection due to the magnetic field. Behind the magnet is the back region, which contains the Back Chambers, used to measure the magnet deflected tracks. These chambers not only determine the track momenta, but also determine where in each particle identification detector a track passes.

All planes in the tracking chambers are one of three types, with wires oriented either vertically (for X measurement) or tilted 30° right or left of vertical (U and V planes). The tracking system accepts particles scattered through an angular range of $40 \leq \theta_y \leq 140$ mrad and $-170 \leq \theta_x \leq 170$ mrad. Table 3.2 contains a summary of tracking chamber properties.

	Vertex		Drift Vertex	Front		Magnet			Back	
Detector	VC1	VC2	DVC	FC1	FC2	MC1	MC2	MC3	BC1/2	BC3/4
mm from target	731	965	1100	1530	1650	2725	3047	3369	4055	5800
Active area										
Horiz. (mm)	323	393	474	660	660	996	1210	1424	1880	2890
Vert. (mm)	137	137	290	180	180	263	306	347	520	710
Type	Microstrip gas		Horizontal drift	Horizontal drift		Proportional			Horizontal drift	
Chamber gas	DME/Ne		$Ar/CO_2/CF_4$	$Ar/CO_2/CF_4$		$Ar/CO_2/CF_4$			$Ar/CO_2/CF_4$	
Gas %	50:50		90:5:5	90:5:5		65:30:5			90:5:5	
Modules per half	1	1	1	1	1	1	1	1	2	2
Rad. length/module	0.8%		0.25%	0.075%		0.29%			0.25%	
Plane config.	VUX	XVU	$XX'UU'VV'$	$UU'XX'VV'$		UXV			$UU'XX'VV'$	
Wires in X plane	1674	2046	80	96	96	496	608	720	128	192
Wires in U,V plane	2170	2170	96	96	96	512	608	720	128	192
Resolution/plane	65 μm		220 μm	225 μm		700 μm			275 μm	300 μm

Table 3.2: Tracking chamber properties

Front Region

The Vertex Chambers (VC) are the first that an accepted scattered particle meets upon exiting the target cell. The VC must provide an accurate measurement of scattering angles while facing tight spatial constraints. To this end, the VC were designed as microstrip gas chambers. Each VC plane consists of a 300 μm thick glass substrate separated by 3 mm from a cathode foil plane. Each glass substrate is etched with alternating 7 μm aluminum anode lines and 85 μm cathode strips, as shown in Figure 3.9. The cathode plane and strips are kept at 1800V and 580V, respectively. The chamber is filled with a dimethyl-ether(DME)/Ne gas mixture to achieve a high gas gain. A resolution of $\sim$65μm is obtained with this technique. The VC planes in each half of the detector are grouped into two modules (VC1, VC2) of three planes each.

The VC suffered from low efficiency in 1995 due to problems with the electronics. Only half of the VC was operational throughout 1996, so track reconstruction including VC information has only been used since 1997.

The two Front Chambers (FC1, FC2) are located immediately in front of the spectrometer magnet, while the Drift Vertex Chambers (DVC) lie between the VC and FC. Both sets of these horizontal drift chambers improve the tracking resolution in the front region. Each drift chamber is comprised of six planes of alternating anode and cathode wires separated by cathode planes. The size of a drift cell is 7 mm in the FC and 6 mm in the DVC. The

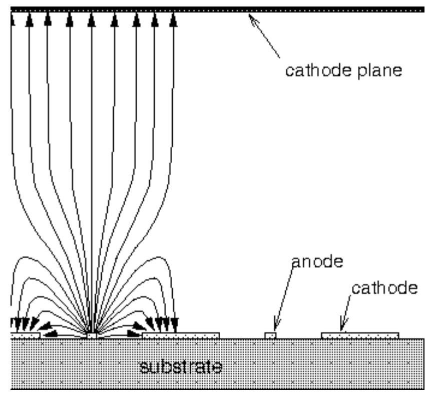

Figure 3.9: Schematic view of a drift cell in a microstrip gas counter, showing the field lines.

---

orientations of the planes are paired (UU', XX', and VV'), with the second plane of each pair offset relative to the first by half the drift cell size.

Because of the difficulties with the VC, the experiment relied on the FC alone for most of 1995 and 1996. This made tracking redundancy critical in the front region and so the DVC were proposed in 1995, and built and commissioned in 1997.

Magnet Region

The HERMES spectrometer magnet produces an integrated field of 1.3 T-m in the center of the spectrometer, with a variation in its deflecting power of less than 10% within the spectrometer's acceptance. An iron plate and correction coil prevent the magnet from deflecting the positron and proton beams. Field clamps on the front and back shield tracking detectors in the front and back regions from the magnetic field. A gap between the halves of this H-type magnet allows the beamlines through as well as scattered particles, and defines the angular acceptance of the spectrometer.

The Magnet Chambers are three (MC1, MC2, MC3) pairs of multiwire proportional chambers located in the gap of the spectrometer magnet. Originally designed to help in matching front and back region tracking information to create complete tracks, the MC were also found useful in detecting low energy tracks that are deflected out of the spectrometer acceptance without passing completely through the back region. Each chamber is comprised of three planes in a UXV orientation. Anode wires 2 mm apart are enclosed by two cathode foils in each plane.

Back Region

The back region contains only one type of tracking chamber, the Back Chambers (BC), which are used to determine the paths of charged particles after passing through the magnetic field. The BC are horizontal drift chambers identical in design to the FC, apart from a greater drift cell size of 15 mm. There are two sets of chambers (BC1/2, BC3/4) separated by the Čerenkov detector. Each set has two modules which each contain six planes: a total of 24 planes are active in the upper(lower) half of the detector.

3.3.2 Particle Identification System

Measuring deep-inelastic scattering processes requires the identification of the scattered lepton and coincident charged hadrons. The HERMES spectrometer particle identification (PID) system employs four sub-systems: a lead-glass calorimeter, two plastic scintillator hodoscopes, one of which is preceded by a lead curtain and acts as a preshower detector, a transition radiation detector, and a threshold Čerenkov detector. Each of these detectors responds differently to positrons and hadrons, allowing tracks to be distinguished as one or the other. The PID detectors are located in the back region of the spectrometer, so extrapolation of trajectories as determined by the back region tracking system is used to assign PID detector responses to tracks. A schematic diagram of these detectors is shown in Figure 3.10.

Čerenkov Detector

The HERMES Threshold Čerenkov counter utilized differences in Čerenkov radiation to identify particles. A particle travelling through a medium with a velocity faster than the velocity of light in the medium emits radiation (Čerenkov radiation) in a cone along the direction of the particle. For a particle of velocity $v = c\beta$ travelling through a medium with index of refraction n, the threshold for this type of radiation emission occurs when $\beta > \frac{1}{n}$.

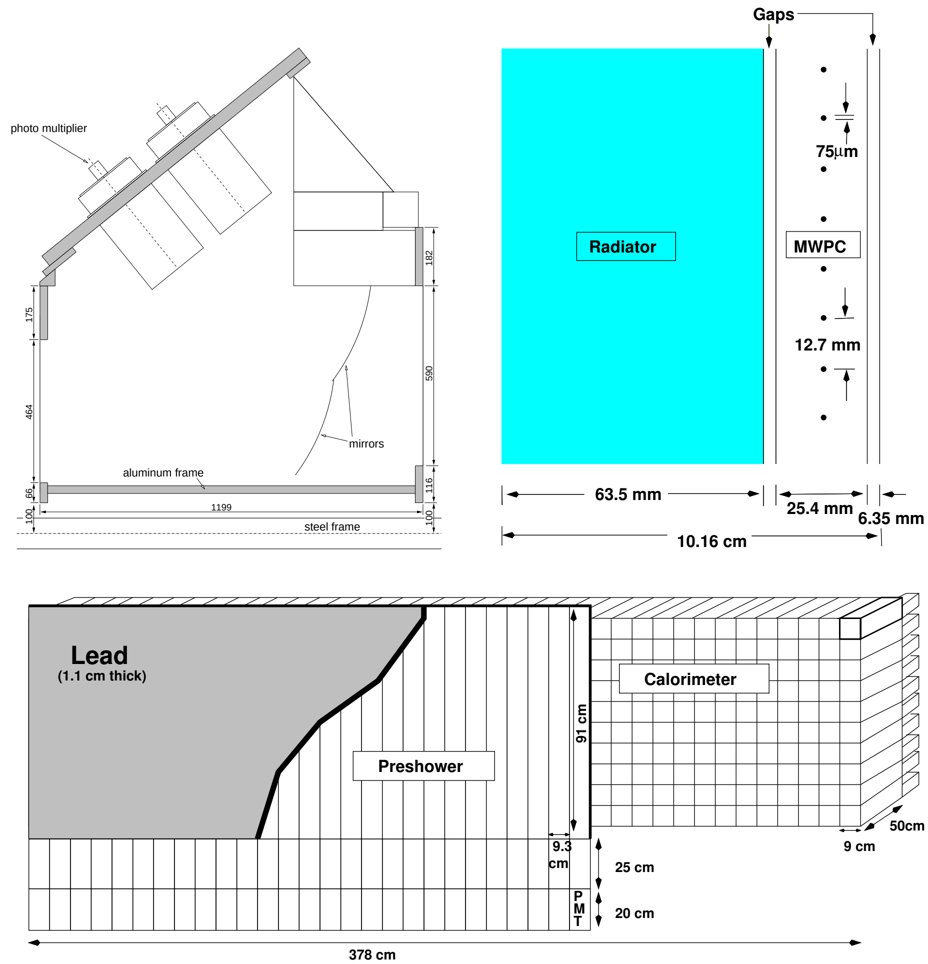

Figure 3.10: Schematic view of particle identification detectors: Čerenkov(top left), Transition Radiation Detector (top right), Preshower and Calorimeter (bottom).

For a given momentum (determined by tracking through the magnet), particles with lighter mass will have larger velocities, which may exceed the threshold for producing Čerenkov radiation. Whether or not a track is correlated with a signal in the Čerenkov detector can be used to constrain the mass of the particle.

1995–1997 saw the use of such a Čerenkov detector at HERMES. This detector used a 1.17 m deep volume of mixed nitrogen and C_4F_{10} as its radiator. As charged particles travelled through this gas, a system of 20 spherical mirrors focused any emitted Čerenkov light on 20 matching phototubes. In 1995, using pure nitrogen as the radiator yielded π,

K, and p momentum thresholds of 5.6, 19.8, and 37.6 GeV, respectively. For 1996(7), a 70:30 N_2:C_4F_{10} mixture lowered these thresholds to 3.8, 13.6, and 25.8 GeV. The detector cleanly identified electrons and positrons up to the pion threshold. Pions could be cleanly identified between their threshold and the kaon threshold, provided that the remaining PID detectors were used to separate radiation positrons and electrons in that range.

Transition Radiation Detector

Transition radiation is produced when a relativistic charged particle crosses a boundary between mediums with different dielectric constants ϵ. As opposed to the β-sensitive Čerenkov radiation, the mean energy of transition radiation scales with $\gamma = \sqrt{\frac{1}{1-\beta^2}}$. Photons are radiated forward with an energy on the keV scale. A 5 GeV positron has a γ of 10^4 and may radiate X-rays; a 5 GeV pion has a γ of only 36. Detection of high energy X-rays provides clean separation of positron/electrons from other charged particles.

The HERMES Transition Radiation Detector (TRD) is comprised of six identical modules per detector half. Each is built of a 6.35 cm thick radiator and a 2.54 cm thick X-ray detector. The radiator is made of loosely packed layers of polyethylene/polypropylene fibers of diameter 17–20 μm. The fibers provide a charged particle with a random matrix of dielectric transitions, producing transition radiation. The X-ray detector is a conventional multi-wire proportional chamber, containing a plane of 256 vertical anode wires separated by 1.27 cm, and between two cathode foil sheets. The chamber volume is filled with 90:10 mixture Xe:CH_4. While all charged particles deposit energy in a TRD module by gas ionization, positrons can be identified by the additional transition radiation signal.

Hodoscopes

Two hodoscopes (H1, H2) are installed in the back region to assist in triggering and particle identification. Both H1 and H2 consist of 42 vertical plastic scintillator paddles, each 9.3 cm wide. The paddles overlap by 1.5 mm to avoid acceptance gaps. In H2, each paddle is aligned with a column of lead-glass blocks in the calorimeter. Both hodoscopes are used in the HERMES trigger.

H2 also serves as a preshower detector for particle identification. H2 sits behind a 1.1

cm sheet of lead; while hadrons hardly produce showers in the lead wall, thereby producing only minimum ionizing signals in the scintillator, there is enough lead for positrons to produce showers that will deposit more energy in the scintillator. This becomes another means of separating positrons from hadrons.

A trigger hodoscope (H0) was installed in 1996 in front of the Front Chambers. Each consists of a single sheet of 3.2 mm thick plastic scintillator.

Calorimeter

The calorimeter, in the rear of the spectrometer, is a key component of both the trigger and the particle identification system. Each half of the calorimeter is a 42×10 array of $9 \times 9 \times 50$ cm blocks. These blocks are made of F101 lead-glass, selected for its resistance to radiation damage, and polished and wrapped in foil. Each block is coupled to a photomultiplier tube. As radiation near the beamline can damage the glass during injection of HERA, both halves of the calorimeter are mounted on a movable frame and can be moved 50 cm vertically away from the beam until a stable beam is available.

Identification of charged particles in the calorimeter relies on the difference in energy deposition between positrons and heavier particles. The depth of the lead-glass corresponds to 18 radiation lengths, so a positron striking the blocks will deposit nearly all of its energy inside. Hadronic energy loss is dominated by the nuclear interaction length, which is much longer than the radiation length. Less of a hadron's energy is lost in the lead-glass. Extrapolated tracks from the back region tracking can be correlated with energy deposits in the calorimeter; the ratio of deposited energy to track momentum is used to help separate positrons from hadrons. $\frac{E}{p} \sim 1$ for positrons/electrons but $\frac{E}{p} \ll 1$ for hadrons.

3.3.3 The Trigger

The trigger system at HERMES must make fast decisions concerning which signals are of interest for physics analysis, so that they can be selected from background with high efficiency and recorded by the data acquisition system. A first-level trigger is implemented in readout electronics and in programmable logic units, making use of discriminator signals derived from the hodoscopes, the Čerenkov counter, and the sums of signals from columns of calorimeter blocks.

Different triggers are used to record candidates for different physics processes. The DIS trigger records the state of the detector when the following criteria are met.

1. A high energy cluster must be found in the calorimeter, as these are likely to come from scattered positrons. The calorimeter energy threshold was set to 3.5 GeV in 1995, which corresponds to $y < 0.85$ for DIS events. This threshold was lowered to 1.4 GeV in order to accept higher y events.

2. A preshower (H2) signal above minimum ionizing is required. This further increases the chances of recording the scattered positron.

3. H0, H1, and H2 must all be present in the event. This suppresses showers from photons, which can create large signals in H2 and the calorimeter.

4. Signals in the hodoscopes must be time-ordered. The main background in the experiment comes from HERA's proton ring. Protons that leave the storage ring and hit the proton beam pipe can produce hadronic showers of high energy and create signals in the calorimeter and preshower. The relative timing of hodoscope signals is required to correspond to that of a relativistic positron travelling from the target to the calorimeter, passing through each hodoscope along the way. This suppresses the proton beam background. The H0 detector was installed in 1996 in the front region to provide a greater timing difference than was available with H1 and H2 alone.

The trigger electronics are able to determine if an event meets these conditions within 400 ns of the actual interaction in the target. A data acquisition system consisting of Fastbus crates connected to a cluster of DEC Alpha workstations collects digitized signals from each detector. The system collected triggered events at a rate of 150 Hz in 1995-1996. This was doubled to 300 Hz in 1997 by upgrading the workstations.

3.3.4 The Luminosity Monitor

In order to compare DIS cross-sections of different target spin states, it is necessary to monitor the luminosity with a physically independent and spin-independent process to correct for variations in target thickness or beam thickness and current. The HERMES luminosity monitor is designed to measure the rate of beam particles that scatter off the electrons of the target atoms, purely electrodynamic processes (Bhabha/Møller) that are well understood.

The luminosity monitor is two calorimeter modules that flank the beampipe in the horizontal plane, 7.2 m downstream of the target cell. Each calorimeter module is a 3×4 array of $NaBi(WO_4)_2$ crystals, each coupled to a photomultiplier. The modules are small enough to fit into the gap of the main calorimeter and can be moved 20 cm horizontally away from the beampipe during injection. The detector measures coincidences between the beam positron and the target electron.

From 1996 on, the luminosity monitor was used for a second purpose. As Bhabha scattering is spin-dependent, the luminosity monitor was used as a check on the calibration of the target's Breit-Rabi Polarimeter by periodically operating the Atomic Beam Source in a mode of high electron polarization. The luminosity monitor would see an asymmetry in its calorimeters, a measure of the average electron polarization in the target cell.

3.3.5 The Gain Monitoring System

The gain stabilities of the photomultipliers in the calorimeter, preshower and luminosity monitor are checked continuously by the Gain Monitoring System (GMS), which was built and maintained by the University of Illinois contingent of the HERMES Collaboration. The GMS sends light pulses of varying intensity to the experimental photomultipliers as well as an array of reference detectors via a fiberoptic network. The responses of the detectors to those pulses is measured in the same way as pulses from incident particle radiation. The responses of the experimental detectors are compared to the references and relative gains are calculated.

Light Source

The GMS light source is a Nitrogen Laser which produces pulses of light at 337 nm when triggered. The laser is aligned so that it fires upon a cuvette of organic dye which fluoresces at a peak wavelength of 500 nm (range 473–547 nm). Optical filters are located near the edge of a filter wheel placed directly in front of the laser to vary the intensity of the outgoing pulses. This allows the GMS to monitor possible non-linear response of the tubes. Eight filter positions are available, but only five are used, the remaining three are empty, passing the full intensity of the light pulse to the fiberoptic network. The response of a reference photodiode to the laser can be seen in Figure 3.11, along with the response of a detector vs. the same reference.

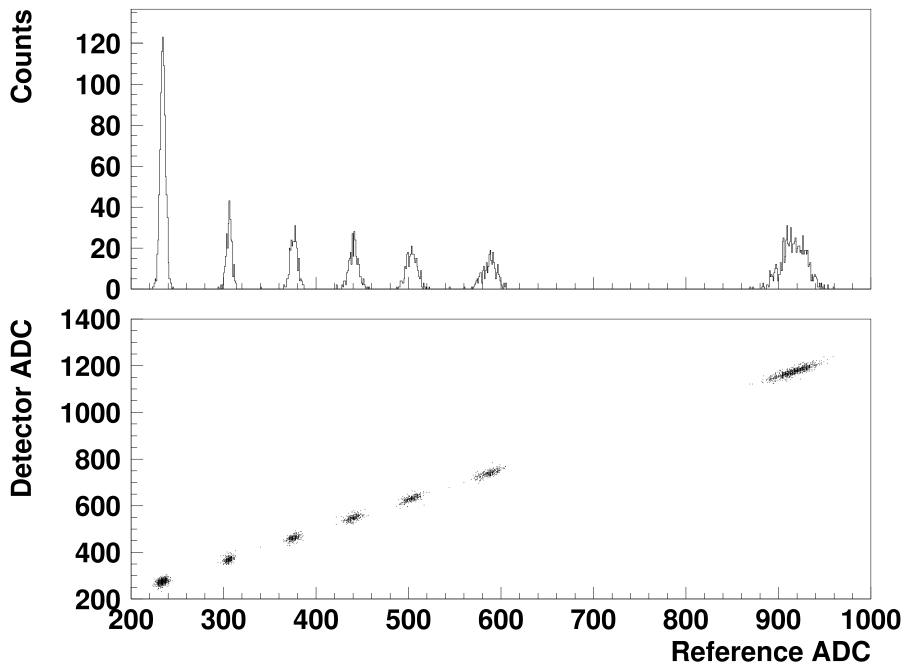

Figure 3.11: Response of a reference photodiode to the GMS laser (top) and response of a monitored detector vs. the same photodiode (bottom). The first peak shows the baseline responses of the detectors.

GMS Trigger

The filter wheel is used to determine when the laser fires — firing is allowed only when a filter rotates into position. Care must be taken to ensure that the GMS laser does not fire during a physics event, as an illumination of the entire calorimeter wall and preshower plane would ruin the recorded event for physics analysis. To this end, electronics are used to ensure that the laser is triggered only during coincidences of a laser filter being in position and the 1.6 μs gap in the bunch structure of the beam (once per orbit) entering the experimental area. As the actual laser pulse may jitter in time relative to this trigger, a separate data acquisition trigger is generated by a photomultiplier which receives unfiltered light from the laser via a short length of optical fiber. The GMS nominally operates at a trigger rate of 3 Hz, defined by the speed of the filter wheel. A separate Čerenkov gain monitoring system uses the GMS timing electronics to fire the LEDs in their own system.

Fiberoptic Network

The light is sent through a fiberoptic network for delivery to the 840 calorimeter photomultipliers, the 84 of the preshower, and the 24 of the luminosity monitor. Simultaneously, the light is split and sent to an array of photodiodes.

The laser light, after passing through the filter wheel, is projected into a single fiber which transmits the light to a commercially purchased 1:16 splitter. Each of the 16 outputs of this splitter is separately attenuable to allow appropriate light delivery to the monitored detectors. The light is routed directly from this splitter to the monitored detectors by a network of custom Illinois-built splitters and commercially purchased splitters as shown in Figure 3.12.

Software

Relative gains of the monitored detectors are calculated by fitting a straight line to the responses to the GMS light pulses of the detectors versus the reference photodiodes. The fits are also constrained to pass through the origin, defined by the average baseline responses of the detector and reference used in the fit.

This is done both online for immediate feedback, and offline for use in data quality determination. Offline, precise gains are calculated once per run ($\sim$10 m) and crude gains are calculated once per data record ($\sim$10 s) using software integrated into the data production scheme (Sec. 4.1.2). The crude, low statistics gain measurements are calculated to be used in the determination of data quality. Although gain corrections were never implemented, as the monitored tubes have been extremely stable, the online calculation of gains has proven the GMS very useful as a "trip" detector or high voltage monitor for the monitored detectors. As a crude gain can be calculated quickly, this is done and displayed graphically in the

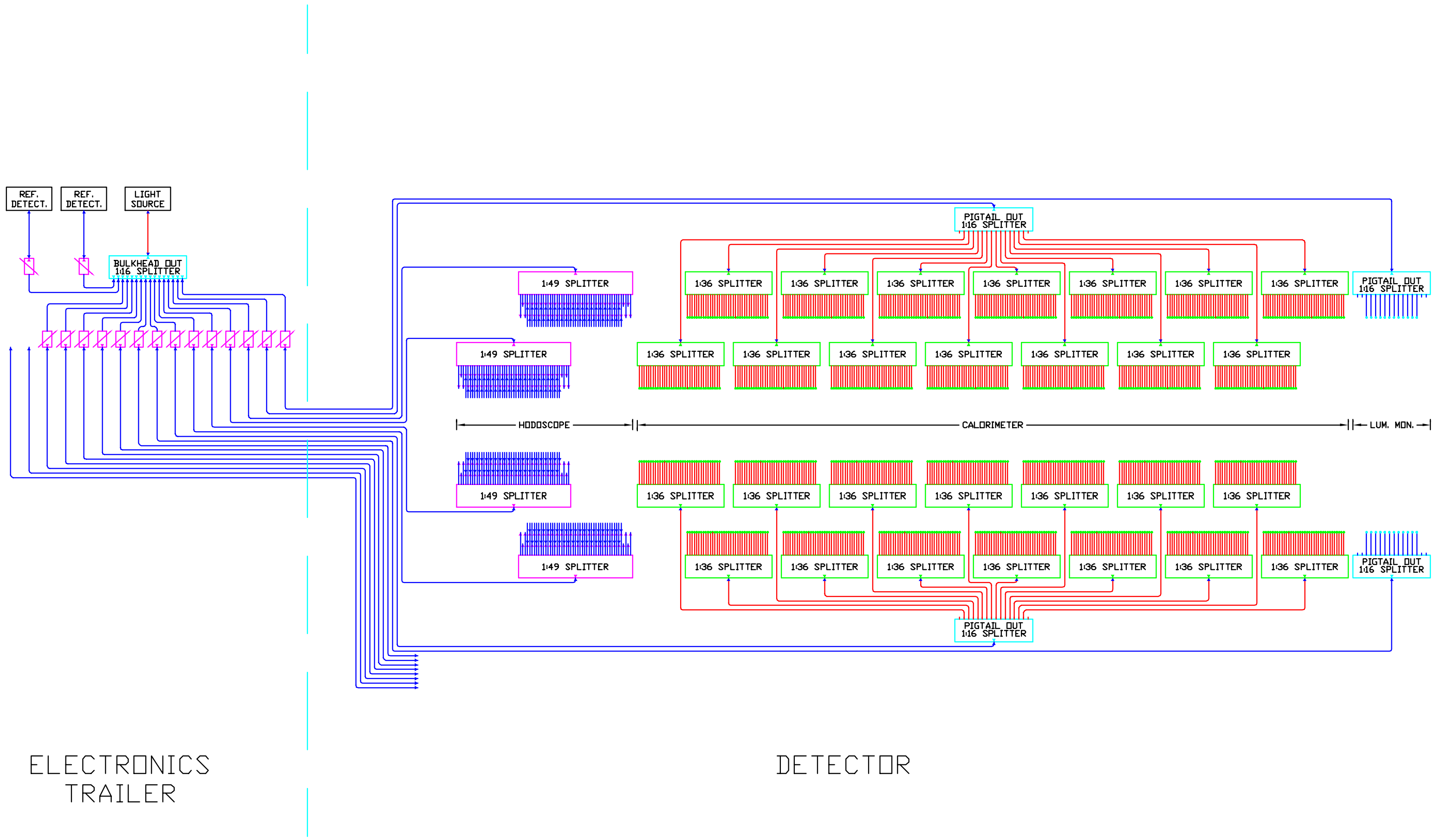

Figure 3.12: GMS fiber network.

HERMES control room on the order of once a minute, providing the status of the monitored tubes (Figure 3.13).

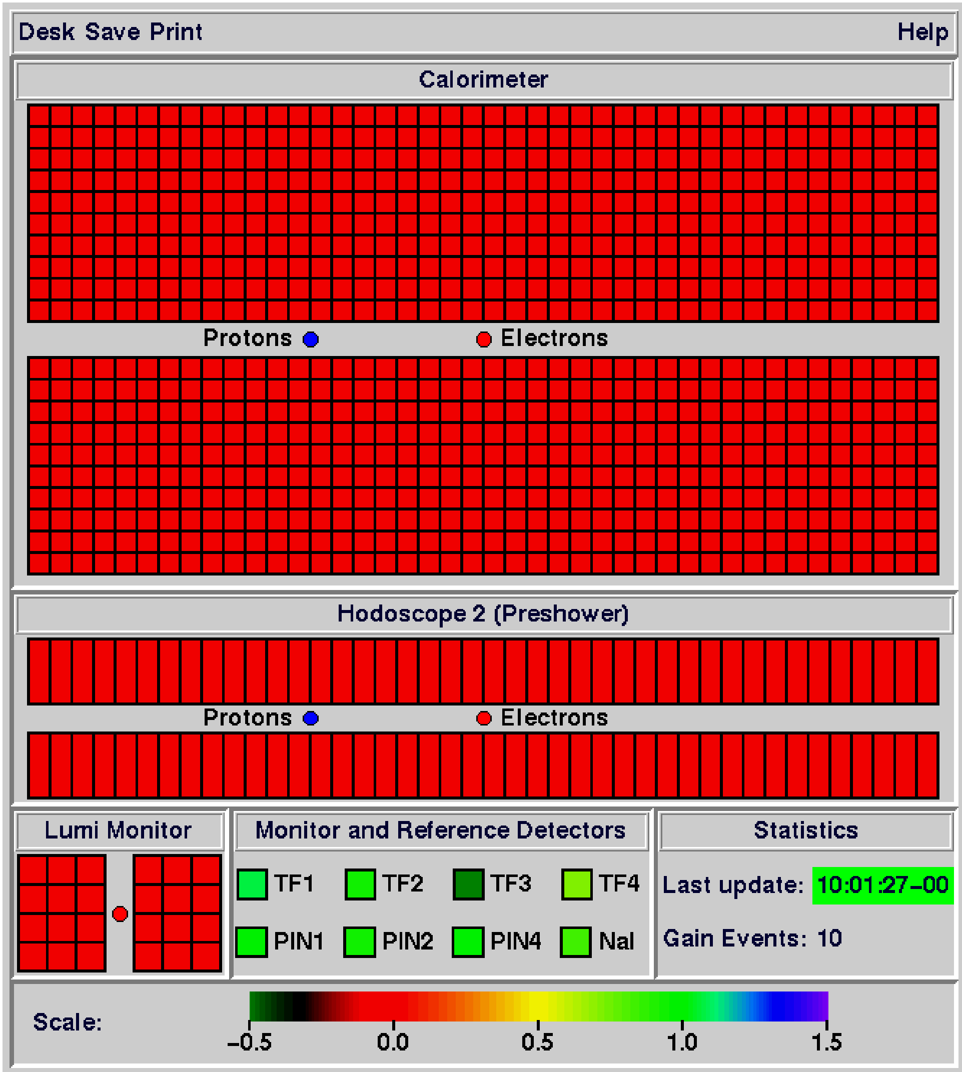

Figure 3.13: GMS online display

References

[1] A. Sokolov and I. Ternov, Sov. Phys. Doklady **8**, 1203 (1964).

[2] M. Düren, The HERMES Experiment: From the Design to the First Results, 1995, DESY-HERMES-95-02.

[3] V. Bargmann, L. Michel and V.L. Telegdi, Phys. Rev. Lett. **2**, 435 (1959).

[4] D. Barber *et al.*, Phys. Lett. B **343**, 436 (1995).

[5] W. Lorenzon for the HERMES Collaboration, 1995, Proposal to DESY for a Longitudinal Electron Polarimeter at HERA - East Section.

[6] W. Lorenzon (on behalf of the HERMES Collaboration and the HERA Polarimeter Group), in *Polarized Gas Targets and Polarized Beams — Seventh International Workshop* (American Institute of Physics, Woodbury, New York, 1997), pp. 181–190.

[7] D. DeSchepper *et al.*, Nucl. Instrum. Methods A **419**, 16 (1998).

[8] D. DeSchepper, Ph.D. thesis, Massachusetts Institute of Technology, 1997.

[9] J. Stewart (for the HERMES Collaboration), in *Polarized Gas Targets and Polarized Beams — Seventh International Workshop* (American Institute of Physics, Woodbury, New York, 1997), pp. 69–78.

[10] B. Braun (for the HERMES Collaboration), in *Polarized Gas Targets and Polarized Beams — Seventh International Workshop* (American Institute of Physics, Woodbury, New York, 1997), pp. 156–161.

[11] HERMES Collaboration, Nucl. Instrum. Methods A **417**, 230 (1998).

4

Data Analysis

The extraction of meaningful physics from the terabytes of data that the HERMES experiment records is a large task. The raw data, a record of detector states during varying time periods, is reduced and interpreted via a series of steps. Decoding and reconstruction software is used to convert the raw spectrometer signals into physical quantities. These derived quantities are then examined to determine the periods of data suited for further analysis. Systematic uncertainties are minimized without the undue sacrifice of statistical uncertainty — data in which detector instabilities will undermine confidence in extracted physics are removed. The selected data are used to generate the fundamental experimental results, the double-spin inclusive and semi-inclusive asymmetries on ^{1}H and ^{3}He targets.

4.1 Processing the Data

4.1.1 Data Structure

All detector signals associated with one trigger of the data acquisition is considered one event. The signals in the detector correspond to an interaction of one bunch of HERA positrons with the HERMES target, and they may be reconstructed to represent an interesting physics event.

The data acquisition system groups events into bursts, associating a burst number with every ten seconds of recorded events. These bursts may or may not be subdivided into polarization records, a delineation of different target polarization states. When the target state is unchanging over a burst, the burst and polarization record are identical, but during a target spin flip, a burst can contain two or three polarization records. Each polarization record or burst is also tagged with the scaler values (e.g., luminosity and polarization) that correspond to its period.

Roughly ten minutes of bursts (~450MB of raw data) are grouped together to form a run, the basic unit of data storage. HERMES collects and saves data runs during HERA lepton beam fills (when HERA's leptons are fully injected and ramped to full energy), which typically last eight hours. These fills are separated by the calendar year in which they were taken, since each year coincides with a different target and detector configuration, as hardware maintenance and upgrades are typically scheduled in December/January.

The raw data are formatted online using the Experimental Physics Input Output (EPIO) package [1]. Offline, HERMES software reframes the data into a tabular format using the ADAMO package [2], which provides a more accessible format for experimental information.

Two other software packages developed at HERMES assist the data collection and analysis. The Distributed ADAMO Database (DAD) [3] extends ADAMO by separating data streams using a client-server model. DAD allows central maintenance and efficient transfer of critical HERMES information.

4.1.2 Data Production and Offline Analysis

HERMES data "production" is the assembly-line of software packages designed to reduce the large EPIO run files into concise summary files. The raw detector responses (ADC, TDC values) are converted into physically meaningful quantities (positions, angles, energies, momenta).

The production has several stages, schematically pictured in Figure 4.1. Before any processing of the EPIO run files, DAD servers are filled with expert detector information, such as calibrations of detector responses and physical geometries and alignments of detector components. A software package called the HERMES Decoder (HDC) draws on the alignment and calibration DAD servers while reading the raw ADC and TDC signals from the EPIO run files in order to convert them to hit positions in wire chambers and energy depositions in various detectors. These resultant quantities are written in ADAMO format; the output is forwarded on to the next software package in the production chain - the HERMES Reconstruction Code (HRC) [4]. HRC uses the hit patterns in the tracking chambers to lay out particle trajectories. The scattering angle and momentum of each track are determined

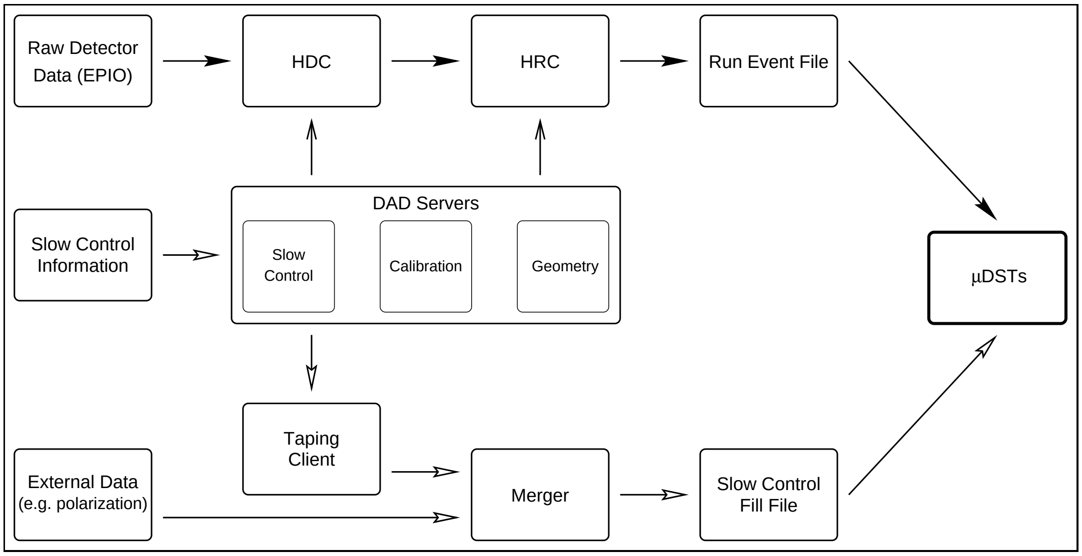

Figure 4.1: Schematic of HERMES data production flow. Solid arrows denote flow of event data, open arrows the slow control information, and wire arrows the static detector information.

---

and correlated with responses in the particle identification detectors. The HRC output, also in ADAMO format, still contains much raw calibration and reconstruction performance information, in addition to the newly calculated track information. While the program ACE (Alignment, Calibration and Efficiency) [5] uses this to calculate chamber calibration and tracking efficiency, the main production filters the essential physics information out of the HRC run file into a small Data Summary Tape (μDST) for each run. Data quality studies and physics analyses principally use the μDST information. New μDSTs are produced when better detector understanding leads to new calibration files. Those used in this thesis are versions 95e5, 96c1, and 97b2, for the years 1995, 1996, and 1997, respectively. These are the same production versions used in the published HERMES final results in References [6, 7, 8]. Finally, the μDSTs are processed by a custom software package written in C and FORTRAN by the author to effect physics studies, including those found in this thesis.

4.1.3 Track Reconstruction

The most important step in the data production chain described above is the track reconstruction. The volume of HERMES data requires a fast, efficient algorithm without sacrificing a high precision in the determined track parameters. The algorithm is reviewed here and described in detail in Reference [4].

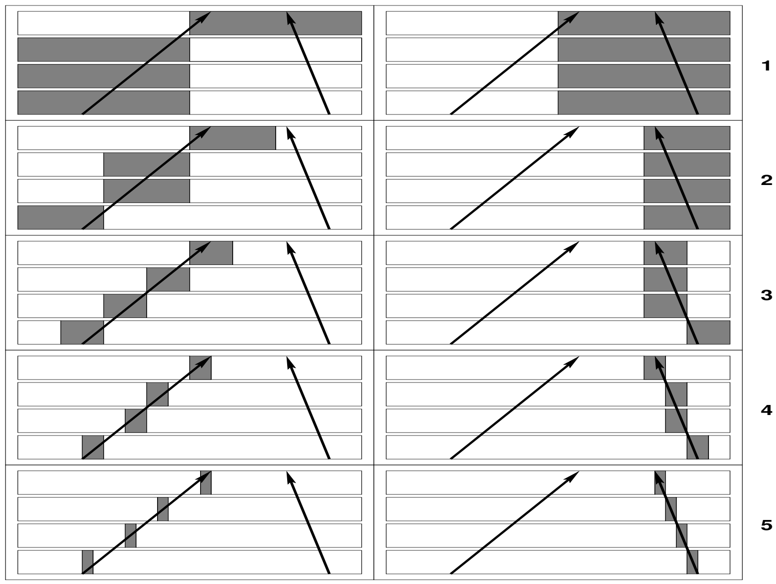

Figure 4.2: The treesearch method for two tracks. The detector pattern is matched iteratively with the resolution doubling each iteration. The arrows show the actual trajectory of the particles in the above schematic diagram.

HRC uses a treesearch algorithm to identify particle trajectories, as shown in figure 4.2. Hits in the detector are digitized into a bit pattern. This pattern is compared to patterns in a database containing all possible hit combinations resulting from real particles. The iterative track search first begins by determining which half of the detector the particle has traveled through. This coarse resolution is refined by a factor of two on each iteration, until the path of the particle is well localized. While over 100 million patterns for particle tracks are possible at Hermes, symmetry arguments reduce the number of stored patterns to a more manageable 31,000. Once the particle's path is determined, a straight line track is fit to each detector hit in the path by least squares minimization.

This treesearch is implemented for each spatial direction of the Hermes tracking chambers (u,v, and x) and for both the front and back (relative to the magnet) regions of the detector. The resultant spatial projections are combined to form a three-dimensional straight line trajectory in each half. These front and back partial tracks are connected, or bridged, in the center of the HERMES spectrometer magnet in order to form full trajectories.

There are two main methods of bridging front and back partial tracks to create full tracks. The standard ('STD') method extends the partial tracks to the center of the magnet. The distance between front and back partial tracks is required to be less than 1.0 cm at the center of the magnet in order to be combined to make a full track. In the 1997 analysis, this method was used with the Vertex Chambers (VC). In 1995 and 1996, however, the VC efficiency and operation was too poor to be used in the tracking. Only Front Chamber (FC) hits were available to determine front partial tracks; the FC's worse resolution, as compared to that of the VC, limits the 'STD' reconstruction efficiency in these years. The efficiency was improved, however, by iteratively varying front track trajectories while assuming the back partial tracks are fixed precisely. This forced-bridging technique (or 'NOVC') significantly improves full track resolution in these years.

Once a full particle trajectory is determined by HRC, the particle's momentum can be determined. HRC converts the particle's bending in the magnet into a momentum by consulting a lookup table and a map of the spectrometer's magnetic field.

The last step of track reconstruction extends the determined tracks through each particle identification (PID) detector and through the HERMES target. Each PID detector's responses which spatially correlate to the extrapolated track positions are assigned to that track. Similarly, the closest approach of the extended trajectory in the target region to the positron beam is considered the most likely production point of that particle.

4.2 Data Quality

Perhaps the most critical step in analyzing the data is the determination of its quality, or its suitability for physics analysis. The HERMES experiment consists of a number of independent subsystems, all of which are required to be operational for accumulated data to be used in a valid analysis. Data taken during a time when a component of the experiment is improperly working can be cut to eliminate systematic biases in the result. At the same time, such cuts must be applied carefully to maintain high statistical precision. The data quality is evaluated on the aforementioned time scales of the fill, run, burst and record.

4.2.1 Fill and Run Quality

Data analysis begins, of course, on the coarsest convenient time scale, which is that of the HERA positron fill. Over the course of each fill, the experiment runs undisturbed. Between fills, changes in the experimental configuration, either hardware or software, can be implemented, necessitating a review of fill conditions to determine whether or not a fill's data should be used in a particular analysis. For example, some fills are taken with the target containing unpolarized gas. For the analysis in this thesis, those fills are not included.

The next level of data evaluation is the run level. Experts responsible for the operation of the target, beam polarimeters, and the many spectrometer components identify the runs when their equipment did not deliver data appropriate for HERMES analysis. The failure of a single component can be enough to invalidate the use of an entire run in physics analysis. The most catastrophic example for polarized physics analysis is the failure of the beam polarimeters to measure the beam polarization. Measurement of spin-dependent cross-sections is then impossible. The HERMES data-taking logbook is also scanned to produce lists of runs which are unusable due to hardware failures.

4.2.2 Burst and Record Quality

Bursts and records are the smallest time scale on which data evaluation can be done. The status of the entire experiment is recorded on the burst level, and so most data quality evaluation is focused here. Bursts and records are identical except during a change of the target polarization state, and will be used interchangeably.

Discussion of the burst quality is conveniently divided into sections detailing quality of the beam, target, luminosity measurements, the data acquisition system, and finally, the tracking chambers and particle identification detectors. As HERMES evolved over the years 1995–1997, so did understanding of the equipment, and also therefore, the data quality strictures.

Beam Performance

To achieve high statistical precision in DIS, intense and stable beam currents are required. Polarized DIS further requires stable, high, well-measured beam polarization. Beam current and polarization are forced to remain within a reasonable range of nominal HERA values for each running year. Beam polarization was measured each minute; the points were smoothed by a cubic spline, and small gaps in the measurement interpolated. Large gaps were not included in the analysis. Expert data quality cuts required at least one full operational beam polarimeter. Lower limits on both beam current and polarization were also implemented. See Table 4.1 for exact cuts.

Target Performance

Just as in the case of the beam, the ideal target has both high density and polarization, and is stable over the course of the running period. The target must have a well-defined nuclear polarization state, which must be parallel or anti-parallel to the beam polarization. With the Atomic Beam Source (ABS), used in 1996–7, only periods when the target gas was only nuclearly polarized passed data quality selection. Periods where the target gas was toggled through states with defined electron polarization (so the luminosity monitor could crosscheck calibration of the target's Breit-Rabi polarimeter) may cause luminosity asymmetries from higher residual electron polarization, and are rejected.

Target polarization and density were required to remain within a certain range. With ^{3}He, the target polarization was measured with the Pumping Cell Polarimeter. During a period when this failed, Target Optical Monitor fill-averaged values were substituted. Target expert-provided lists were used to separate polarized target runs from unpolarized, and to remove periods of hardware failure. Exact cuts are listed in Table 4.1.

Luminosity

The HERMES luminosity monitor detects coincident Bhabha scattering of beam positrons off target electrons. This measurement is used to provide relative normalizations to measured DIS rates. The rate of Bhabha scattering is also a test of HERA positron beam stability. For each target, this rate is required to remain in a nominal operating range. Residual electron polarization in the hydrogen atom sample may produce a small asymmetry in the measured Bhabha rates in the two target spin states, but this bias is removed by averaging across target spin states.

Required Beam Conditions	
1995:	
Current	$8 \text{ mA} < I_{e_+} < 32 \text{ mA}$
Polarization	$40\% < P_{e_+} < 70\%$
1996–7:	
Current	$8 \text{ mA} \leq I_{e_+} \leq 50 \text{ mA}$
Polarization	$30\% < P_{e_+} < 80\%$
Required Target Conditions	
1995:	
Density (nucleons/cm^3)	$0.85 \cdot 10^{15} < \rho_{^3\mathrm{He}} < 1.5 \cdot 10^{15}$
Polarization	$30\% < P_{^3\mathrm{He}} < 60\%$
1996–7:	
Polarization	$70\% < P_\mathrm{p} < 99\%$
Atomic Fraction	$\alpha_0 > 0$ and $\alpha_R > 0$
Required Luminosity Conditions	
1995:	
Lumi Monitor Rate	$40 \text{ Hz} < R_\mathrm{Bhabha} < 210 \text{ Hz}$
Luminosity Ratio: $\frac{\text{Lumi Rate}}{\text{density}\cdot\text{current}}$	$5 \cdot 10^{-15} < \frac{R_\mathrm{Bhabha}}{\rho_{^3\mathrm{He}} \cdot I_{e^+}}$
1996–7:	
Lumi Monitor Rate	$5 \text{ Hz} \leq R_\mathrm{Bhabha} \leq 60 \text{ Hz}$
GMS	No Dead Blocks

Table 4.1: Conditions required for beam and target record data quality

In 1995, while running with the ^{3}He target, another independent measure of the luminosity was used — the beam current times the target density. In 1995, the ratio of two luminosity measurements is required to be nearly constant. This requirement could not be imposed in 1996–7, because of the lack of direct measurement of the target density in the ABS.

Finally, the Gain Monitoring System (GMS) was used to monitor the response of the Luminosity Monitor calorimeter from 1996 onwards. The GMS compares the responses over time of the calorimeter blocks to a reference laser beam. All blocks were required to function properly, that is, without loss of gain. Cuts are detailed in Table 4.1.

Data Acquisition

Failures in the HERMES DAQ, which collects data prior to its offline processing, can leave the collected data unsuitable for analysis. Requirements are imposed to ensure that the quality of the collected data is not compromised by DAQ-related problems.

The length of a record (as introduced in Section 4.1.1) in seconds is a measure of the entire data-taking time spanned by that record. The "live time" of the DAQ during a record is a measure of the time that the DAQ is not busy and is able to collect events. The live time is defined as the ratio of accepted triggers to generated triggers,

$$\text{Live Time} = \frac{T_{acc}}{T_{gen}}. \tag{4.1}$$

The record length and the live time are multiplied by the luminosity to generate normalization factors for the experimental count rates. Cuts are placed on both record length and live time to ensure data acquisition efficiency and stability. See Table 4.2.

Required DAQ Conditions	
1995:	
Live Time	$.50 < \text{Live Time} < 1.00$
Record Length	$9s \leq t_{\text{record}} \leq 11s$
Initialization	Exclude first 3 bursts and last burst
1996–7:	
Live Time	$.50 < \text{Live Time} < 1.00$
Record Length	$0s \leq t_{\text{record}} \leq 11s$
Initialization	Exclude first and last burst
Synchronization	Exclude records with synch errors

Table 4.2: Conditions required for DAQ record data quality

The beginning and end of a data run (see Section 4.1.1) require a number of DAQ initialization and cleanup processes, which are CPU intensive. This typically reduces the live time, and can create erroneous timing in the event collection. For this reason, the first and last records of each run are excluded from analysis.

A last DAQ concern is that events (records) can be associated with the wrong target polarization state. Records with these synchronization problems can be detected and excluded, due to the large amount of redundant timing information stored in the records. Synchronization problems are found mainly in the proton data of 1996–7, when the fast polarization reversal of the target heightens the difficulty of proper timing.

Tracking Chambers

To extract physics from the recorded data requires that the tracking system of the spectrometer be reliably and efficiently running. Failures in the tracking chamber high voltages were detected in 1995 by calculating the tracking efficiencies in the front and back regions of the spectrometer. In 1996, the high voltage readbacks of the chambers were stored, allowing periods where there were Front Chamber and Back Chamber trips to be cut directly. In 1997, the Vertex Chambers were included in the tracking algorithm, and Vertex Chamber experts studied the detector performance to determine periods of hardware failure. See Table 4.3

Due to the top/bottom symmetry of the HERMES spectrometer, a detector may fail in one half of the detector but not the other. In semi-inclusive physics, a multi-track coincidence must be detected, requiring the full acceptance of the detector to be available. Both halves of the detector were required to be working for the semi-inclusive analysis in this thesis.

Particle Identification Detectors

Given accurate and reliable tracking, DIS studies require the ability to differentiate between leptons and hadrons. Stable operation of the particle identification (PID) detectors is mandated for both this reason and the fact that some of the PID detectors are used in the DAQ event triggers.

The GMS continually checks the responses of the calorimeter and preshower PMTs. Scaler counters connected to each hodoscope channel of H1 indicate whether or not the channel is on and is taking data. To evaluate the Čerenkov detector performance, a lepton identification efficiency was calculated (the efficiency of leptons identified in the Čerenkov). Experts from the Čerenkov and TRD groups identified bursts where these detectors were malfunctioning. See Table 4.3.

Overall Efficiency

After the above cuts, the 1995 data were still unsatisfactorily unstable. To improve the data quality further, periods when detector components were intermittently failing were excised. The principle behind this "Swiss-cheese" cut is that periods in which a particular detector is tripping frequently are suspected to be conditions unsuitable for a precision analysis. Due to marked improvement in detector stability, this cut was not imposed in 1996–7. See Table 4.3.

Required Tracking Chamber Conditions	
1995:	
Front Efficiency	$80\% < \epsilon_{\text{front}} < 100\%$
Back Efficiency	$94\% < \epsilon_{\text{back}} < 100\%$
Previous Burst	Reject burst before burst with trips
1996–7:	
High Voltage Trips	Reject bursts with FC and BC HV trips
1997:	
Vertex Chamber	Reject bursts in VC Expert list
Required PID Detector Conditions	
1995–7:	
Gain Monitoring System	Reject bursts with bad channels in calorimeter and preshower
Scaler Counters	Reject bad hodoscope channels
TRD DQ	Reject from TRD Expert list
Čerenkov DQ	Reject from Čerenkov Expert list
Required Overall Efficiency	
1995:	
Fraction of Gaps / Run	$\frac{n_{\text{gaps}}}{n_{\text{bursts}}} < 0.10$
Fraction of Good Records / Run	$\frac{n_{\text{good bursts}}}{n_{\text{bursts}}} > 0.40$
Good Records / Fill	$n^{\text{top}}_{\text{good bursts}} \geq 100$
(each detector half)	$n^{\text{bot}}_{\text{good bursts}} \geq 100$

Table 4.3: Data Quality conditions imposed on tracking chambers, particle identification detectors, as well as overall efficiency

Quality Summary

The numbers of records after data quality selection are listed by year in Table 4.4.

	1995	1996	1997
$\langle P_{\text{beam}} \rangle$	55.1%	52.3%	53.1%
$\langle P_{\text{target}} \rangle$	45.8%	81.8%	89.3%
Runs	2178	3308	7284
μDST Records, spin state $\uparrow\downarrow$	29913	82396	187158
μDST Records, spin state $\uparrow\uparrow$	29590	82406	186843

Table 4.4: Final Burst Summary

4.3 Event Selection

After the data quality selection is complete and the analyzable bursts are identified, the events in those bursts that represent inclusive and semi-inclusive DIS reactions must be selected. Algorithms utilizing the responses of the particles in the PID detectors are used to separate the scattered positrons from final state hadrons. Kinematic cuts on the detected positrons and coincident hadrons then define whether or not the event is DIS. A summary of the requirements over the years 1995–7 is given in Table 4.5.

4.3.1 Particle Identification

The four HERMES particle identification detectors — Calorimeter, Preshower, Čerenkov and TRD — each respond differently to the particles that enter them, as seen in figure 4.3. An algorithm that combines these responses was developed for convenient separation of leptons and hadrons.

Electron and Hadron Separation

Each PID detector's response, as seen in figure 4.3, can be used in a straightforward manner by the use of hard cuts on the individual detector responses near the intersection of their responses to electrons and hadrons. If this is done, the PID information of the components

Geometry	
Scattering vertex	
1995	$-30 < z_{\mathrm{vertex}} < 30$ cm
1996–7	$-18 < z_{\mathrm{vertex}} < 18$ cm
1995–7	$r_{\mathrm{vertex}} < 0.75$ cm
Angular acceptance	$40 < \|\theta_y\| < 140$ mrad
	$-170 < \theta_x < 170$ mrad
Direct calorimeter hit	$\|x_{\mathrm{calo}}\| < 175$ cm
	$\|y_{\mathrm{calo}}\| < 30$ cm
Particle Identification	
Identify leptons	
1995	$\mathrm{PID}_{95} > 2$
1996–7	$\mathrm{PID3} + \mathrm{PID5} > 2$
Identify hadrons	
1995	$\mathrm{PID}_{95} < -1$
1996–7	$\mathrm{PID3} + \mathrm{PID5} < 0$
Semi-Inclusive Hadron Selection	
Increase parton-hadron correlation	$z_h > 0.2$
	$x_F > 0.1$
Pion Identification	
Čerenkov response	$\langle$ photoelectrons $\rangle > 0.25$
1995	$5.6 < p_h < 19.8$ GeV/c
1996–7	$4.0 < p_h < 13.3$ GeV/c
Kinematics	
Ensure scaling region	$Q^2 > 1$ GeV^2
Avoid resonance region (inclusive)	$W^2 > 4$ GeV^2
Ensure factorization (semi-inclusive)	$W^2 > 10$ GeV^2
Minimize radiative corrections	$y < 0.85$

Table 4.5: Criteria for selecting DIS inclusive and semi-inclusive events and tracks

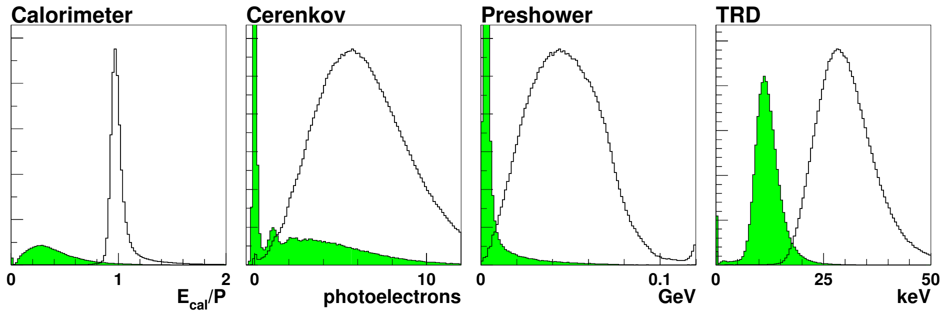

Figure 4.3: PID detector responses to DIS positrons (white) and coincident hadrons (shaded).

---

is independent and can be used for detector-specific studies. For data analysis, however, a more efficient and more complex method is used. For each detector, the conditional probabilities $P^{(i,R)}$ that particle i generates response R is defined, either by Monte Carlo techniques or test-beam measurements. These conditional probabilities $P^{(i,R)}$ are converted to true probabilities,

$$\mathcal{P}^i = \frac{\Phi^i P^{(i,R)}}{\sum_j \Phi^j P^{(j,R)}}, \tag{4.2}$$

where Φ^i are the average flux of particle i for given kinematics.

In the simple case where only electrons and hadrons need separation, Eq. 4.2 becomes

$$\begin{aligned} \mathcal{P}^e &= \frac{\Phi^e P^{(e,R)}}{\Phi^e P^{(e,R)} + \Phi^h P^{(h,R)}} \\ \mathcal{P}^h &= \frac{\Phi^h P^{(h,R)}}{\Phi^e P^{(e,R)} + \Phi^h P^{(h,R)}} \end{aligned} \tag{4.3}$$

For use in the analysis, taking the logarithm of the ratio of these electron and hadron probabilities gives a convenient particle identification parameter, or "PID."

$$\mathrm{PID} = \log\left(\frac{\mathcal{P}^e}{\mathcal{P}^h}\right) = \log\left(\frac{\Phi^e P^{(e,R)}}{\Phi^h P^{(h,R)}}\right) = \log\left(\frac{P^{(e,R)}}{P^{(h,R)}}\right) + \log\left(\frac{\Phi^e}{\Phi^h}\right) \tag{4.4}$$

As a PID parameter may be defined for each detector, combined likelihoods can be formed simply by adding together the detector-specific PID parameters, which is equivalent to the logarithm of the product of the detector-specific probability ratios of Eqs. 4.3. Parameters that are so defined are

$$\mathrm{PID3} \;=\; \mathrm{PID}^{\check{\mathrm{C}}\mathrm{erenkov}} + \mathrm{PID}^{\mathrm{Calorimeter}} + \mathrm{PID}^{\mathrm{Preshower}} \tag{4.5}$$

and

$$\mathrm{PID5} \;=\; \mathrm{PID}^{\mathrm{TRD}}. \tag{4.6}$$

The PID parameters are sensitive measures of particle type, but understanding of the particle fluxes Φ^i is required. If the flux ratios Φ^e/Φ^h have weak dependence on kinematics, however, then the second term in Eq. 4.4 only provides a constant offset to the distribution, and the logarithms of the ratios of the conditional probabilities is sufficient PID information. The PID parameters in this case have a simple interpretation: particles with positive PID are likely to be electrons, while particles with negative PID are likely to be hadrons. See Figure 4.4 for the PID3+PID5 distribution for 1997. In 1996–7, PID3+PID5 was used

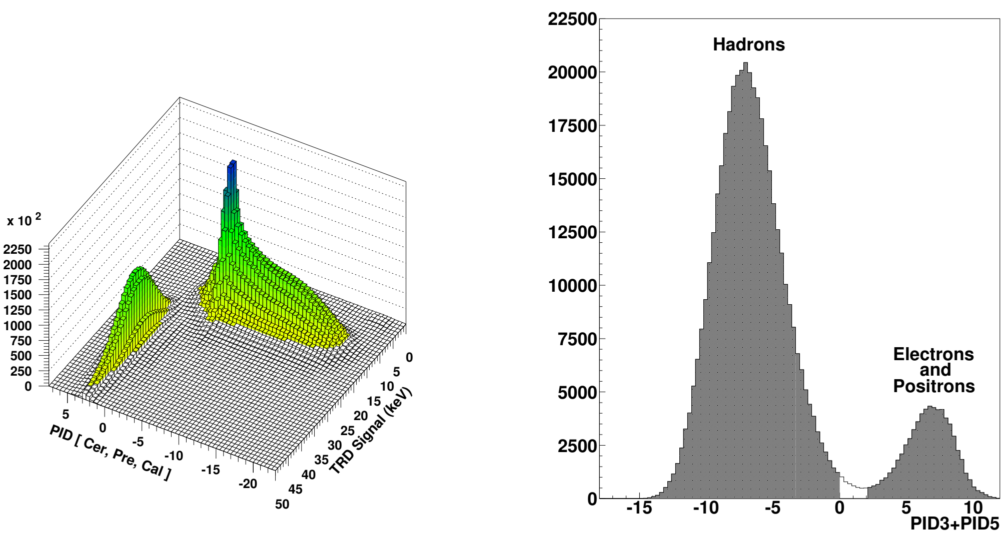

(a) 1995 (b) 1997

Figure 4.4: PID distributions for detected tracks in (a) 1995: PID3 vs. TRD mean response and (b) 1997: PID3+PID5

to separate electrons and hadrons. In 1995, however, this was not possible. The parent distributions for the TRD were not yet considered, so instead, a hard cut on the truncated mean TRD response and PID3 was used:

$$\text{PID95} = \text{PID3} + 0.31(\text{TRD}_{\text{mean}}) - 5.48. \tag{4.7}$$

Also, instabilities in the running year led to more frequent PID detector trips. When the TRD in particular failed, particle identification relied on only the other three detectors:

$$\text{PID95} = \text{PID3}. \tag{4.8}$$

Positron-hadron separation in 1995 is also shown in Figure 4.4. After implementation of the cuts in Table 4.5, hadron contamination of the positron sample is estimated at less than 1% [9]. A detailed description of particle identification at HERMES can be found in Reference [9].

Pion Separation

One of the advantages of the HERMES experiment is its ability to differentiate pions from the rest of the hadron sample using the threshold Čerenkov detector. Requiring identified hadrons with momentum between 4.0 and 13.3 GeV/c in 1996–7 to produce photoelectrons in the Čerenkov establishes a clean sample of pions. In 1995, due to a different Čerenkov radiator, the momentum window was between 5.6 and 19.8 GeV/c.

4.3.2 Deep Inelastic Event Selection

Identification of a positron or electron within an event completely defines the pertinent kinematic quantities (x, Q^2, W^2) of the event. Both positrons and electrons are considered, as the electrons are a measure of the charge-symmetric background, discussed further in Section 4.5.1. Kinematic cuts can be placed on the lepton to identify a deep-inelastic scattering sample.

Each lepton within an event is treated as the scattered lepton, thereby defining the event's kinematics. Cuts on vertex position, z_{vertex} and t_{vertex}, establishes that the track originated in the HERMES target cell. Angular cuts in θ_x and θ_y provide a check that the calculated track is indeed within the spectrometer acceptance. The even more stringent requirement that the track strike within the calorimeter limits ensures proper calorimeter PID information.

Physics cuts are placed on the lepton to achieve a DIS sample, as noted in Table 4.5. An upper limit on the kinematic variable y reduces the radiative corrections to the cross-section. The lower limit $W^2 > 4$ GeV^2 selects the events in the DIS region where the nucleon breaks apart incoherently, avoiding resonances. Finally, the requirement that $Q^2 > 1$ GeV^2 places the sample in a region where Bjorken scaling occurs. An appropriate binning in the Bjorken scaling variable x (to ensure good statistics per bin) is then determined. A diagram of such cuts is found in Figure 4.5.

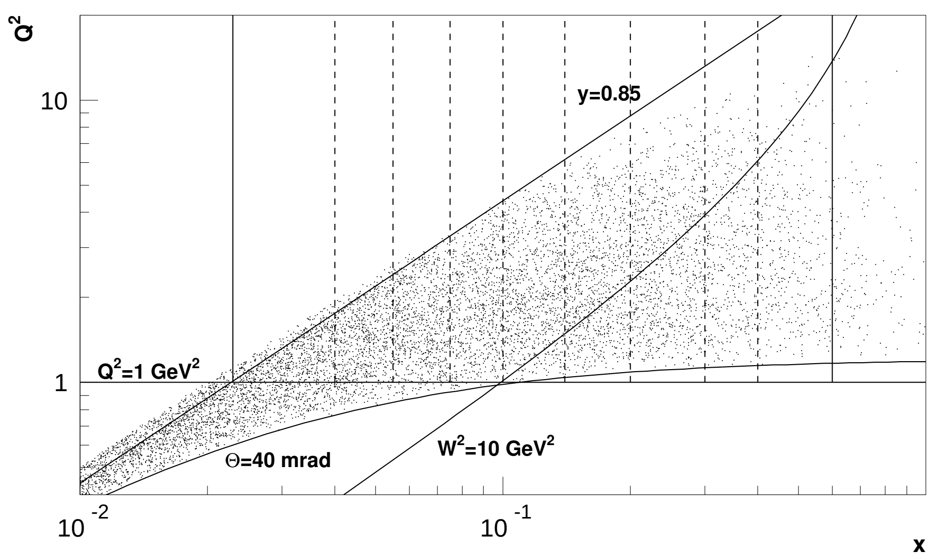

Figure 4.5: Distribution of events in HERMES in the x-Q^2 plane. Solid lines show the applied cuts in the semi-inclusive analysis. Dashed lines show the x-binning.

Semi-inclusive DIS requires events in which at least one hadron be detected in coincidence with a DIS positron. These events are then subsets of the inclusive DIS sample. In the analysis, factorization is assumed in the semi-inclusive process: the hadron fragmentation is separable from the scattering process. The higher limit of $W^2 > 10$ GeV^2 is imposed to ensure this.

Just as is required for lepton tracks, hadron tracks are required to originate in the target cell and remain within the spectrometer acceptance. Additionally, cuts on the fraction of the transfer energy carried by the hadron, $z > 0.2$, and the Feynman scaling variable, $x_F > 0.1$, maximize the correlation between the detected hadron and the quark struck in the scattering.

The events containing inclusive DIS positrons and electrons, as well as, in the semi-inclusive case, coincident hadrons (and pions, separately), are accumulated in each year of HERMES data-taking. The total yield for each particle type is found in Table 4.6.

	1995	1996	1997
e^+	2143301	720173	1552425
e^-	21784	10519	24218
h^+	269958	95109	207685
h^-	169666	54772	118760
π^+	15657	40832	91635
π^-	10848	28414	63118

Table 4.6: Particle yields for each running year.

4.4 Asymmetry Formation

After establishment of the event samples, the formation of the DIS double-spin asymmetry is straightforward. The number of events of a certain type h in the two relative beam-target spin states, $N^h_{\uparrow\Downarrow(\uparrow\Uparrow)}$, can be expressed as

$$\begin{aligned} N^h_{\uparrow\Downarrow}(x, Q^2, z) &= \mathcal{E}^h \sigma \int \mathcal{L}(t) \left[1 + A^h_{\|}(x, Q^2, z)\ P_T(t) P_B(t)\right] dt, \\ N^h_{\uparrow\Uparrow}(x, Q^2, z) &= \mathcal{E}^h \sigma \int \mathcal{L}(t) \left[1 - A^h_{\|}(x, Q^2, z)\ P_T(t) P_B(t)\right] dt, \end{aligned} \tag{4.9}$$

where $A^h_{\|}$ is the double-spin asymmetry of the process. σ is the integrated unpolarized DIS cross-section of Eq. 2.8, over the kinematical region of interest, and $\mathcal{E}^h$ is the acceptance and efficiency of this same region for event type h (assumed spin-independent). $\mathcal{L}(t)$ is the time-dependent luminosity, while $p_T(t)$ and $p_B(t)$ are the polarizations of the target and beam, respectively.

Note that h can denote any of the inclusive or semi-inclusive event types on either of the target types; in the inclusive case, the dependence is on x and Q^2 only, while in the semi-inclusive case there is additional z_h dependence. As the focus is on the x dependence of the asymmetries, Eq. 4.9 are integrated over Q^2 and z_h. The only time-dependent quantities in the integral are the luminosity and polarization terms. If the luminosity and polarization integrals are rewritten as

$$\begin{aligned} L &= \int \mathcal{L}(t)\, dt, \\ L_P &= \int \mathcal{L}(t)\, |P_T(t) P_B(t)|\, dt, \end{aligned} \tag{4.10}$$

then the raw asymmetry $A_{||}^h$ is obtained by combination of Eq. 4.9, arriving at:

$$A_{||}^h = \frac{N^{\uparrow\Downarrow} L^{\uparrow\Uparrow} - N^{\uparrow\Uparrow} L^{\uparrow\Downarrow}}{N^{\uparrow\Downarrow} L_P^{\uparrow\Uparrow} + N^{\uparrow\Uparrow} L^{\uparrow\Downarrow}} \tag{4.11}$$

Acceptance and efficiency factors cancel in the ratio.

$A_{||}$ can be related to the virtual photoabsorption asymmetry as in Eq. 2.19 and Eq. 2.24. If $\mathbf{g_2}$ is assumed zero, then

$$\begin{aligned} A_1^h = \frac{g_1^h}{F_1^h} &= \frac{1}{(1+\gamma\eta)} \frac{A_{||}^h}{D} \\ &= \frac{1}{(1+\gamma\eta)} \frac{N^{\uparrow\Downarrow} L^{\uparrow\Uparrow} - N^{\uparrow\Uparrow} L^{\uparrow\Downarrow}}{N^{\uparrow\Downarrow} L_P^{\uparrow\Uparrow} D^{\uparrow\Uparrow} + N^{\uparrow\Uparrow} L_P^{\uparrow\Downarrow} D^{\uparrow\Downarrow}}. \end{aligned} \tag{4.12}$$

In this analysis, the events are binned in x, and the averages of the kinematic factors D, γ, and η (defined in Section 2.2.2) in each bin are computed and used, along with the particle yields in each bin, to construct the asymmetries. The depolarization factor D may vary slightly between the spin states, and is averaged separately for each spin state. Table 4.7 defines the binning used in the analysis, and average values of x in the bins.

4.5 Corrections to the Asymmetries

The measure A_1^h asymmetries, if calculated as in Eq. 4.12, do not represent the 'true' asymmetries of Nature until a few small corrections are applied. These are listed and

bin	x range	$\langle x \rangle$
1	0.023–0.040	0.033
2	0.040–0.055	0.047
3	0.055–0.075	0.065
4	0.075–0.100	0.087
5	0.100–0.140	0.119
6	0.140–0.200	0.168
7	0.200–0.300	0.244
8	0.300–0.400	0.342
9	0.400–0.600	0.465

Table 4.7: x bin definitions and average values.

---

detailed here.

4.5.1 Background

In a collected event, there may be more than one positron that matches DIS selection criteria. In addition to the scattered positron, positrons from photoproduced e^+e^- pairs may pass the DIS cuts. This is the dominant background in the DIS sample. The photoproduced e^+e^- pairs also are responsible for the majority of detected electrons. The charge-symmetry of this background channel allows for the detected electron yield to be used as a background subtraction, the idea being that false DIS positrons are mirrored by the DIS electron sample. The data analysis treats positrons and electrons identically, but electrons are given a negative weight in the inclusive analysis. In the semi-inclusive analysis, hadrons coincident with detected DIS electrons are subtracted from the semi-inclusive yields. This background subtraction is small, and only appears at low x values, as shown in Figure 4.6.

Diffractive processes may also contribute to DIS background. In particular, ρ production and decay can generate pion background uncorrelated to the nucleon spin structure. Estimation of this contribution indicates that it is small enough to be ignored [10].

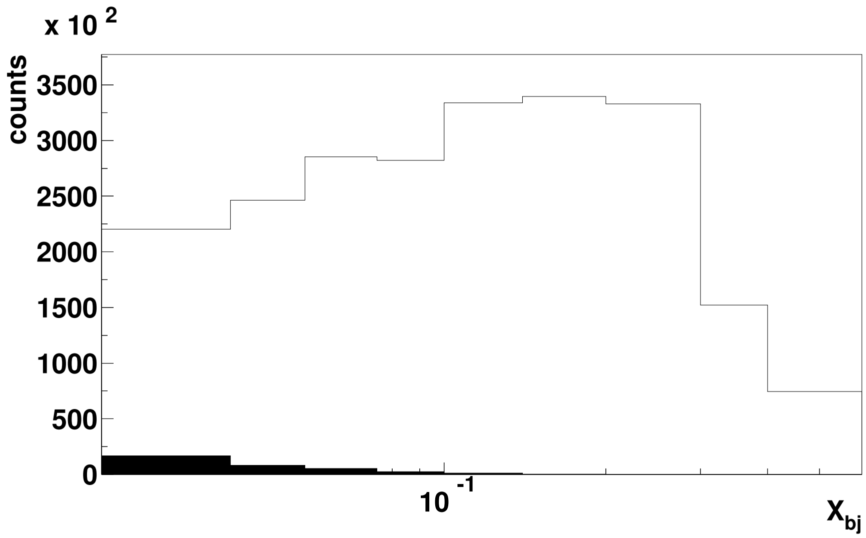

Figure 4.6: Deep Inelastic positron (white) and electron (black) yields for 1996 and 1997.

4.5.2 Smearing

The kinematic quantities measured by the HERMES spectrometer do not perfectly represent the true quantities. Systematic deviations must be estimated. At HERMES, measured kinematics differ from the true kinematics for two reasons. One, charged particles traversing the detector interact with the detector media and produce photons, altering the measured kinematics. Two, imperfections in detector alignment and track reconstruction can contribute small kinematic shifts. Both effects can be estimated by Monte Carlo [11]. DIS events are generated and physics asymmetries constructed. The same events are also passed through a realistic model of the HERMES detector and reconstructed with HRC. The ratio of the perfect Monte Carlo asymmetries to the realistic Monte Carlo asymmetries provides the smearing correction.

$$\begin{aligned} C_{\rm smear} &= \frac{A^h_{\rm MC,ideal}}{A^h_{\rm MC,realistic}} \\ A^h_{\rm corrected} &= C_{\rm smear} \cdot A^h_{\rm measured} \end{aligned} \tag{4.13}$$

While smearing corrections were calculated for all three years of data-taking, the 1995 smearing corrections on the ^{3}He asymmetries are small enough to be neglected [12, 13]. Proton corrections are listed in Table 4.8 for the inclusive asymmetries and the semi-inclusive charged hadron asymmetries. Charged pion asymmetries are assumed to have the same smearing corrections as charged hadron asymmetries. The proton corrections differ for 1996 and 1997 because of the different reconstruction methods used: "NOVC" in 1996, and "STD" in 1997.

	1996			1997		
$\langle x \rangle$	e^+	h^+	h^-	e^+	h^+	h^-
0.033	0.946±0.009	0.916±0.007	0.984±0.019	0.946±0.009	0.914±0.007	0.984±0.019
0.047	0.975±0.009	0.934±0.007	0.965±0.017	0.975±0.009	0.935±0.007	0.970±0.017
0.065	0.967±0.009	0.934±0.007	0.947±0.015	0.967±0.009	0.934±0.007	0.947±0.015
0.087	0.955±0.009	0.930±0.006	0.932±0.011	0.955±0.009	0.931±0.006	0.932±0.011
0.119	0.937±0.009	0.937±0.005	0.934±0.007	0.937±0.009	0.932±0.004	0.930±0.007
0.168	0.931±0.008	0.957±0.004	0.956±0.005	0.931±0.008	0.952±0.004	0.950±0.005
0.244	0.934±0.007	0.977±0.003	0.978±0.004	0.934±0.007	0.977±0.003	0.978±0.004
0.342	0.966±0.008	0.993±0.003	0.992±0.004	0.966±0.008	0.994±0.003	0.994±0.003
0.465	0.989±0.005	0.999±0.004	0.995±0.004	0.989±0.005	1.001±0.003	0.998±0.004

Table 4.8: Smearing corrections for 1996 and 1997 [14].

4.5.3 Radiative Corrections

The leading order single photon exchange (Born approximation) depicted in Figure 2.1 provides a good model for the DIS process. Higher order radiative processes, however, also contribute to the measured cross-section and must be corrected for in the asymmetries. The participating first-order QED processes are shown in Figure 4.7.

The radiative processes are modeled by programming the measured ^{1}H and ^{3}He asymmetries into the POLRAD [16, 12] code, which calculates the correction δ_{RC} needed to reproduce the Born cross-section.

$$\begin{aligned} \delta_{\mathrm{RC}} &= A^h_{\mathrm{Born}} - A^h_{\mathrm{total}} \\ A^h_{\mathrm{corrected}} &= A^h_{\mathrm{measured}} + \delta_{\mathrm{RC}} \end{aligned} \tag{4.14}$$

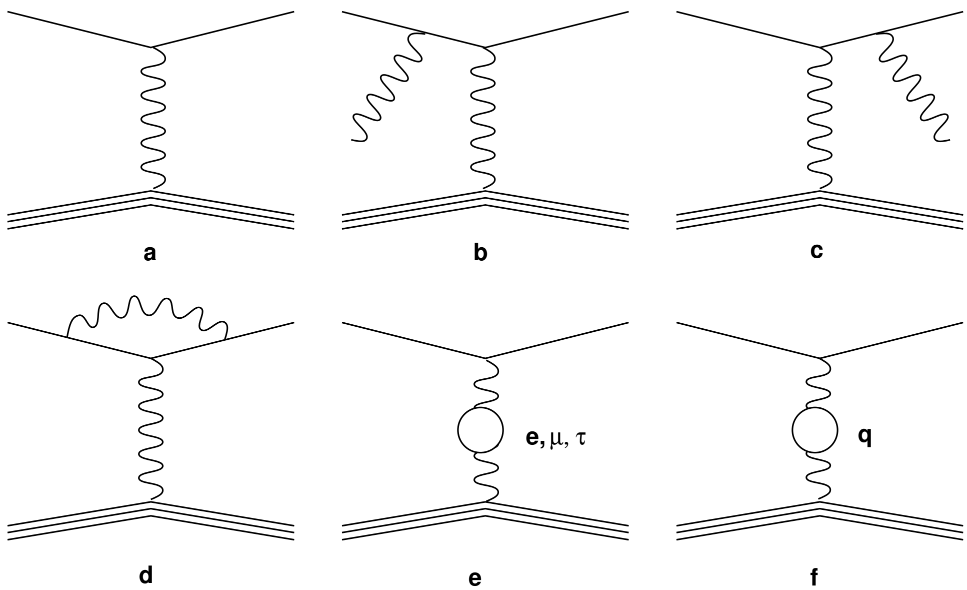

Figure 4.7: Feynman diagrams for processes contributing to the radiative corrections to DIS. a) The one photon exchange term. b) initial state brehmsstrahlung correction, c) final state brehmsstrahlung correction, d) vertex correction, e),f) vacuum polarization correction.

$\langle x \rangle$	^{3}He	^{1}H (1996)	^{1}H (1997)
0.033	$0.0571_{\pm 0.00292}$	$0.00121_{\pm 0.00006}$	$0.00121_{\pm 0.00006}$
0.047	$0.0494_{\pm 0.00134}$	$0.00119_{\pm 0.00004}$	$0.00119_{\pm 0.00004}$
0.065	$0.0474_{\pm 0.00064}$	$0.00117_{\pm 0.00003}$	$0.00117_{\pm 0.00003}$
0.087	$0.0439_{\pm 0.00023}$	$0.00097_{\pm 0.00004}$	$0.00097_{\pm 0.00004}$
0.119	$0.0423_{\pm 0.00062}$	$0.00049_{\pm 0.00003}$	$0.00049_{\pm 0.00003}$
0.168	$0.0404_{\pm 0.00100}$	$-0.00037_{\pm 0.00002}$	$-0.00037_{\pm 0.00002}$
0.244	$0.0389_{\pm 0.00138}$	$-0.00131_{\pm 0.00010}$	$-0.00123_{\pm 0.00010}$
0.342	$0.0399_{\pm 0.00181}$	$-0.00205_{\pm 0.00006}$	$-0.00201_{\pm 0.00006}$
0.465	$0.0384_{\pm 0.00196}$	$-0.00223_{\pm 0.00013}$	$-0.00210_{\pm 0.00013}$

Table 4.9: Radiative corrections for the inclusive asymmetries [12, 15].

Radiative corrections to the measured inclusive asymmetries are listed in Table 4.9. Semi-inclusive corrections have been calculated to be negligible [12].

4.6 Statistical Uncertainties of the Asymmetries

The statistical uncertainties of the A_1 asymmetries are straightforwardly calculated. As luminosities and polarizations at HERMES are determined with high statistical precision, only the Poisson distributed ($(\delta N)^2 = N$) counting rates contribute.

The statistical uncertainty δA_1 can then be calculated

$$(\delta A_1)^2 = \left(\frac{\partial A_1}{\partial N^{\uparrow\Downarrow}} \cdot \delta N^{\uparrow\Downarrow}\right)^2 + \left(\frac{\partial A_1}{\partial N^{\uparrow\Uparrow}} \cdot \delta N^{\uparrow\Uparrow}\right)^2; \tag{4.15}$$

starting with Eq. 4.12 yields

$$\delta A_1 = \frac{1}{(1+\gamma\eta)} \frac{L^{\uparrow\Downarrow} L_P^{\uparrow\Uparrow} D^{\uparrow\Uparrow} + L^{\uparrow\Uparrow} L_P^{\uparrow\Downarrow} D^{\uparrow\Downarrow}}{(N^{\uparrow\Downarrow} L_P^{\uparrow\Uparrow} D^{\uparrow\Uparrow} + N^{\uparrow\Uparrow} L_P^{\uparrow\Downarrow} D^{\uparrow\Downarrow})^2} \sqrt{N^{\uparrow\Downarrow}(N^{\uparrow\Uparrow})^2 + N^{\uparrow\Uparrow}(N^{\uparrow\Downarrow})^2}. \tag{4.16}$$

4.6.1 Correlations

The different asymmetries A_1^h measured at HERMES of the yields of the different particle types h are statistically correlated with each other. This impacts the further analysis of the asymmetries detailed in the next chapter and bears discussion. The semi-inclusive event samples are subsets of the inclusive sample, and therefore a statistically significant correlation between the semi-inclusive and inclusive asymmetries is expected. That the asymmetry correlations are proportional to the particle multiplicities, n_h, can be derived [17], yielding

$$\mathrm{Cor}(A_1^{h_i}, A_1^{h_j}) = \frac{\langle n^{h_i} n^{h_j} \rangle}{\sqrt{\langle (n^{h_i})^2 \rangle \langle (n^{h_j})^2 \rangle}}. \tag{4.17}$$

n^{e^+} is defined to be 1, and there is zero correlation between asymmetries from different years. Given these correlations, shown in Table 4.10, a statistical covariance matrix $\mathcal{C}_A^{\mathrm{stat}}$

	^{3}He			^{1}H		
$\langle x \rangle$	A^{e^+}, A^{h^+}	A^{e^+}, A^{h^-}	A^{h^+}, A^{h^-}	A^{e^+}, A^{h^+}	A^{e^+}, A^{h^-}	A^{h^+}, A^{h^-}
0.033	0.446	0.395	0.128	0.453	0.394	0.130
0.047	0.491	0.417	0.137	0.500	0.414	0.140
0.065	0.507	0.411	0.131	0.517	0.406	0.134
0.087	0.497	0.386	0.117	0.509	0.379	0.120
0.119	0.452	0.336	0.105	0.464	0.328	0.108
0.168	0.365	0.260	0.096	0.375	0.253	0.098
0.244	0.260	0.178	0.083	0.267	0.171	0.084
0.342	0.183	0.120	0.066	0.188	0.115	0.066
0.465	0.127	0.080	0.051	0.130	0.076	0.050

Table 4.10: Correlations between inclusive and semi-inclusive hadron asymmetries.

---

can be constructed, relating all the asymmetries:

$$\mathcal{C}_A^{\mathrm{stat},ij} \;=\; \mathrm{Cor}(A_1^{h_i}, A_1^{h_j}) \cdot \delta A_1^{h_i} \delta A_1^{h_j}. \tag{4.18}$$

The full matrix $\mathcal{C}_A^{\mathrm{stat},ij}$ is used in one of the analyses in the next chapter. Each year is treated separately in that analysis, as experimental conditions varied from year to year. The resultant matrix for analysis of the inclusive and charged hadron ($h^{\pm}$) asymmetries is then 9×9. Also note that the statistical variance of an included asymmetry $A_1^{h_i}$ is given by the square root of the ith diagonal element,

$$\delta A_1^{h_i} \;=\; \sqrt{\mathcal{C}_A^{\mathrm{stat},ii}} \tag{4.19}$$

4.7 Systematic Uncertainties of the Asymmetries

There are both experimental and theoretical issues that contribute uncertainties to the asymmetries that are not statistical in their nature. Just as the statistical covariance matrix of Eq. 4.18 was introduced, it is useful now to discuss these systematic uncertainties along with the correlations of the uncertainties among the measured asymmetries, defining in the process a systematic covariance matrix $\mathcal{C}_A^{\mathrm{sys}}$.

4.7.1 Beam Polarization

The scale of the asymmetries is determined by the polarization measurements. The beam polarization was measured with the same apparatus for all three years of data-taking, so there are correlations in this uncertainty among all measured asymmetries. The main contribution to the uncertainty is given by a calibration constant which was determined only once for all data-taking (hence, 100% correlated among all HERMES measurements), to a relative precision of $\Delta P/P = 3.26\%$. Instabilities in the measurements from year to year lead to estimated fractional uncertainties of $\Delta P_{\rm year}/P_{\rm year} = (2.2\%, 0.9\%, 0.9\%)$ for the years 95, 96, and 97, respectively. These contributions to the uncertainties are 100% correlated within a year, but completely uncorrelated otherwise. The beam polarization covariances are then

$$\mathcal{C}_A^{P_B,\mathrm{ij}} = A_1^{h_\mathrm{i}} A_1^{h_\mathrm{j}} \left[\left(\frac{\Delta P}{P}\right)^2 + \delta_{\mathrm{year_i},\mathrm{year_j}} \left(\frac{\Delta P_{\rm year}}{P_{\rm year}}\right)^2 \right]. \qquad (4.20)$$

4.7.2 Target Polarization

The target polarization measurement further determines the scale of the asymmetries. In 1995, the ^{3}He target polarization had a relative uncertainty of 5%, so for all 1995 ^{3}He asymmetries,

$$\mathcal{C}_{A_{^3\mathrm{He}}}^{P_T,\mathrm{ij}} = A_1^{h_\mathrm{i}} A_1^{h_\mathrm{j}} \left(\frac{\Delta P_{^3\mathrm{He}}}{P_{^3\mathrm{He}}}\right)^2. \qquad (4.21)$$

Treatment of the ABS data is not as straightforward. In 1997, the relative uncertainty in the target polarization was determined to 4.5%. In 1996, however, the target's commissioning year, the target was not well understood. Molecular recombination inside the target cell was much larger in this year, leading to the polarization's relative uncertainty being estimated at over 12%.

A different method of determining the 1996 target polarization uncertainty was needed in order to use the data in a precision analysis. The inclusive $A_{||}$ for both 1996 and 1997 were formed, using the best target polarization calculations available for each year. As both measurements are of the same physics, the resulting asymmetries should be statistically identical. The 1996 target polarization was then determined by renormalizing the 1996 inclusive asymmetry to the 1997 asymmetry. The statistical error of the fitting constant yielded a polarization uncertainty of 4%. This uncertainty is correlated among all 1996 measurements, while the 4.5% 1997 uncertainty is correlated among all measurements from both 1996 and 1997:

$$\mathcal{C}_{A_{1\,\mathrm{H}}}^{P_T,\mathrm{ij}} = A_1^{h_\mathrm{i}} A_1^{h_\mathrm{j}} \left(\left(\frac{\Delta P_{1997}}{P_{1997}} \right)^2 + \delta_{96} \left(\frac{\Delta P_{1996}}{P_{1996}} \right)^2 \right). \tag{4.22}$$

4.7.3 Yield Fluctuations

The normalized yield of positrons during data-taking should be constant modulo the acceptance and efficiency. Instabilities in detector efficiencies can give the yields a time-dependence. If the time-dependence varies on the scale of the target spin-flip time, then the asymmetries can be affected.

The test of instability of this sort is to replace the target spin orientation values with random ones. New asymmetries are calculated. These random spin asymmetries should average to zero, and their variance should match the statistical uncertainty of the physics asymmetry. A difference in the spread of the random asymmetry distribution from the expected signals the presence of additional systematic effects.

The 1996 and 1997 inclusive and semi-inclusive asymmetries pass this test [18]. Asymmetries from 1995 data, however, show inclusive and semi-inclusive variances that are larger than expected [12, 19]. The longer time scale for target spin-flips in 1995 makes it likely that yield fluctuations could appear on the spin-flip time scale, causing this extra uncertainty. The difference between the measured and expected variances are used as another source of systematic uncertainty on the ^{3}He asymmetries;

$$(\sigma_{\mathrm{yield}}^{h_\mathrm{i}})^2 = (\sigma_{\mathrm{measured}}^{h_\mathrm{i}})^2 - (\sigma_{\mathrm{expected}}^{h_\mathrm{i}})^2. \tag{4.23}$$

It is assumed that the calculated uncertainty can be applied to every x bin. Each ^{3}He asymmetry x bin's covariance matrix then becomes

$$\mathcal{C}_{A_{3\,\mathrm{He}}}^{\mathrm{yield,ij}} = \sigma_{\mathrm{yield}}^{\mathrm{i}} \sigma_{\mathrm{yield}}^{\mathrm{j}} \tag{4.24}$$

4.7.4 Smearing and Radiative Corrections

Systematic uncertainties in the smearing and radiative corrections described in Sections 4.5.2 and 4.5.3 were estimated during their calculation. Smearing contributions are assumed to be correlated among all asymmetries measured in the same year, and are applied only to ^{1}H asymmetries. The radiative corrections were only applied to the inclusive asymmetries and so the systematic uncertainties are only applied to them.

$$\mathcal{C}_A^{\mathrm{smear/rad,ij}} = A^{h_\mathrm{i}} A^{h_\mathrm{j}} \left(\frac{\Delta C_{\mathrm{smear}}}{C_{\mathrm{smear}}}\right)^2 + \delta_{\mathrm{incl.}}(\Delta(\delta_{\mathrm{RC}}))^2. \tag{4.25}$$

4.7.5 Uncertainty in R

An additional contribution to the systematic error is given by the uncertainty of the ratio of longitudinal to transverse cross-sections $R(x, Q^2)$, which can be treated as a correlated systematic uncertainty on the measured asymmetries.

$$\mathcal{C}_A^{R,\mathrm{ij}} = A^{h_\mathrm{i}} A^{h_\mathrm{j}} (\Delta R)^2 \tag{4.26}$$

4.8 The Asymmetries

Finally, the asymmetries extracted from the HERMES 1995, 1996, and 1997 data-taking are presented in this Section. As the 1996 and 1997 asymmetries are of the same physics, they are presented first separately to show their statistical compatibility, and then combined, to form the final HERMES measurement of A_1^p.

The total systematic uncertainty for each asymmetry is formed from the square root of the corresponding diagonal element of the matrix

$$\mathcal{C}_A^{\mathrm{Sys.}} = \mathcal{C}_A^{\mathrm{P_B}} + \mathcal{C}_A^{\mathrm{P_T}} + \mathcal{C}_A^{\mathrm{yield}} + \mathcal{C}_A^{\mathrm{smear/rad}} + \mathcal{C}_A^{R}. \tag{4.27}$$

The statistical compatibility of the 1996 and 1997 asymmetries (Figure 4.8) allow them to be statistically averaged, and final ^{3}He and ^{1}H asymmetries can be presented. Figure 4.9 compares the inclusive asymmetries to the best measurements from SLAC [20, 21], which have high statistical precision and are over a kinematical range similar to HERMES. The

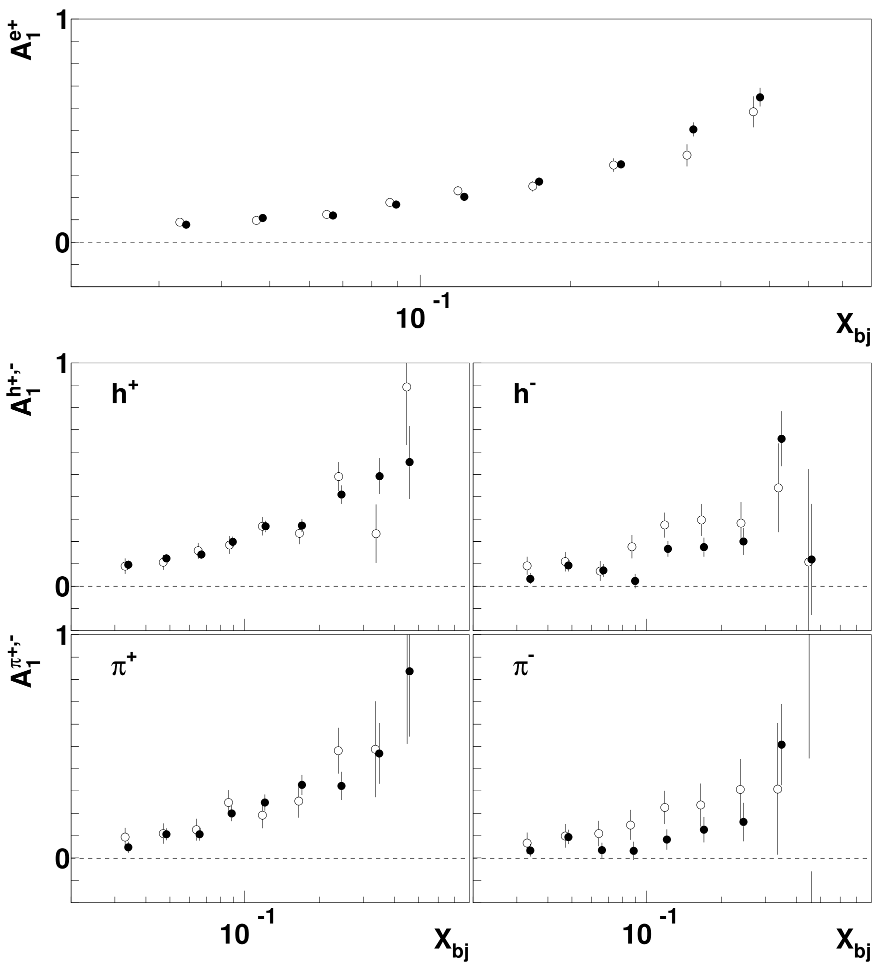

Figure 4.8: 1996 (open circles) and 1997 (closed circles) inclusive and semi-inclusive asymmetries on the ^{1}H target. Only statistical uncertainties shown.

---

measurements are consistent.

Semi-inclusive DIS hadron asymmetries at HERMES are compared to those measured at CERN by SMC [22] in Figure 4.11. The measurements are consistent, though HERMES has the better precision in its kinematic range.

The ability of HERMES to identify pions in the semi-inclusive channel is unique among DIS experiments. Total hadron asymmetries on ^{3}He and identified pion asymmetries on both ^{3}He and ^{1}H are measured for the first time at HERMES, and shown in Figures 4.10 and 4.11.

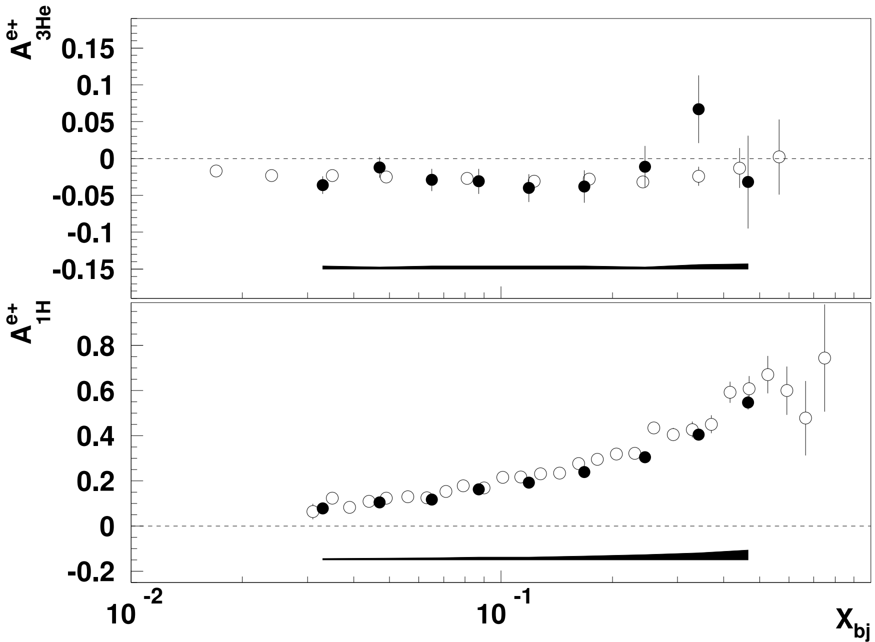

Figure 4.9: Final inclusive DIS A_1 asymmetries on ^{3}He and ^{1}H. The HERMES measurements (closed circles) are compared to measurements from SLAC (open circles) [20, 21]. Statistical error bars are shown; systematic errors for HERMES are shown in the dark bands.

While the double-spin DIS asymmetries presented here are the basic experimental results of HERMES, they alone do not give detailed information about the structure of the nucleon. The next chapter will use these asymmetries in order to separate the quark polarizations in the nucleon by flavor.

References

[1] CERN-CN Division, CERN, EPIO — Experimental Physics Input Output Package, 1993.

[2] ECP Division, CERN, ADAMO — Entity-relationship programming system, version 3.3, 1994.

[3] W. Wander, Proceedings of CHEP '95, Rio de Janeiro, 1995.

[4] W. Wander, Ph.D. thesis, University of Erlangen-Nürnberg, Germany, 1996.

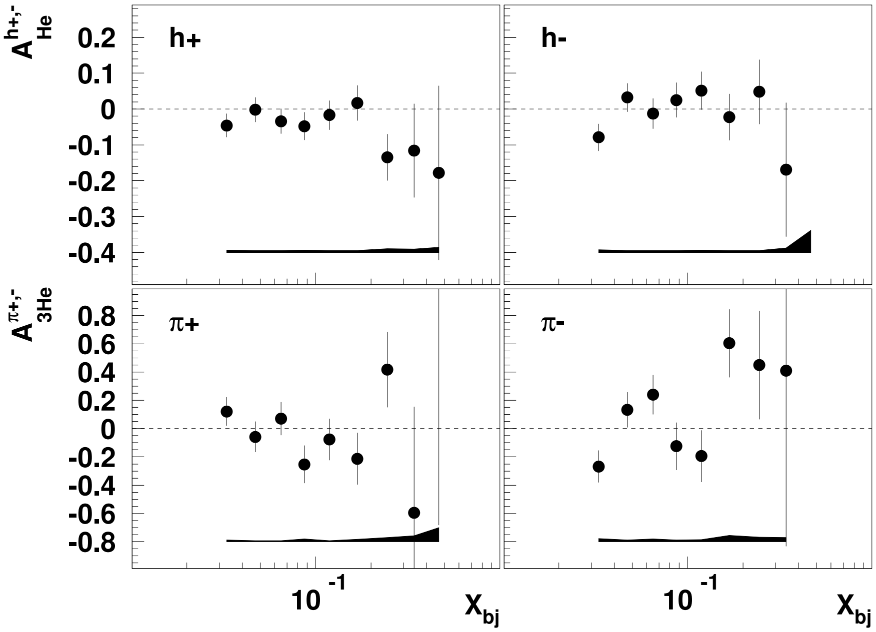

Figure 4.10: Final semi-inclusive DIS ^{3}He A_1 asymmetries. Statistical error bars are shown; systematic error is shown in the dark band.

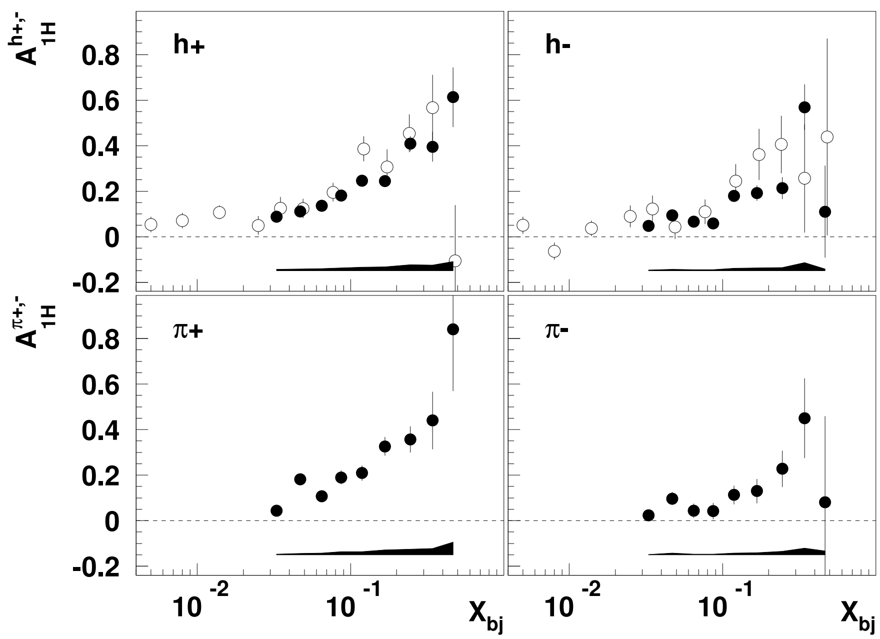

Figure 4.11: Final semi-inclusive DIS ^{1}H A_1 asymmetries, compared to SMC (open circles) [22]. Statistical error bars for both experiments are shown; systematic error for HERMES is shown in the dark band.

[5] M. Kolstein, Ph.D. thesis, Free University, Amsterdam, 1998.

[6] HERMES Collaboration, Phys. Lett. B **404**, 383 (1997).

[7] HERMES Collaboration, Phys. Lett. B **442**, 484 (1998).

[8] HERMES Collaboration, Phys. Lett. B **464**, 123 (1999).

[9] R. Kaiser, Ph.D. thesis, Simon Fraser University, 1997.

[10] J. Ouyang, 1997, HERMES Internal Note 97–047.

[11] A. Gute, Ph.D. thesis, University of Erlangen-Nürnberg, Germany, 1999.

[12] The HERMES g_1^n Group, 1997, HERMES Internal Note 97–007.

[13] M. Ferstl, Ph.D. thesis, University of Erlangen-Nürnberg, Germany, 1997.

[14] A. Gute, private communication.

[15] I. Akushevich, private communication.

[16] I. Akushevich and N. Shumeiko, J. Phys. G: Nucl. Part. Phys. **20**, 513 (1994).

[17] M.A. Funk, Ph.D. thesis, University of Hamburg, Germany, 1998.

[18] B. Bains *et al.*, 1999, HERMES Internal Note 99–015.

[19] H. Tallini, Ph.D. thesis, University of Liverpool, 1998.

[20] E154 Collaboration, Phys. Rev. Lett. **79**, 26 (1997).

[21] E143 Collaboration, Phys. Rev. D **58**, 112003 (1998).

[22] Spin Muon Collaboration, Phys. Lett. B **420**, 180 (1998).

5

Extraction of Parton Distribution Functions

The double-spin asymmetries, whose extraction was described in the previous chapter, are the basic experimental results of HERMES. The asymmetries represent combinations of the different quark flavors' contributions to the spin of the nucleon. Two alternate methods of the nucleon's spin separation by quark flavor are presented. The first utilizes a new asymmetry — pion charge difference — measured on each target. The second uses the inclusive and charged hadron asymmetries on each target as presented in the previous chapter.

5.1 Pion Charge Difference Method

The ability of the HERMES spectrometer to uniquely identify pions allows the use of a new technique in separating the nucleon's spin content by quark flavor.

5.1.1 The Asymmetries

Asymmetries of the pion charge difference can be formed. From Eq. 2.28 and Eq. 2.29 in Section 2.3.1, charged pion yields on a ^{1}H target can be written

$$\begin{aligned} N^{\pi^+} &\propto (4u(x)+\bar{d}(x))D^+ + (d(x)+4\bar{u}(x))D^- + (s(x)+\bar{s}(x))D^s \\ N^{\pi^-} &\propto (4u(x)+\bar{d}(x))D^- + (d(x)+4\bar{u}(x))D^+ + (s(x)+\bar{s}(x))D^s, \end{aligned} \tag{5.1}$$

where both expressions have the same proportionality constant. The yield of pion charge excess can then be written

$$\begin{aligned} N^{\pi^+-\pi^-} &= N^{\pi^+} - N^{\pi^-} \\ &\propto (4u(x) - 4\bar{u}(x) - d(x) + \bar{d}(x))(D^+ - D^-), \end{aligned} \tag{5.2}$$

or

$$N^{\pi^+-\pi^-} \propto (4u_v(x) - d_v(x))(D^+ - D^-), \tag{5.3}$$

where $u_v(d_v) \equiv u(d) - \bar{u}(\bar{d})$ are defined to be the valence u and d quark distributions. This expression for the pion charge difference yield can be used in the construction of the double-spin pion charge difference asymmetry,

$$A^{\pi} = \frac{N_{\uparrow\Downarrow}^{\pi^+-\pi^-} - N_{\uparrow\Uparrow}^{\pi^+-\pi^-}}{N_{\uparrow\Downarrow}^{\pi^+-\pi^-} + N_{\uparrow\Uparrow}^{\pi^+-\pi^-}}. \tag{5.4}$$

For the ^{1}H target, using Eq. 5.3,

$$A^{\pi}_{^1\mathrm{H}} = \frac{4\Delta u_v(x) - \Delta d_v(x)}{4u_v(x) - d_v(x)}. \tag{5.5}$$

Similarly, for the ^{3}He target,

$$A^{\pi}_{^3\mathrm{He}} = \frac{-\Delta u_v(x) + 4\Delta d_v(x)}{7u_v(x) + 2d_v(x)}. \tag{5.6}$$

The double-spin pion charge differency asymmetries on ^{1}H and ^{3}He are shown in Figure 5.1.

5.1.2 The Results

Note that in going from Eq. 5.1 to Eq. 5.2 and 5.3, the terms involving the s quarks cancel, due to the assumed equality of the likelihoods of a struck s quark fragmenting into either a π^+ or π^-. Also note that the remaining $(D^+ - D^-)$-dependence in the pion charge difference yields (Eq. 5.3) cancels in the asymmetry ratio. The cancellation of the fragmentation functions is due to the factorization assumption discussed in Section 2.3.1.

From these two asymmetries, $\Delta u_v(x)$ and $\Delta d_v(x)$ can be solved for in a straightforward

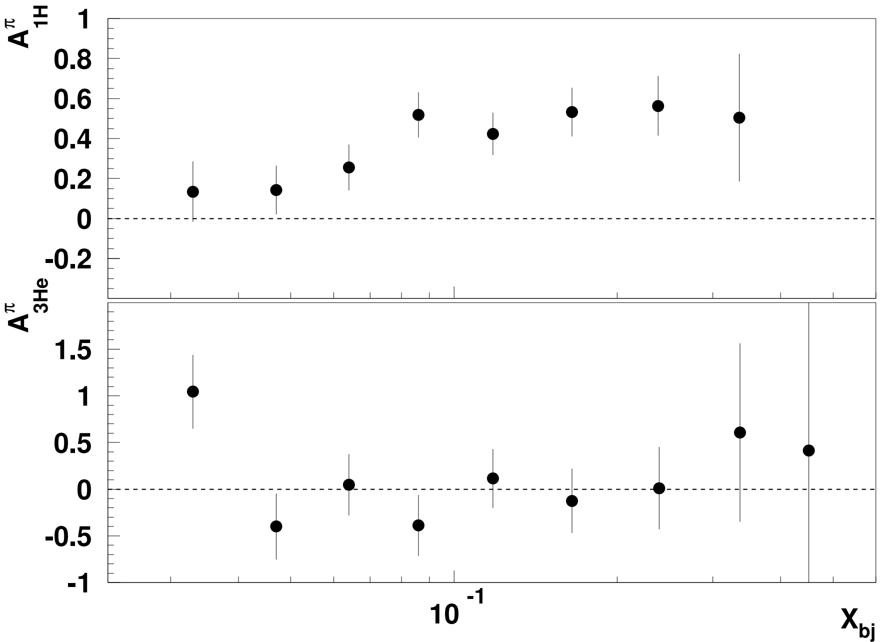

Figure 5.1: Final DIS pion charge difference asymmetries on ^{1}H and ^{3}He. Only statistical error bars are shown.

---

manner, arriving at the expressions

$$\begin{aligned}
\Delta u_v(x) &= \frac{1}{15}[4(4u_v(x) - d_v(x))A^{\pi}_{^1\mathrm{H}} + (7u_v(x) + 2d_v(x))A^{\pi}_{^3\mathrm{He}}] \\
\Delta d_v(x) &= \frac{1}{15}[(4u_v(x) - d_v(x))A^{\pi}_{^1\mathrm{H}} + 4(7u_v(x) + 2d_v(x))A^{\pi}_{^3\mathrm{He}}]. \qquad (5.7)
\end{aligned}$$

The method is attractive for its lack of dependence on Monte Carlo, and the few required assumptions.

The relatively low charged pion yields (as compared to inclusive yields and generic charged hadron yields), in addition to the fact that the difference in the positive and negative pion yields is taken, leads to a large statistical uncertainty in the resultant $\Delta u_v(x)$ and $\Delta d_v(x)$ measurements. Results are shown in Figure 5.2.

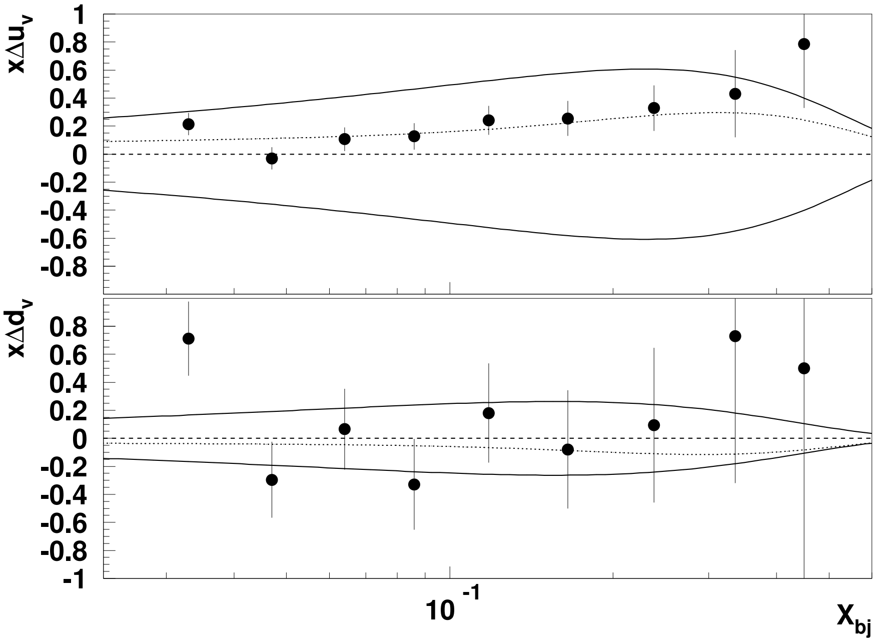

Figure 5.2: x-weighted Δu_v and Δd_v distributions, extracted from the pion charge difference asymmetries. Solid lines show the upper and lower bounds, $[q_v, -q_v]$, while the dotted lines show Δq_v parametrizations from Ref. [1]. Only statistical error bars are shown.

5.1.3 Monte Carlo Check

To check the validity of the extraction method, the technique was used on Monte Carlo generated events. Events were generated given the same underlying assumptions assumed in the extraction of Section 5.1.2, namely, isospin symmetry of the fragmentation functions, and the fact that the fragmentation process factorizes from the scattering process. By using the Monte Carlo to generate events using these assumptions, asymmetries can be formed and used to recover the polarized valence quark distributions that are also inputs to the Monte Carlo.

That isospin symmetry is found in the Monte Carlo fragmentation functions (reduction of fragmentation functions from 12 to 3, explained in Section 2.3.1) is shown in Figure 5.3. The factorization assumption — lack of x-dependence in the fragmentation functions — is verified in the Monte Carlo and shown for $D_u^{\pi^+}$ in Figure 5.4. As the assumptions regarding isospin symmetry and factorization of the fragmentation functions are sufficiently met in

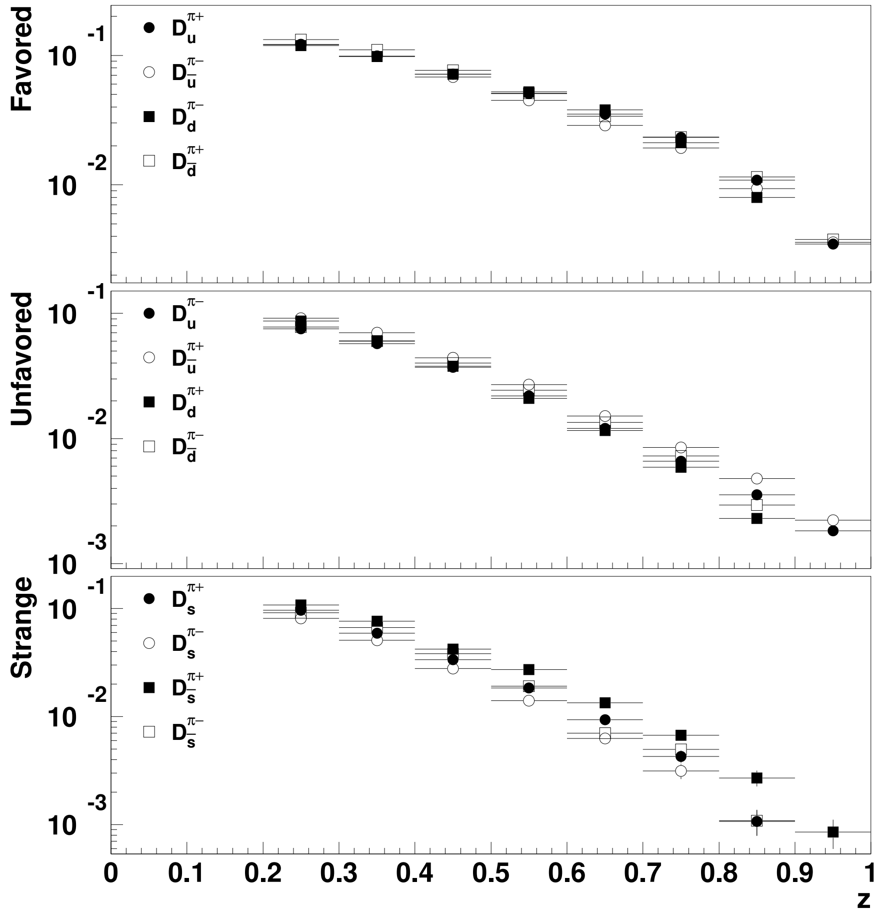

Figure 5.3: Isospin symmetry of the Monte Carlo generated charged pion fragmentation functions.

---

the Monte Carlo, events are generated and pion charge difference asymmetries are formed on both proton and neutron targets. The linear combination of these asymmetries that results in Δu_v and Δd_v is calculated, and the results are shown in Figure 5.5. Clearly, the input polarized valence quark distributions are not recovered. This has been independently verified via Monte Carlo study in a separate analysis [2].

5.1.4 Conclusion

While the method of using the charged pion difference asymmetries on ^{1}H and ^{3}He to extract the polarized valence quark distributions in the nucleon is a clean (Monte Carlo free) and

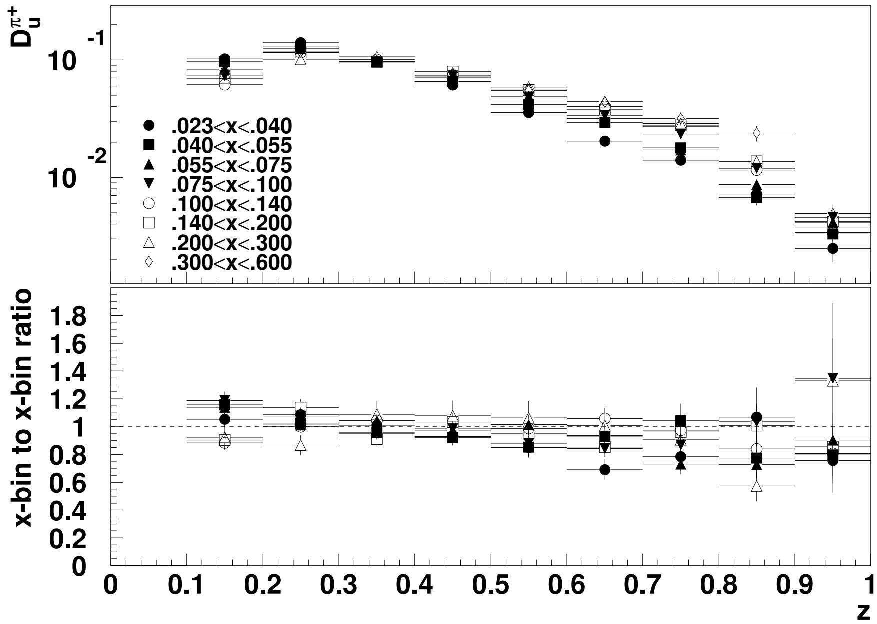

Figure 5.4: x independence of $D_u^{\pi^+}$. The upper plot shows $D_u^{\pi^+}$ for each x-bin, while the lower shows the ratios of those bin-separated functions.

---

straightforward approach, it does not give satisfactory results for HERMES. Monte Carlo checks of the technique, as described in Section 5.1.3, show that for HERMES kinematics and acceptance, $\Delta u_v(x)$ and $\Delta d_v(x)$ are not recovered.

The reason most likely involves the fragmentation process. The assumed isospin symmetry and factorization properties of the fragmentation functions are grossly met, as shown in Figures 5.3 and 5.4. The pion production, however, may not be sensitive to precisely the combination of quark distributions expected, perhaps because of acceptance issues. While this could certainly bear further study, the fact that the pion charge difference asymmetries are subject to low statistics due to taking the difference of the already low identified pion yields (especially in 1995), the analysis technique is dropped in favor of an alternative.

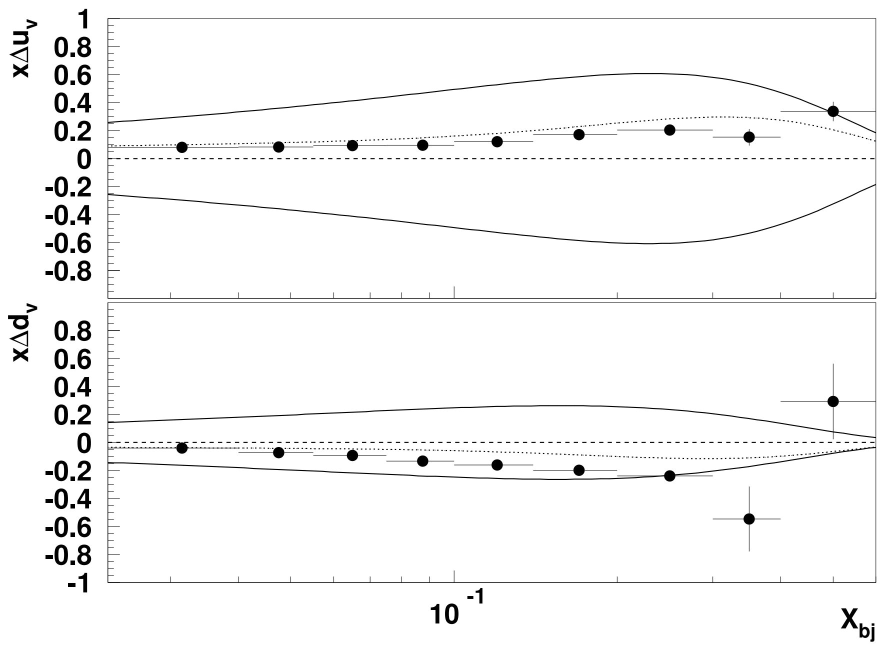

Figure 5.5: x-weighted Δu_v and Δd_v distributions, extracted from Monte Carlo-generated pion charge difference asymmetries. Solid lines show the upper and lower bounds, $[q_v, -q_v]$, while the dotted lines show the input Δq_v parametrizations. The input distributions were not recovered.

5.2 Purity Method

5.2.1 Overview

The purity formalism, as defined in Section 2.3.4, allows a convenient analysis for extraction of polarized parton densities. To repeat the earlier section, the measured asymmetries can be written as

$$A^h(x,z) \;=\; (1+R)\sum_q P_q^h(x,z)\frac{\Delta q(x)}{q(x)}, \tag{5.8}$$

with the purities defined as

$$P_q^h(x,z) \;=\; \frac{e_q^2 D_q^h(z) q(x)}{\sum_{q'} e_{q'}^2 D_{q'}^h(z) q'(x)}. \tag{5.9}$$

The purities can be interpreted as the probability that a detected particle h originated in the scattering of the beam lepton from quark flavor q in the nucleon. This form of the asymmetries allows their use in a simple fit to the polarized parton densities. Given the purities, the measured asymmetries can be assembled together as a system of equations linear in the unknown $\frac{\Delta q(x)}{q(x)}$ functions, as in Eq. 5.8. These equations can be recast in matrix form, where for each x-bin,

$$\vec{\mathbf{A}} = \mathbf{P}\vec{\mathbf{Q}}, \tag{5.10}$$

having defined column vectors of n_A asymmetries, n_q quark polarizations, and the $n_A \times n_q$ rectangular purity matrix:

$$\vec{\mathbf{A}}(x) = \begin{pmatrix} A^{h_1}(x) \\ \vdots \\ A^{h_{n_A}}(x) \end{pmatrix}, \quad \vec{\mathbf{Q}}(x) = \begin{pmatrix} \frac{\Delta q_1(x)}{q_1(x)} \\ \vdots \\ \frac{\Delta q_{n_q}(x)}{q_{n_q}(x)} \end{pmatrix}, \quad \mathbf{P}(x) = \begin{bmatrix} P_{q_1}^{h_1}(x) & \cdots & P_{q_{n_q}}^{h_1} \\ \vdots & \ddots & \vdots \\ P_{q_1}^{h_{n_A}}(x) & \cdots & P_{q_{n_q}}^{h_{n_A}} \end{bmatrix}. \tag{5.11}$$

The number of measured asymmetries n_A is typically larger than the number of independent quark polarizations n_q, so the system is overconstrained. The solution vector $\vec{\mathbf{Q}}$ to the matrix equation is the one which minimizes [3, 4]

$$\chi^2 = \left(\vec{\mathbf{A}} - \mathbf{P}\cdot\vec{\mathbf{Q}}\right)^T \mathcal{C}_A^{-1} \left(\vec{\mathbf{A}} - \mathbf{P}\cdot\vec{\mathbf{Q}}\right), \tag{5.12}$$

where $\mathcal{C}_A$ is the asymmetry covariance matrix introduced in Section 4.6.1. The quark polarization covariance $\mathcal{C}_Q$ is given by

$$\mathcal{C}_Q = \left(\mathbf{P}^T \, \mathcal{C}_A^{-1} \, \mathbf{P}\right)^{-1}, \tag{5.13}$$

and the solution to the purity equation is then

$$\vec{\mathbf{Q}} = \mathcal{C}_Q^{-1} \, \mathbf{P}^T \, \mathcal{C}_A^{-1} \, \vec{\mathbf{A}}. \tag{5.14}$$

5.2.2 Treatment of ^{3}He Data

Parton distributions are defined on the proton, and Monte Carlo techniques allow straightforward calculation of proton purities, as detailed in the next Section. Neutron purities can be derived from proton purities by simple isospin rotation: $u \leftrightarrow d$ and $\bar{u} \leftrightarrow \bar{d}$ in the Monte

Carlo inputs. The ^{3}He target used at HERMES for the asymmetries used in this analysis is treated as a proton and neutron mixture. A nuclear correction is required to relate the asymmetries on the ^{3}He target to proton and neutron purities and quark polarizations.

Central to the nuclear correction is the assumption that nuclear structure functions are simple combinations of proton and neutron structure functions. For ^{3}He, with two protons and one neutron,

$$\begin{aligned} F_1^{^3\mathrm{He},h}(x) &= 2F_1^{p,h}(x) + F_1^{n,h}(x) \\ g_1^{^3\mathrm{He},h}(x) &= 2p^p_{^3\mathrm{He}} g_1^{p,h}(x) + p^n_{^3\mathrm{He}} g_1^{n,h}(x), \end{aligned} \tag{5.15}$$

where $p^{p/n}_{^3\mathrm{He}}$ are the effective polarizations of the protons/neutrons in the ^{3}He nucleus. $p^p_{^3\mathrm{He}}$ and $p^n_{^3\mathrm{He}}$ have been determined to be -0.027 and 0.865, respectively [5, 6].

For each asymmetry of particle type h measured on the ^{3}He target, the corresponding asymmetry has been measured on the proton. Manipulation of Eq. 5.15 then allows the separation of the neutron contribution to the ^{3}He asymmetries:

$$A_1^{n,h} = \frac{g_1^{n,h}}{F_1^{n,h}}(x) = \frac{1}{p^n_{^3\mathrm{He}}(1-f_p^h)}\left(A_1^{^3\mathrm{He},h} - p^p_{^3\mathrm{He}} f_p^h A_1^{p,h}\right), \tag{5.16}$$

where the dilution factor, f_p^h, is defined as the ratio of yields of h on the proton and on the nucleus.

$$f_p^h = \frac{2\sigma_p^h}{\sigma^h_{^3\mathrm{He}}} = \frac{2F_1^{p,h}}{F_1^{^3\mathrm{He},h}} \tag{5.17}$$

$$= \frac{n_h^p}{n_h^{^3\mathrm{He}}}\frac{2F_1^p}{F_1^{^3\mathrm{He}}} \tag{5.18}$$

Eq. 5.18 is derived by replacing the semi-inclusive structure functions by the inclusive ones times the DIS-normalized hadron multiplicities. This allows a direct measurement of the semi-inclusive dilution factor from HERMES unpolarized data, avoiding acceptance and normalization issues.

Eq. 5.16, then, gives a recipe for converting measured ^{3}He inclusive and semi-inclusive asymmetries into neutron asymmetries. To use this in the analysis, proton and neutron purities must be generated by Monte Carlo and the proton and ^{3}He asymmetries separated in the matrix purity equation. A new matrix $\mathcal{N}$ exists such that

$$\begin{pmatrix} \vec{\mathbf{A}}^p \\ \vec{\mathbf{A}}^{^3\mathrm{He}} \end{pmatrix} = \mathcal{N} \cdot \begin{pmatrix} \mathbf{P}^p \\ \mathbf{P}^n \end{pmatrix} \vec{\mathbf{Q}}. \tag{5.19}$$

If the proton and ^{3}He asymmetry vectors $\vec{\mathbf{A}}^p$ and $\vec{\mathbf{A}}^{^3\mathrm{He}}$ are arranged such that the asymmetry types h are in the same order, then from Eq. 5.16,

$$\mathcal{N} = \begin{pmatrix} 1 & & & & & \\ & \ddots & & & 0 & \\ & & 1 & & & \\ a_{h_1} & & & b_{h_1} & & \\ & \ddots & & & \ddots & \\ & & a_{h_m} & & & b_{h_m} \end{pmatrix}, \tag{5.20}$$

with

$$\begin{aligned} a_h &\equiv f_p^h p_{^3\mathrm{He}}^p \\ b_h &\equiv (1 - f_p^h) p_{^3\mathrm{He}}^n. \end{aligned} \tag{5.21}$$

The introduction of this dilution matrix allows the convenience of using neutron purities in the analysis. A more detailed review can be found in Reference [3].

5.2.3 Purity Generation

The next step is the generation of the purities. Three different processes are involved. First, the unpolarized parton distributions $q(x)$ reflect the probability of scattering from quark flavor q at the detected x. Second, the fragmentation functions $D_q^h(z)$ describe the probability that a hadron h is produced in the hadronization of the struck quark q in the nucleon. Third, an acceptance function which models the probability that the hadron h is detected in the HERMES spectrometer is used. Current levels of understanding of these three points are combined into the PEPSI Monte Carlo software package [7] , which is a polarized extension of the LEPTO [8] deep-inelastic scattering Monte Carlo. PEPSI is used to generate the purities.

In the PEPSI Monte Carlo, simulating HERMES data requires three steps. First, a point in the DIS kinematical plane is selected, defining the inclusive event information. The unpolarized quark distributions are used probabilistically to decide which quark flavor was struck in the scattering process. Secondly, the kinematics of the struck quark as well as the structure of the target remnant are passed to the hadronization code, which generates the semi-inclusive event information. The physics of the event simulation done, and the kinematics of all particles known, the Monte Carlo merely has to determine which of these particles would be seen and reconstructed as tracks by the detector.

Unpolarized Parton Distributions

It would be desirable to measure all unpolarized input in the same kinematic region and with the same apparatus as used for the measurement of the polarized hadron asymmetries of Chapter 4, as this would minimize systematic effects, and provide optimal tuning of quark densities and fragmentation parameters. However, global fits to world data and subsequent evolution of those fits to the HERMES kinematic range yield an accuracy for the unpolarized quark distributions that the HERMES unpolarized data cannot match. World parametrizations have been checked at HERMES directly with $\frac{F_2^n}{F_2^p}$ and $\bar{u}-\bar{d}$ measurements [9, 10]. In this analysis, a parametrization from the CTEQ Collaboration [11] is the primary one used, while one from the GRV [12] group is used to help determine systematic error. Both parametrizations are shown in Figure 5.6.

Fragmentation

Just as for the unpolarized quark distributions, it would be optimal to use fragmentation information directly measured at HERMES. By comparing inclusive and semi-inclusive yields on unpolarized targets, HERMES has extracted the fragmentation functions in its kinematic region. The favored and unfavored pion fragmentation functions extracted from 1996 data is shown in Figure 5.7 [13]. The measured HERMES fragmentation functions can be integrated over z, and in conjunction with unpolarized quark distributions, can be used to directly evaluate the purities in Eq. 5.9. The SMC experiment uses this approach in the extraction of polarized parton distributions from their data [15].

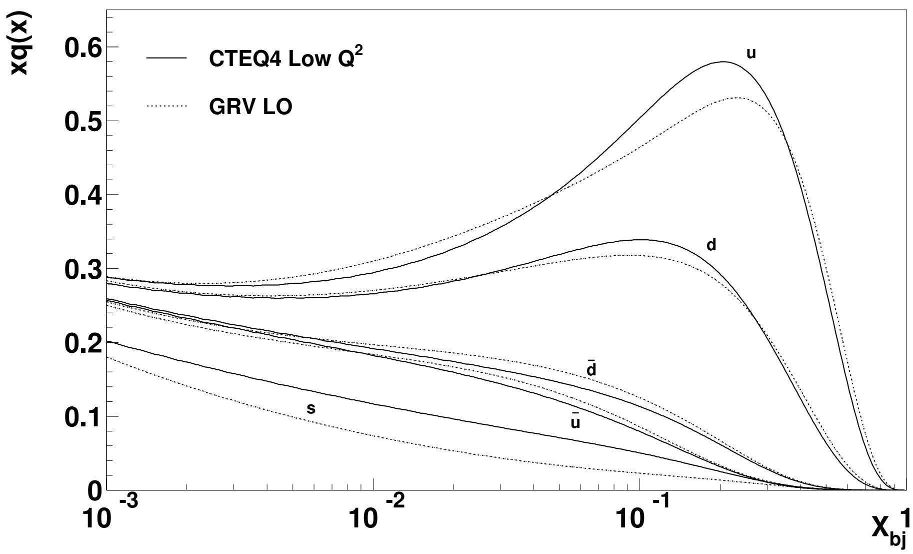

Figure 5.6: Unpolarized x-weighted Parton Density Functions, from the CTEQ Collaboration [11] and the GRV [12] group, evolved to $Q^2 = 2.5$ GeV^2.

In this analysis, however, a different approach is used. The LUND string model of Section 2.3.2 is implemented in the JETSET package [16], and embedded into the Monte Carlo. The advantages of including the fragmentation process in the Monte Carlo are twofold. It facilitates taking into account kinematic correlations between the parton distributions, fragmentation functions, and acceptance function. Also, assumptions concerning the fragmentation functions are no longer explicitly required (isospin symmetry of the pion fragmenation functions, for example). The LUND string model must first be tuned to fit HERMES yields, however. At higher energies, LUND has been successfully used to describe world data [17]. At these higher energies, the model includes higher order QCD processes to simulate jet production. HERMES does not have the energy to produce jets, and so the default LUND model does not reproduce its low energy hadron yields very well. The HERMES data has been simulated using only first order elements, and furthermore, the free parameters of the LUND model have been tuned to fit the measured semi-inclusive yields at HERMES [2]. Figure 5.8 shows the results of tuning LUND for HERMES. Similar fits have been performed using the independent fragmentation and cluster fragmentation models. As mentioned in Section 2.3.2, the cluster model is not successful in modeling

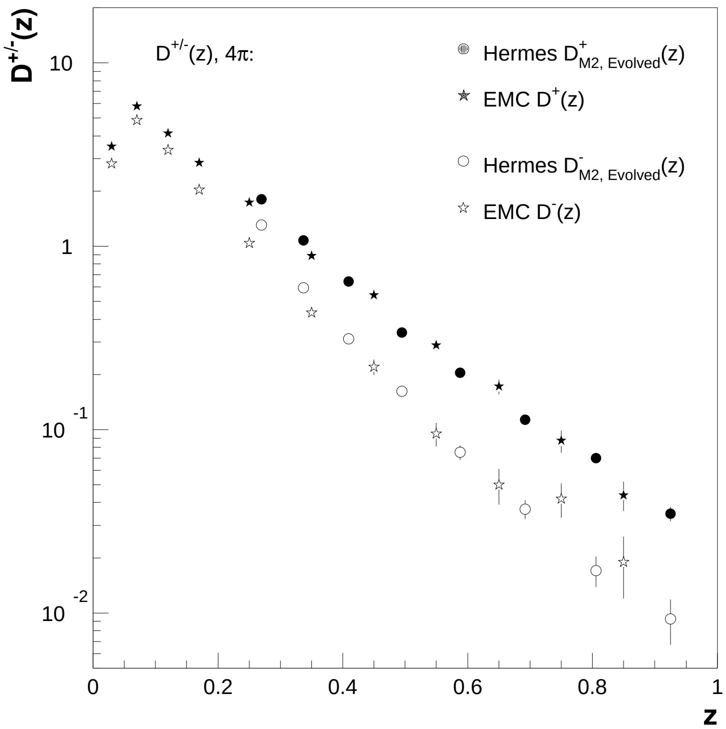

Figure 5.7: HERMES favored and unfavored pion fragmentation functions in 4π, overlaid with results of the EMC experiment [14]. HERMES results are evolved to the average Q^2 of EMC.

HERMES yields [13], so only results from the independent model fit are compared in the extraction. The LUND model and the independent fragmentation model are both included in the JETSET package, which is included in the HERMES Monte Carlo.

Acceptance

To facilitate detailed studies of HERMES spectrometer effects, the HERMES Monte Carlo simulates the response of each component of the spectrometer. Although it is the best simulation available, it is far too slow for use as a high-statistics generator, which is required for the purities. A simpler approach is to combine a simple box-model of the detector acceptance with a map of the HERMES magnetic field. The HRC momentum lookup table determines the magnetic bending of the tracks, and the bent trajectories are required to

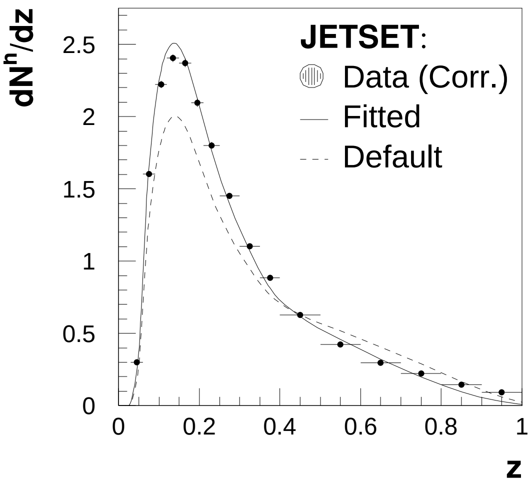

Figure 5.8: Comparison of LUND string model to HERMES data, before and after parameter tuning [13].

---

pass within the same geometric cuts as required in Table 4.5. This simple model assumes an ideal response from the HERMES spectrometer. This is reasonable, since all real detector effects are removed from the measured asymmetries, as detailed in Section 4.5.

Purities

Generating the inclusive DIS purities can be performed directly from Eq. 5.9, as the inclusive purities involve no fragmentation functions. Semi-inclusive purities are generated from the same equation, utilizing high statistics Monte Carlo simulations using the GRV parametrized unpolarized parton distributions, the fitted LUND string fragmentation model, and the HERMES acceptance. In the Monte Carlo simulation, the flavor of the struck quark for a generated scattering event is known. If all scattering events h from flavor q are tabulated as N_q^h, then the purity for this process can be written as

$$P_q^h(x) = \frac{N_q^h(x)}{\sum_{q'} N_{q'}^h(x)}. \tag{5.22}$$

Semi-inclusive purities are generated using the Monte Carlo, tabulating the generated events according to Eq. 5.22, shown for a proton target in Figure 5.9, and shown for a neutron target in Figure 5.10. The main features of the purities are due to the input parton

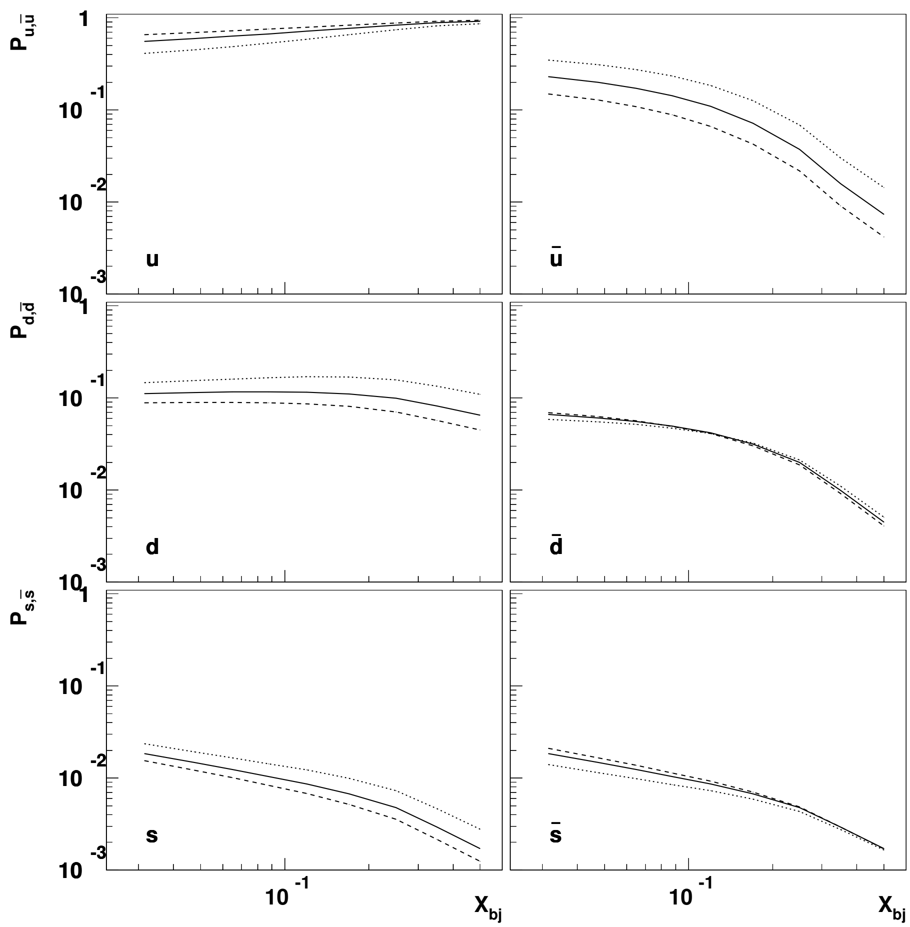

Figure 5.9: Inclusive proton purities (solid lines) and Semi-inclusive h^+ (dashed lines) and h^- (dotted lines) proton purities for the six light quark flavors.

distributions and charge-weighting in Eq. 5.9. The u-quarks dominate DIS in the proton, and so the u-purities are commensurately dominant, with under 10% of the inclusive events coming from the other flavors. For each quark flavor, the semi-inclusive purities are either enhanced or suppressed relative to the inclusive purities by the fragmention functions.

5.2.4 Treatment of Sea Polarization

Once the purities are generated, the form of the fitted vector $\vec{\mathbf{Q}}$ must be chosen. Optimally, polarizations of all the quark flavors that contribute significantly to the spin structure of

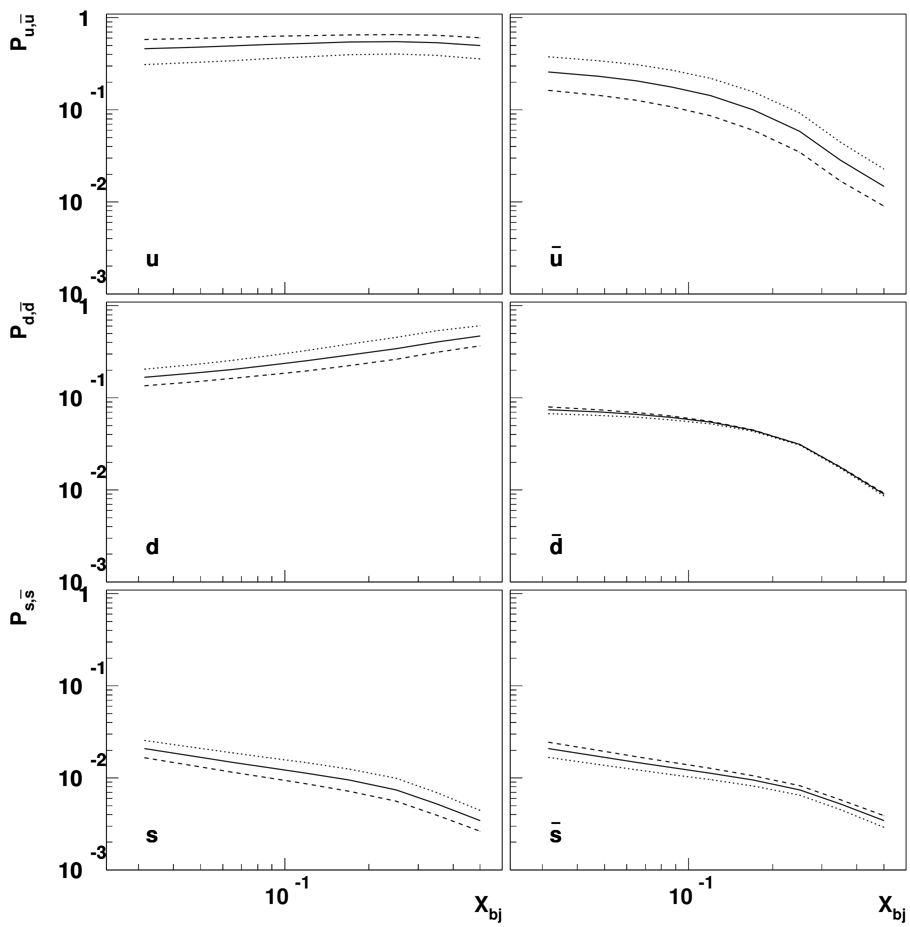

Figure 5.10: Inclusive neutron purities (solid lines) and Semi-inclusive h^+ (dashed lines) and h^- (dotted lines) neutron purities for the six light quark flavors.

---

the nucleon are included in the fit. This excludes the c, b, and t quarks, as their large mass prohibits a significant density of these flavors in the quark sea. This leaves the d, u, and s quark flavors, and their antiquark counterparts for a total of six independent quark polarizations.

The number of fitted quark polarizations in $\vec{\mathbf{Q}}$ depends on the number of physically distinct asymmetries — this analysis includes six different measured asymmetries, so a complete fit of the six light quark polarizations is possible. However, as is evident from Figures 5.9 and 5.10, the u purity dominates in the proton and to a lesser extent in the neutron, while the d quarks are significant in neutron. The sea quark purities, however, are relatively small. In practice, then, the small sensitivity of the asymmetries to the sea quarks makes a full six flavor separation difficult.

Instead of the full six flavor fit, a phenomenologically motivated model is imposed on the sea quark polarizations. The tiny dependencies of the HERMES asymmetries on the separate sea quark flavors can be combined into a more significant dependency on a single parameter that reflects the average sea properties. Possible choices of such models follow.

Unpolarized Sea

In the most simple model, sea quark spins are assumed to make no contribution to the total nucleon spin:

$$\Delta\bar{u} \;=\; \Delta\bar{d} \;=\; \Delta\bar{s} \;=\; \Delta s \;=\; 0. \tag{5.23}$$

This model is equivalent to treating the measured HERMES asymmetries as being linear in only two quark polarization, Δu and Δd. While providing for the most precise determination of u and d quark polarizations, the discussion of Chapter 1 indicates that polarized sea quark distributions may have a significant contribution to the nucleon spin. The sea quarks cannot be assumed to have zero polarization in a study of nucleon spin structure, and this assumption is not used in the analysis.

SU(3) Spin Symmetric Sea

If treated as polarized, the next assumption regarding the sea quarks is that their distributions be identical. This means that the different sea quark flavors show the same numbers densities in both spin states. For the purity fit, an average helicity distribution of the sea is defined:

$$\Delta q_{\text{sea}} \;\equiv\; \Delta\bar{u} \;=\; \Delta\bar{d} \;=\; \Delta\bar{s} \;=\; \Delta s \;\neq\; 0. \tag{5.24}$$

The purity for this average sea is then defined

$$P_{q_{\text{sea}}}\frac{\Delta q_{\text{sea}}}{q_{\text{sea}}} \;=\; \left(P_{\bar{u}}\frac{1}{\bar{u}} + P_{\bar{d}}\frac{1}{\bar{d}} + P_{\bar{s}}\frac{1}{\bar{s}} + P_{s}\frac{1}{s}\right)\Delta q_{\text{sea}}. \tag{5.25}$$

Here, the unpolarized distribution q_{sea} is arbitrary, as one multiplies and divides by it in defining the purity. Three parameters would be fit in the analysis, $\frac{\Delta u}{u}$, $\frac{\Delta d}{d}$, and $\frac{\Delta q_{\text{sea}}}{q_{\text{sea}}}$. $\bar{u}$

purities are typically much greater than the other sea purities, due to the $\bar{u}$ charge factor. Therefore, the average sea quark purity in this model is dominated by the $\bar{u}$ contribution. If the polarized sea quark distributions are not equal, the average polarized sea distribution extracted using this model will be dominated by $\Delta\bar{u}$.

SU(3) Polarization Symmetric Sea

A slight variation on the Spin Symmetric Sea model is to assume that the sea quark polarizations are flavor symmetric, as opposed to their spins:

$$\frac{\Delta q_{\text{sea}}}{q_{\text{sea}}} \equiv \frac{\Delta\bar{u}}{\bar{u}} = \frac{\Delta\bar{d}}{\bar{d}} = \frac{\Delta\bar{s}}{\bar{s}} = \frac{\Delta s}{s}. \tag{5.26}$$

The purity of the average sea is then defined

$$P_{q_{\text{sea}}}\frac{\Delta q_{\text{sea}}}{q_{\text{sea}}} = \left(P_{\bar{u}} + P_{\bar{d}} + P_{\bar{s}} + P_s\right)\frac{\Delta q_{\text{sea}}}{q_{\text{sea}}}. \tag{5.27}$$

This model is introduced because of recent Drell-Yan measurements from Fermilab [18], confirmed at HERMES [10], which indicate a light antiquark flavor asymmetry in the nucleon sea: $\bar{d}(x) - \bar{u}(x) > 0$, significantly so at low x. The inequality of the unpolarized sea distributions suggests that the polarized distributions are unequal as well. Furthermore, a quark flavor's polarized distribution cannot be greater than its unpolarized distribution. As $s(x) < \bar{d}(x)$, a large enough sea polarization would make the spin symmetric sea model unfeasible. The SU(3) polarization symmetric sea model is used in this analysis.

5.2.5 Valence Treatment

Just as there are different models by which to treat the sea, in the purity extraction there are several ways to separate the u and d distributions into valence and sea portions. Namely, there is the **Valence Fit**, in which $\frac{\Delta u_{\text{v}}}{u_{\text{v}}}$, $\frac{\Delta d_{\text{v}}}{d_{\text{v}}}$, and the sea polarization are fitted, the **Simple Fit**, in which $\frac{\Delta u}{u}$, $\frac{\Delta d}{d}$, and the sea polarization are fitted, and finally, the **Flavor Symmetric Fit**, in which $\frac{\Delta u+\Delta\bar{u}}{u+\bar{u}}$, $\frac{\Delta d+\Delta\bar{d}}{d+\bar{d}}$, and sea polarization are fitted.

As these three fits only differ by how the sea and valence polarizations are separated, the results of any one fit can be used to derive the others using the definitions of $u_{\text{sea}}(d_{\text{sea}})$

and $u_{\mathrm{val}}(d_{\mathrm{val}})$. The flavor symmetric fit is used in the analysis.

5.2.6 Monte Carlo Study of Purity Matrix Inversion

The polarization symmetric sea model and the flavor symmetric fit decided upon, a fit of the asymmetries of the previous chapter can be performed.

The PEPSI Monte Carlo models both the polarized and unpolarized contributions to the deep-inelastic cross-section. Monte Carlo asymmetries can be used to test the implementation of the purity formalism. If an initial parametrization of polarized parton distributions is chosen, Monte Carlo asymmetries and purities can both be generated, and the purity technique can be performed to verify that the input parton parametrizations can be extracted from the Monte Carlo generated data. This is only a check of the implementation of the extraction technique, not a check of the technique's validity. Using the GRV

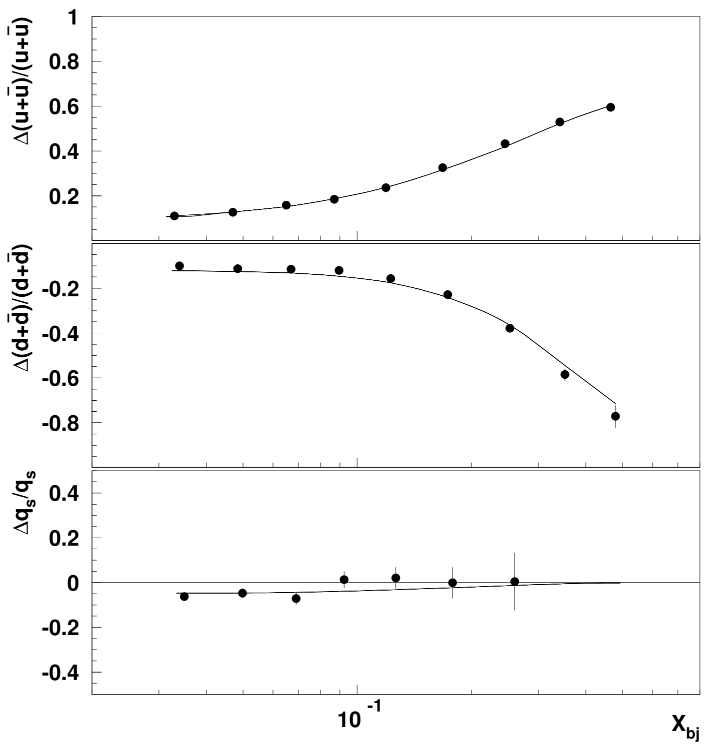

Figure 5.11: Successful extraction of Monte Carlo inputs from Monte Carlo generated asymmetries. Solid lines show the input parametrizations, while the data points show purity extraction results.

parametrizations [12] of 1995 as input parton distributions, Figure 5.11 shows the results of such a Monte Carlo test.

5.2.7 Uncertainties of Purity Extracted Polarizations

Uncertainty from Input Asymmetries

An advantage of the purity extraction technique is that the statistical and systematic uncertainties of the extracted quark polarizations can be derived from those of the asymmetries using Eq. 5.13 and the asymmetry covariances. The covariance $\mathcal{C}_Q$ is calculated twice, once using the statistical asymmetry covariance matrix alone, and once using the total (statistical and systematic) covariance matrix. The systematic covariance matrix of the extracted polarizations is then the difference

$$\mathcal{C}_Q^{\mathrm{sys}} = \mathcal{C}_Q^{\mathrm{total}} - \mathcal{C}_Q^{\mathrm{stat}}. \tag{5.28}$$

The diagonal elements of the covariance matrices give the squares of the uncertainties on the extracted polarizations; the systematic uncertainties of the polarizations are given by

$$\delta \frac{\Delta q_i}{q_i} = \sqrt{\mathcal{C}_Q^{\mathrm{sys,ii}}}. \tag{5.29}$$

Purity Systematic Uncertainty

Effects of the additional systematic uncertainties from the input purities are estimated by running the analysis with different models of the unpolarized physics involved. For each model, a set of purities is calculated and the quark polarizations extracted. The resulting spread gives an uncorrelated uncertainty.

For the uncertainty due to the unpolarized parton distributions, the two models from the CTEQ and GRV groups are used. For the uncertainty due to fragmentation, the uncertainty is calculated from the models fitted to HERMES yields, mentioned in Section 5.2.3.

Unpolarized Sea Model Uncertainty

In applying the Unpolarized Sea Model (Section 5.2.4), a systematic uncertainty must be assigned for the maximum possible variation of the sea polarization from zero. The polarized parton distribution cannot, by definition, exceed the unpolarized distribution. Since the parton distributions defined on $\mathbf{F_1}$ are desired, the R correction introduced in Section 2.1.3 provides the positivity limit on the sea quark polarizations, $\frac{\Delta q_{\rm sea}}{q_{\rm sea}} = \pm\frac{1+\gamma^2}{1+R}$. The asymmetries are corrected for this maximal(minimal) sea polarization, the analysis rerun for each case, and the differences in extracted quark polarizations taken as uncorrelated uncertainties.

5.2.8 Polarizations and Spin Distributions

The formalism of the preceding sections is used to fit the measured HERMES 1995, 1996 and 1997 asymmetries to the polarizations of the quarks in the nucleon in the Quark Parton Model.

The SU(3) polarization symmetric model of the sea of Section 5.2.4 is used; however, an unpolarized sea is assumed above x of 0.3. From the unpolarized parton distributions shown in Figure 5.6, it can be seen that the sea quark density decreases rapidly with x: the number of sea quarks carrying a substantial fraction of the nucleon momentum is negligible. The positivity limit of the previous section then provides a strong enough constraint on the possible sea contribution in this region to the nucleon spin. Further, by assuming the sea polarization to be zero here, the reduction of the fit parameters to two increases the statistical precision of the up and down polarization fit at the cost of a slight increase in the systematic uncertainty.

Extracted Quark Polarizations

The results use the inclusive and semi-inclusive hadron asymmetries, shown in Figures 4.9, 4.10, and 4.11. The main result of the purity extraction, assuming a polarization symmetric sea, and using a flavor symmetric fit of the light quarks, is seen in Figure 5.12. A table of the results is seen in Table 5.1. The up quark polarizations are positive and the down quark polarizations are negative over the measured range of x. The polarizations are largest at

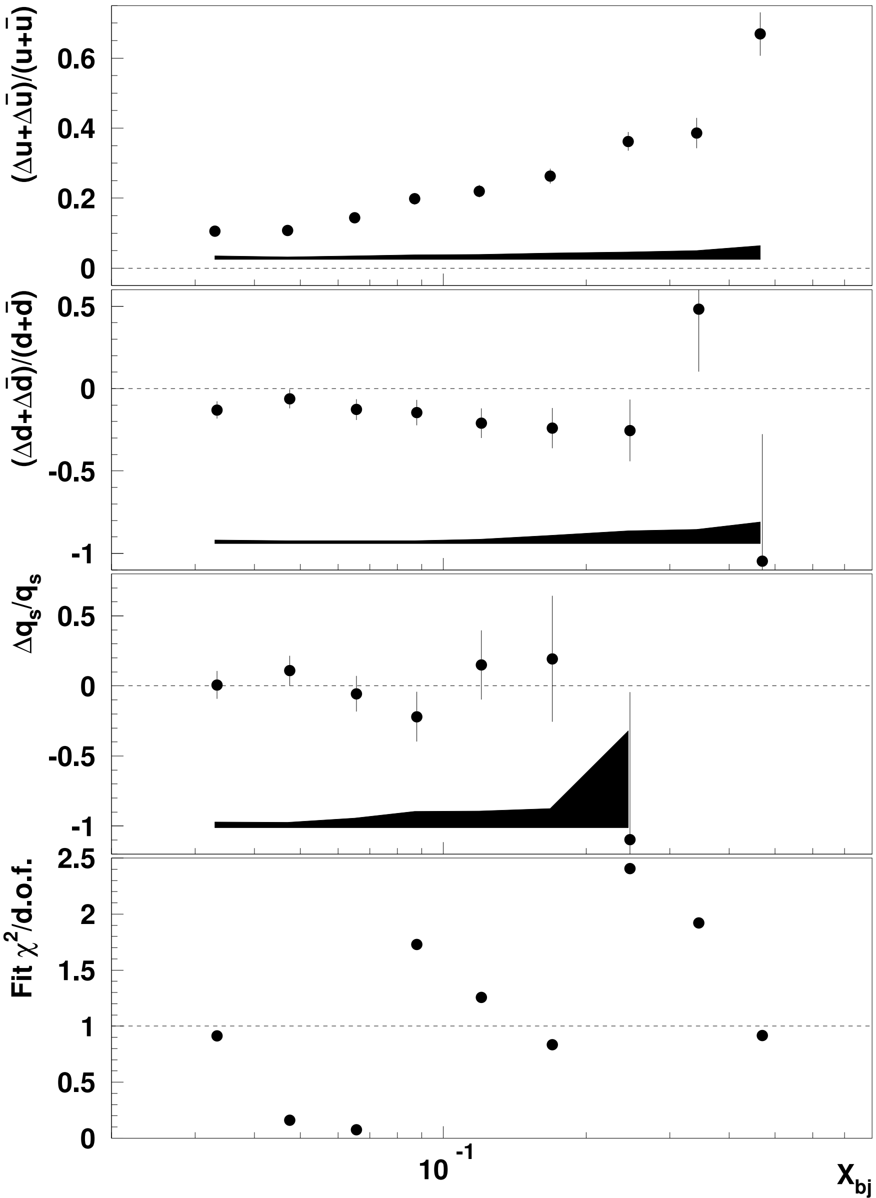

Figure 5.12: Flavor decomposition of nucleon quark polarization as a function of x, derived from HERMES inclusive and semi-inclusive asymmetries.

large x and remain different from zero in the sea region. The sea polarization is compatible with zero over the measured range of x. The overall χ^2 per degree of freedom of the fit is 1.1.

The different contributions to the systematic uncertainties in the polarization extraction are calculated as detailed in Section 5.2.7. The total systematic uncertainty can be separated into a contribution from the input asymmetries, and a contribution from the purity extraction itself. The former incorporates the uncertainties due to the polarization measurements of the target and beam, yield fluctuations in the 1995 data, and the smearing and radiative corrections to the asymmetries. The latter includes the uncertainties in choosing the fragmentation model and unpolarized parton distribution set, and a contribution from the assumptions concerning Δq_{s}. A graphical representation of the breakdown of the systematic uncertainties of Table 5.1 into the purity components and the asymmetry components can be seen in Figure 5.13. The systematic uncertainty of the u polarization is dominated by those from the input asymmetries. The d polarization shows sensitivity to the choice of fragmentation model at high x while the sea quark polarization is sensitive to the fragmentation model over the entire measured range.

$\langle x\rangle$	$\frac{\Delta u+\Delta\bar{u}}{u+\bar{u}}$	$\frac{\Delta d+\Delta\bar{d}}{d+\bar{d}}$	$\frac{\Delta q_s}{q_s}$	χ^2/d.o.f
0.033	$0.106 \pm 0.013 \pm 0.010$	$-0.130 \pm 0.052 \pm 0.021$	$0.007 \pm 0.099 \pm 0.042$	0.91
0.047	$0.108 \pm 0.014 \pm 0.007$	$-0.062 \pm 0.057 \pm 0.016$	$0.109 \pm 0.106 \pm 0.039$	0.16
0.065	$0.144 \pm 0.015 \pm 0.011$	$-0.127 \pm 0.063 \pm 0.017$	$-0.056 \pm 0.127 \pm 0.068$	0.07
0.087	$0.198 \pm 0.017 \pm 0.013$	$-0.146 \pm 0.077 \pm 0.016$	$-0.220 \pm 0.178 \pm 0.117$	1.73
0.119	$0.220 \pm 0.018 \pm 0.014$	$-0.210 \pm 0.090 \pm 0.026$	$0.150 \pm 0.248 \pm 0.119$	1.26
0.168	$0.263 \pm 0.021 \pm 0.019$	$-0.239 \pm 0.122 \pm 0.050$	$0.193 \pm 0.450 \pm 0.137$	0.84
0.244	$0.362 \pm 0.027 \pm 0.022$	$-0.254 \pm 0.188 \pm 0.078$	$-1.098 \pm 1.054 \pm 0.691$	2.41
0.342	$0.386 \pm 0.043 \pm 0.025$	$0.482 \pm 0.380 \pm 0.085$	—	1.92
0.465	$0.669 \pm 0.062 \pm 0.039$	$-1.047 \pm 0.770 \pm 0.129$	—	0.92

Table 5.1: Extracted values for flavor separated quark polarizations versus x with the SU(3) symmetric sea model.

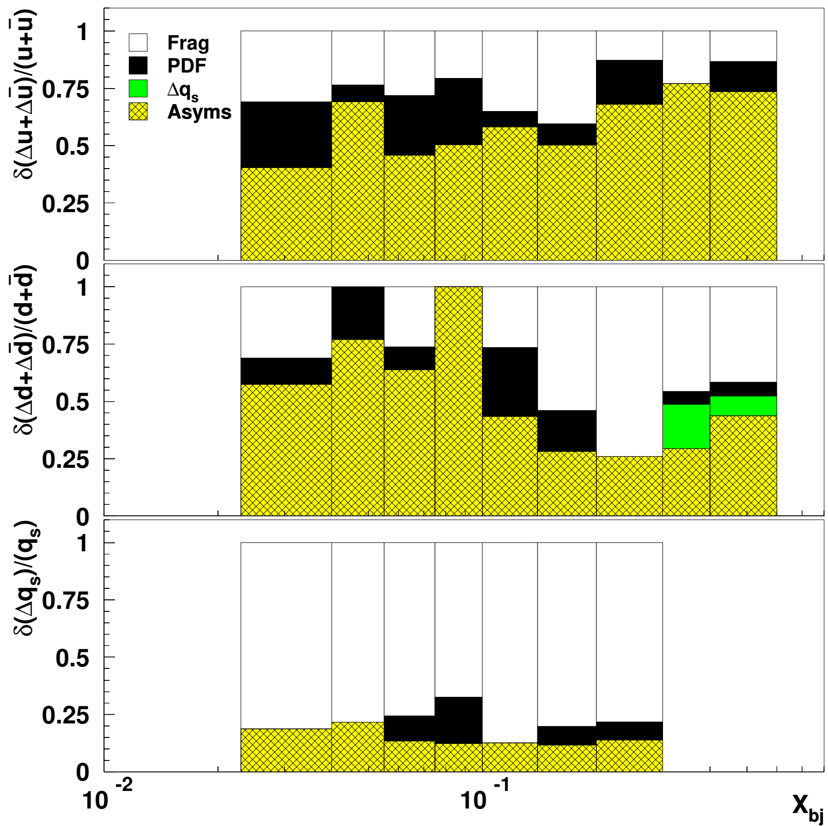

Figure 5.13: Fractional breakdown of contributions to systematic error of the extracted polarizations. 'Frag' denotes the contribution from choice of fragmentation model, 'PDF' from choice of unpolarized parton distribution set, 'Δq_s' from setting the sea polarization to zero in the highest two bins. 'Asyms' denotes the contribution from the systematic error on the asymmetries.

Extracted Parton Distributions

Calculating parton distributions from the extracted polarizations is straightforward. The polarizations are multiplied by unpolarized parton distributions evaluated at the average x of each bin. The unpolarized distributions are evaluated at an average Q^2 of 2.5 GeV^2, evolving the polarized parton distributions to this Q^2 value as well. The quark polarizations are assumed to be Q^2 independent in the leading order, as motivated by Reference [19] and Figure 4.11, which depicts asymmetries calculated from data taken at different Q^2 values. Note that the resultant parton distributions are also multiplied by x in the following figures. The resultant parton distributions are are shown in Figure 5.14, along with three parametrizations of previous world data on polarized DIS: GRSV 95 Leading Order Standard Scenario [20], Gehrmann-Stirling Leading Order Gluon Set A [1], and De Florian *et al.* Leading Order Set B [21].

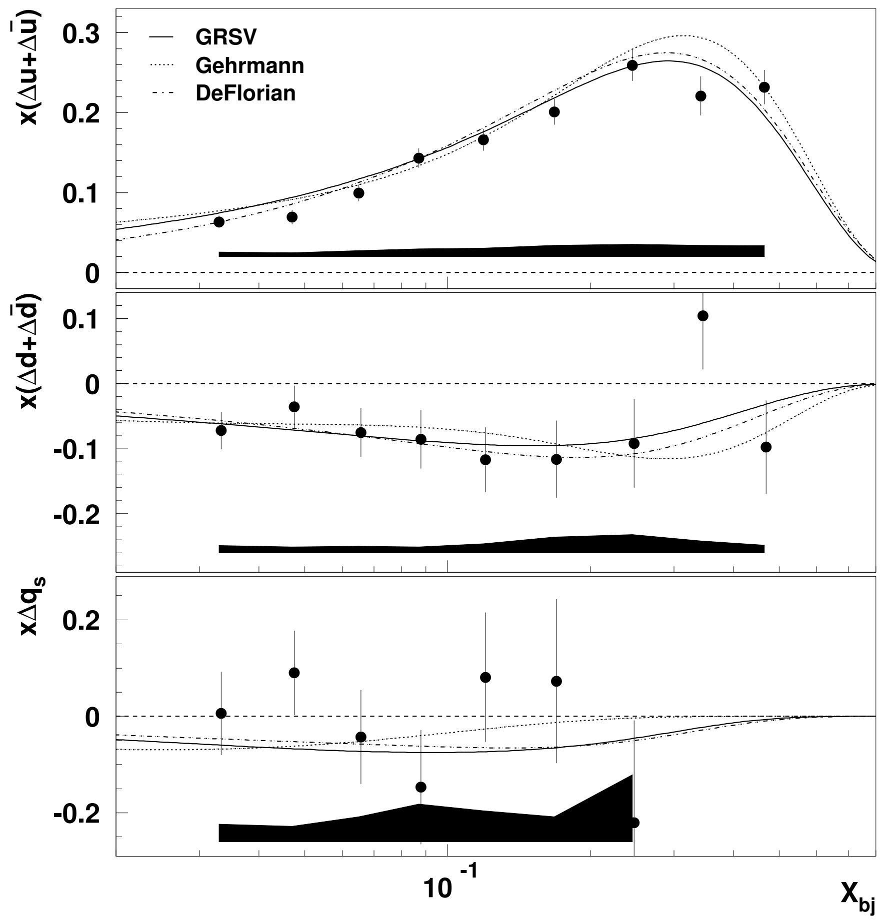

Figure 5.14: Quark spin distributions at $Q^2 = 2.5$ GeV^2 as a function of x. Error bars shown are statistical and the dark bands show systematic uncertainties. The various curves are parametrizations of other world data. See text for details.

The GRSV and Gehrmann-Stirling groups' parametrizations include world polarized data up to 1995, including results from E142, E143, and SMC, as well as the results of hyperon decay analysis. De Florian *et al.* adds still more recent data, including measurements from E154 and the semi-inclusive measurements of SMC. Of note is that both GRSV and

De Florian *et al.* fit world data on A_1, while Gehrmann-Stirling fit world g_1 values. The A_1 fits assume R is zero; experimental extractions of g_1 correct for the measured R values. An R correction is applied to the A_1 fits in order to make a consistent comparison with this analysis. From each group, the leading order analysis is chosen for consistency with the assumptions in this analysis.

The results from this analysis are consistent with all three parametrizations. The polarized up distribution is slightly lower than the parametrizations; the statistical uncertainties of the down distribution are too large to claim a precise x-dependence. The sea quark polarization is closer to zero than to any of the parametrizations, which are constrained by hyperon decay constants. Note that the sea result in this purity analysis is primarily a measurement of the Δu_s and $\Delta \bar{u}$ distributions, not Δs.

The distributions of Figure 5.14 can be manipulated into the polarized valence u and d distributions. HERMES results are compared with results from SMC in Figure 5.15; the two experiments have compatible results, though the precision in this analysis is greater due to better statistics on the proton.

Sea Model Comparison

This analysis has focused on an SU(3) polarization symmetric sea, but it is interesting to see the differences of other assumptions on the purity extraction. SMC and the groups whose parametrizations are used in the preceding sections do not assume flavor symmetric polarization in the sea, but instead assume spin symmetry. A comparison of purity analysis results for these two competing sea models is shown in Figure 5.16.

Little dependence on the sea model assumption is seen, as the extracted parton distributions are essentially the same. Differences in the input purities are due to differences in the unpolarized sea distributions. The extracted polarized distributions do not reflect this due to the u_s and $\bar{u}$ dominance in the sea.

5.2.9 Moments of the Distributions

The total contribution of a quark flavor to the proton spin is calculated by integrating its measured polarized parton distribution over the entire x range. In practice, this is broken

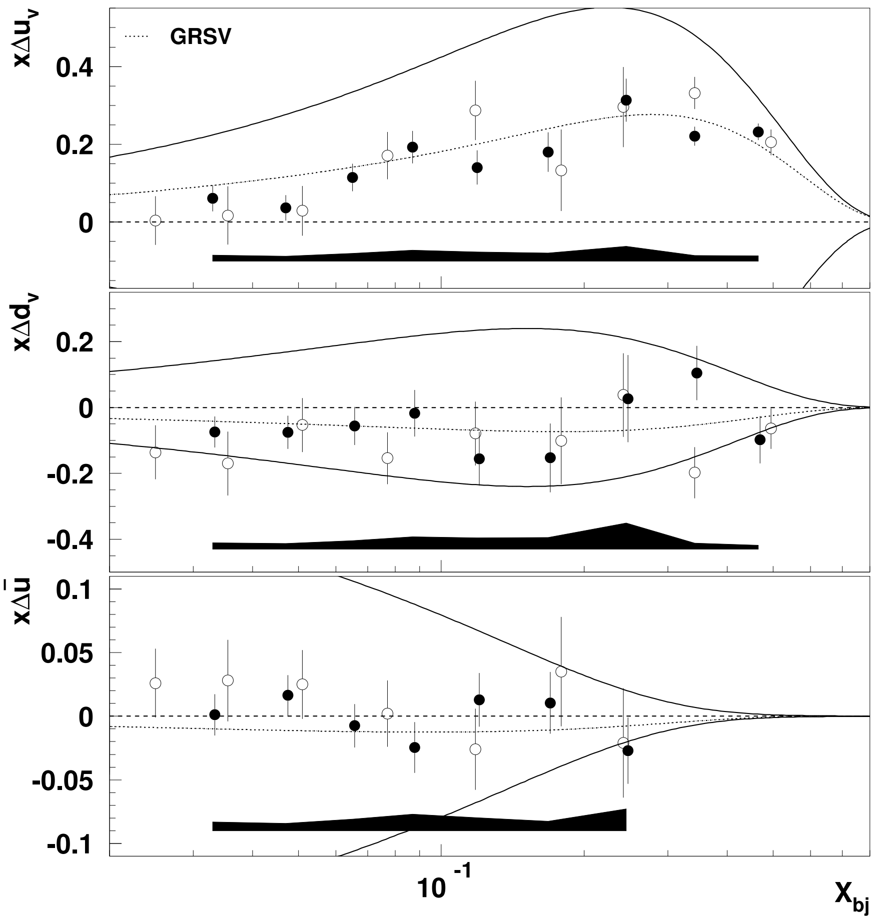

Figure 5.15: Quark spin distributions at $Q^2 = 2.5$ GeV^2 for the valence quarks $x\Delta u_v$, $x\Delta d_v$ and the sea quarks $x\Delta\bar{u}$ as a function of x. Error bars shown are statistical and the dark bands show systematic uncertainties. The distributions from this analysis (solid circles) are compared to results from SMC (open circles), extrapolated to the same Q^2. The solid lines indicate the positivity limits of the unpolarized distributions and the dashed lines are the parametrization of GRSV (Standard, LO).

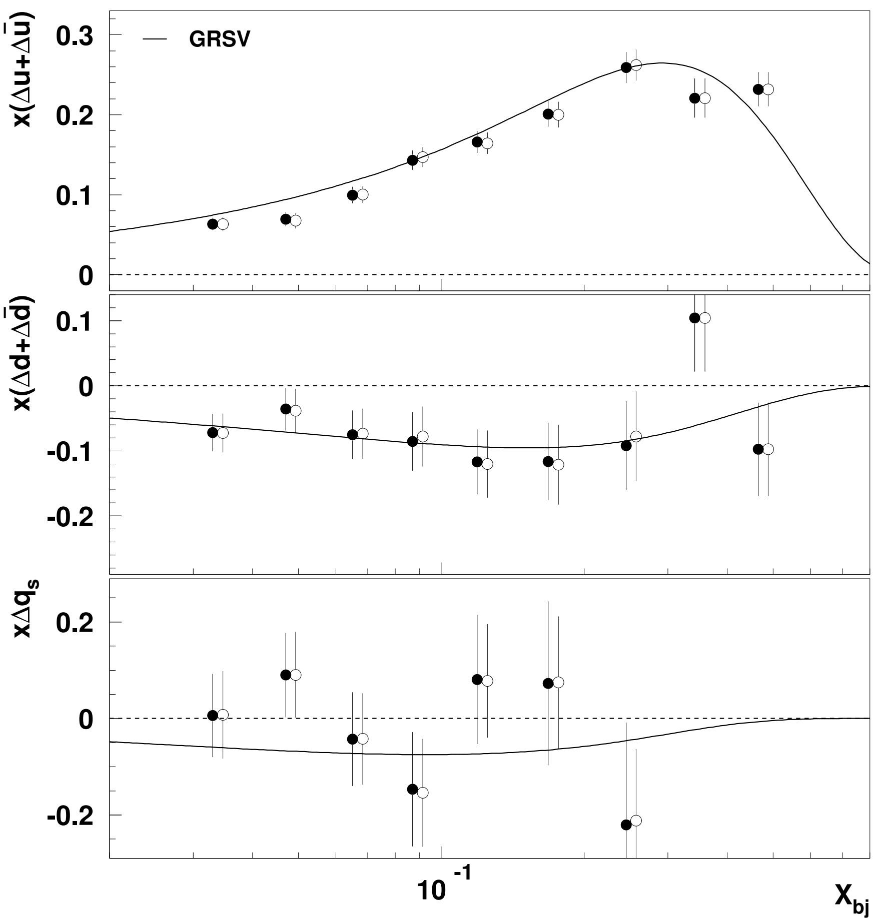

Figure 5.16: Quark spin distributions at $Q^2 = 2.5$ GeV^2 extracted assuming an SU(3) polarization symmetric sea (solid circles) and assuming an SU(3) spin symmetric sea (open circles). Only statistical errors are shown. The curve is the parametrization of GRSV (Standard, LO).

into three parts: the measured region $0.023 < x < 0.6$, the low x region $x < 0.023$, and the high x region $x > 0.6$.

In the measured region, it is assumed that the quark polarization is constant over each kinematic x bin to provide a direct and simple measurement. In each bin, the measured quark polarization is multiplied by the integral of the relevant unpolarized distribution over the bin, using the parametrizations from Reference [11].

$$\Delta q_f = \sum_i \left(\frac{\Delta q_f}{q_f}|_i \int_{x_i}^{x_{i+1}} q_f(x)|_{Q^2} \, dx \right) \tag{5.30}$$

As is indicated, the unpolarized distribution is evolved to any Q^2 to calculate the integrated spin fraction at that same Q^2. The n^{th} moment can be calculated by multiplying the unpolarized distribution by x^n before integrating.

The integral over the measured region can be compared to other experiments with little theoretical uncertainty. Table 5.2 shows several of the integrated spin distributions compared with the same measurements from SMC.

	This Analysis	SMC
Δu_v	$0.52 \pm 0.04 \pm 0.08$	$0.59 \pm 0.08 \pm 0.07$
Δd_v	$-0.19 \pm 0.09 \pm 0.13$	$-0.33 \pm 0.11 \pm 0.09$
$\Delta \bar{u}$	$-0.01 \pm 0.02 \pm 0.03$	$0.02 \pm 0.03 \pm 0.02$
$\Delta \bar{d}$	$-0.02 \pm 0.03 \pm 0.04$	$0.02 \pm 0.03 \pm 0.02$
$x\Delta u_v$	$0.12 \pm 0.01 \pm 0.01$	$0.15 \pm 0.02 \pm 0.01$
$x\Delta d_v$	$-0.02 \pm 0.02 \pm 0.02$	$-0.05 \pm 0.02 \pm 0.02$

Table 5.2: Comparison of the HERMES measured region integrals of valence and sea spin distributions with SMC results [15]. The SMC values are extrapolated to $Q^2 = 2.5$ GeV^2 and integrated over the HERMES x-range of $0.023 < x < 0.6$.

Extrapolating the integral to include the low x contribution is problematic, as there is no clear prediction for the behavior of polarized parton distributions at low x. In the past, g_1 analyses have extended their integrals to low x by assuming Regge parametrization [22, 23]. E154, in their g_1^n extraction [24], show data in conflict with a simple Regge parametrization. For comparison with other measurements, HERMES has extrapolated to low x assuming a simple Regge parametrization of $\Delta q_f(x) \propto x^{-\alpha}$ with $\alpha = 0$ for the first three bins in the analysis ($x < 0.075$). Due to the strong model dependence of the result, no error is reported for this extrapolation.

The high-x extrapolation $0.6 < x < 1.0$ was obtained by fitting the functional forms of the CTEQ unpolarized distributions [11] to the data. The systematic uncertainty of this extrapolation is small and is included in the quoted uncertainty of the total integral.

Official HERMES integrals [25] can be found in Table 5.3 along with predictions for their values from SU(3) analysis and from Lattice QCD calculations [26]. The HERMES

	Measured region	Low-x	Total integral	Prediction		Q^2
$\Delta u + \Delta\bar{u}$	$0.51_{\pm 0.02 \pm 0.03}$	0.04	$0.57_{\pm 0.02 \pm 0.03}$	$0.66_{\pm 0.03}$	SU(3)	2.5
$\Delta d + \Delta\bar{d}$	$-0.22_{\pm 0.06 \pm 0.05}$	-0.03	$-0.25_{\pm 0.06 \pm 0.05}$	$-0.35_{\pm 0.03}$	SU(3)	2.5
$\Delta s + \Delta\bar{s}$	$-0.01_{\pm 0.03 \pm 0.04}$	0.00	$-0.01_{\pm 0.03 \pm 0.04}$	$-0.08_{\pm 0.02}$	SU(3)	2.5
$\Delta\bar{u}$	$-0.01_{\pm 0.02 \pm 0.03}$	0.00	$-0.01_{\pm 0.02 \pm 0.03}$			
$\Delta\bar{d}$	$-0.02_{\pm 0.03 \pm 0.04}$	0.00	$-0.01_{\pm 0.03 \pm 0.04}$			
Δu_v	$0.52_{\pm 0.05 \pm 0.08}$	0.03	$0.57_{\pm 0.05 \pm 0.08}$	$0.84_{\pm 0.05}$	Lattice	5
Δd_v	$-0.19_{\pm 0.11 \pm 0.13}$	-0.03	$-0.22_{\pm 0.11 \pm 0.13}$	$-0.25_{\pm 0.02}$	Lattice	5
$x\Delta u_v$	$0.12_{\pm 0.01 \pm 0.01}$	0.00	$0.13_{\pm 0.01 \pm 0.01}$	$0.198_{\pm 0.008}$	Lattice	4
$x\Delta d_v$	$-0.02_{\pm 0.02 \pm 0.02}$	0.00	$-0.02_{\pm 0.02 \pm 0.02}$	$-0.048_{\pm 0.003}$	Lattice	4

Table 5.3: The integrals of various spin distributions. The results are given for the measured region $0.023 < x < 0.6$, for the low-x extrapolation and for the total integral. Note that the entry for $\Delta s + \Delta\bar{s}$ does not represent a direct measurement of the strange sea but relies on the sea polarization flavor symmetry assumption. An uncertainty of the Regge-type extrapolation at low-x is not included in the quoted error for the total integral. The HERMES results are given for $Q^2 = 2.5$ GeV^2. The Q^2 values of the predictions are quoted in GeV^2.

results are mostly compatible with the predictions of SU(3) symmetry analysis. The largest disagreement is in the strange spin fraction $\Delta s + \Delta\bar{s}$. HERMES data suggests that the sea is unpolarized where SU(3) predicts a negative contribution to the overall spin. It should be noted that the s-quark results in this analysis are based on a measurement of all sea quarks, which are dominated by the u-quarks. HERMES extracted first and second moments of valence spin fraction are significantly lower than the lattice predictions.

References

[1] T. Gehrmann and W.J. Stirling, Phys. Rev. D **53**, 6100 (1996).

[2] H. Tallini, Ph.D. thesis, University of Liverpool, 1998.

[3] M.A. Funk, Ph.D. thesis, University of Hamburg, Germany, 1998.

[4] J. Niczyporuk and E. Bruins, Phys. Rev. D **58**, 091501 (1998).

[5] J. Friar, B. Gibson, *et al.*, Phys. Rev. C **42**, 2310 (1990).

[6] C. degli Atti, S. Scopetta, *et al.*, Phys. Rev. C **48**, R968 (1993).

[7] M. Veltri, Max Planck Institute—Heidelberg, Note MPIH-V18-1992.

[8] G. Ingelman *et al.*, 1996, DESY Report 96-057.

[9] K. Ackerstaff, Ph.D. thesis, University of Hamburg, Germany, 1996.

[10] HERMES Collaboration, Phys. Rev. Lett. **81**, 5519 (1998).

[11] H. Lai *et al.*, Phys. Rev. D **55**, 1280 (1997).

[12] M. Glück, E. Reya, and W. Vogelsang, Z. Phys. C **67**, 433 (1995).

[13] P. Geiger, Ph.D. thesis, Ruprecht-Karls-Universität Heidelberg, Germany, 1998.

[14] European Muon Collaboration, Nucl. Phys. B **321**, 541 (1989).

[15] Spin Muon Collaboration, Phys. Lett. B **420**, 180 (1998).

[16] T. Sjöstrand, Comp. Phys. Comm. **82**, 74 (1994).

[17] JADE Collaboration, Phys. Lett. B **157**, 340 (1985).

[18] NuSea Collaboration, Phys. Rev. Lett. **80**, 3715 (1998).

[19] Spin Muon Collaboration, Phys. Rev. D **58**, 112001 (1998).

[20] M. Glück, E. Reya, M. Stratmann and W. Vogelsang, Phys. Rev. D **53**, 4775 (1996).

[21] D. de Florian, O. A. Sampayo and R. Sassot, Phys. Rev. D **57**, 5803 (1998).

[22] R. Heimann, Nucl. Phys. B **64**, 429 (1973).

[23] J. Ellis and M. Karliner, Phys. Lett. B **213**, 73 (1988).

[24] E154 Collaboration, Phys. Rev. Lett. **79**, 26 (1997).

[25] HERMES Collaboration, Phys. Lett. B **464**, 123 (1999).

[26] M. Göckeler *et al.*, Phys. Lett. B **414**, 340 (1997).

6

Conclusions

The first three years of HERMES data taking has yielded high statistics polarized deep inelastic scattering on ^{3}He and ^{1}H targets. These events, in concert with a large acceptance open-geometry spectrometer and good scattered particle identification, allow HERMES to probe inclusive and semi-inclusive reactions to a greater degree than done previously.

From the polarized scattering events, inclusive and semi-inclusive charged hadron asymmetries have been formed, and presented as a function of x_{Bj}. Using the framework of the Quark-Parton Model, these asymmetries can be simultaneously fit to constrain the polarizations of the different flavors of quarks in the nucleon. These polarizations in turn can be converted into polarized, or helicity difference, parton distributions by multiplying by unpolarized parton distribution parametrizations that have been precisely fit to world data. The extracted values for the measured region ($0.023 < x_{\mathrm{Bj}} < 0.60$) integrals of these distributions for both valence and sea quarks have been presented, and are $\Delta u_v = 0.522 \pm 0.044 \pm 0.085$, $\Delta d_v = -0.190 \pm 0.089 \pm 0.130$, and $\Delta \bar{u} = -0.006 \pm 0.020 \pm 0.025$.

These measurements agree with SMC: the valence measurements are consistent with each other and the sea measurements from both are consistent with zero. It should be noted that while SU(3) analysis predicts a negative strange quark polarization, the HERMES and SMC measurements assume that the sea spin contributions are polarization-symmetric and spin-symmetric, respectively. This reported sea polarization, then, is an average over all sea flavors, and a positive $\bar{u}$ polarization could offset a negative s polarization. The polarization-symmetric and spin-symmetric assumptions make negligible difference in the extracted distributions.

The limiting portion of this data set is the lack of statistics on an effective neutron target. HERMES will soon have a new data set with high statistics accumulated on a deuterium target, which should improve the statistical precision of the determined d-quark polarized distribution. For this deuterium run, the Threshold Čerenkov was replaced by a Ring Imaging Čerenkov detector. This will allow detection of π, K, and p over nearly all momenta. Fragmentation studies to these particles will be furthered, and it will be possible to form π and K asymmetries without their usefulness being statistically crippled. The Kaon asymmetries in particular provide direct sensitivity to the strange quark polarization in the nucleon, allowing a Purity analysis to directly extract Δs without requiring SU(3) symmetry. These improvements to HERMES as well as the commissioning of new spin experiments should provide for a more complete understanding of nucleon spin composition.

Vita

Balijeet Singh Bains was born on September 22, 1972 in New Orleans, Louisiana. After completing a B.S. in Physics from Louisiana State University and A & M College in 1993, he entered graduate school at the University of Illinois at Urbana-Champaign. There, he joined the Nuclear Physics Laboratory in 1994, earned an M.S. in physics in 1995, and a Ph.D. in physics in 2000.